



**Michigan  
Technological  
University**

Michigan Technological University  
**Digital Commons @ Michigan Tech**

---

Dissertations, Master's Theses and Master's Reports

---

2016

## Thermomechanical Processing of Aluminum Micro-alloyed with Sc, Zr, Ti, B, and C

Cameron McNamara

*Michigan Technological University, ctmcnama@mtu.edu*

Copyright 2016 Cameron McNamara

---

### Recommended Citation

McNamara, Cameron, "Thermomechanical Processing of Aluminum Micro-alloyed with Sc, Zr, Ti, B, and C", Open Access Dissertation, Michigan Technological University, 2016.  
<https://digitalcommons.mtu.edu/etdr/240>

Follow this and additional works at: <https://digitalcommons.mtu.edu/etdr>



Part of the [Metallurgy Commons](#)

THERMOMECHANICAL PROCESSING OF ALUMINUM MICRO-ALLOYED  
WITH Sc, Zr, Ti, B, AND C

By

Cameron T McNamara

A DISSERTATION

Submitted in partial fulfillment of the requirements for the degree of

DOCTOR OF PHILOSOPHY

In Materials Science and Engineering

MICHIGAN TECHNOLOGICAL UNIVERSITY

2016

©2016 CT McNamara



This dissertation has been approved in partial fulfillment of the requirements for the Degree of DOCTOR OF PHILOSOPHY in Materials Science and Engineering.

Department of Materials Science and Engineering

Dissertation Advisor: *Professor Stephen Kampe*

Committee Member: *Assoc. Professor Doug Swenson*

Committee Member: *Assoc. Professor Paul Sanders*

Committee Member: *Asst. Professor Scott Wagner*

Department Chair: *Professor Stephen Kampe*



*To Ms. Bailey K. Ross and our daughter Sawyer Sofia*



## Table of Contents

---

<b>Preface</b> .....	ix
<b>Acknowledgments</b> .....	xi
<b>Abstract</b> .....	xiii
<b>Introduction: The Case for HSLA-Al</b> .....	1
<b>Chapter I: Precipitation Strengthening of Dilute Al-TM alloys</b> .....	3
1 Introduction.....	3
1.1 Diffusion and Characteristics of Trialuminides.....	3
1.2 Strengthening Mechanisms.....	5
1.2.1 Precipitation, Dislocation, and Solute Strengthening.....	6
1.3 Existing Alloys.....	10
1.4 HSLA-Al Alloys sans Scandium.....	10
1.5 Scope of the Current Study.....	11
2 Methods.....	12
2.1 Casting.....	12
2.2 Thermomechanical Processing.....	14
2.3 Macroscale Imaging and Compositional Analysis.....	16
2.4 Microhardness, Conductivity, and Tensile Testing.....	16
2.5 Electron Microscopy.....	17
3 Results.....	17
3.1 Cooling Rates and Compositions.....	17
3.2 As-cast Grain Structures and Porosity.....	19
3.3 Multi-step and Two-step Isothermal Aging Curves.....	20
3.4 Comparison of Peak Microhardness for Al-Sc-Zr and Al-Zr Alloys.....	25
3.5 Tensile Stress-Strain Curves for Al-Sc-Zr and Al-Mg-Sc-Zr.....	27
3.6 Post-mortem TEM Imaging of Nanoscale Precipitates and SEM Fractography.....	29
4 Discussion.....	30
4.1 Quality of Castings.....	30
4.1.1 Grain Refinement.....	31
4.2 Hardness Increases from Mg, Ti, Ti-B, and Ti-C Additions.....	32
4.3 Increase of Hardness and Yield Strength and Hardness through Precipitation.....	34
4.3.1 Effect of Mg, Ti, Ti-B, and Ti-C on Aging.....	38
4.3.2 Effect of Cold Work on Aging.....	38
4.4 Challenges.....	41
5 Conclusions.....	44
<b>Chapter II: Recrystallization Resistance in Grain Refined Dilute Al-Zr Alloys</b> .....	47
1 Introduction.....	47
1.1 Use of Zr in Combination with Al-Ti-B, Al-Ti-C.....	47
1.2 Recrystallization Resistance.....	49
1.2.1 Optimizing the Precipitate Distribution.....	49
1.2.2 Mechanisms of Recrystallization.....	51



1.2.3 Particle Stimulated Nucleation.....	52
1.2.4 Predicting Recrystallized Grain Size during Static Annealing.....	53
1.3 Mitigation of Dendritic Segregation.....	55
1.4 Scope of this Contribution.....	56
2 Methods.....	57
2.1 Casting.....	57
2.2 Thermomechanical Processing.....	58
2.3 Optical and Electron Microscopy.....	59
3 Results.....	60
3.1 Alloying Levels.....	60
3.2 Optical and Electron Microscopy.....	61
3.2.1 As-cast Microstructures.....	61
3.2.2 Thermomechanically Processed Microstructures.....	65
4 Discussion.....	71
4.1 Grain Size Determination and As-cast Observations.....	71
4.2 Changes in Hardness and Conductivity during TMP.....	75
4.3 Low- and High-Angle Grain Boundaries.....	77
4.4 Theoretical vs. Observed Recrystallized Grain Size.....	81
4.5 Other Factors and Limitations.....	82
5 Conclusions.....	83
<b>List of References.....</b>	<b>85</b>
<b>Appendix I: Metallographic Preparation.....</b>	<b>91</b>
<b>Appendix II: Multi-step Aging Conductivity Curves.....</b>	<b>93</b>
<b>Appendix III: Casting X-Ray Images.....</b>	<b>95</b>
<b>Appendix IV: All Available Raw Material Certification Sheets.....</b>	<b>99</b>

## Preface

This dissertation is written in two chapters, each intended to be published in part or wholly as journal articles. In terms of contributions to this work, Professor Steve Kampe clarified the discussion of strengthening mechanisms in Sections 1.2 and 4.3 and provided valuable feedback during the entire data collection and writing process. Many useful recommendations for additional analysis were also given by Assoc. Prof. Paul Sanders, Assoc. Prof. Doug Swenson, and Asst. Prof. Scott Wagner throughout. Brian Milligan, an undergraduate research assistant, collected the second series of isothermal aging data presented in Figure 12. Owen Mills, Director of the Applied Chemical and Morphological Analysis Laboratory (ACMAL), provided training and expertise in SEM and TEM data collection. A great friend, colleague, and talented microscopist, Jerome Cornu, enabled quality electron backscattered diffraction data collection for Chapter II, and Dr. Thomas Dorin assisted with the analysis thereof; both of these researchers reside at the Institute for Frontier Materials at Deakin University in Victoria, Australia. All other data was collected and analyzed by the author. Both chapters were written *in toto* by the author, other than the aforementioned edits.



## Acknowledgments

*This work would not have been possible without financial, moral, and technical support from the following agencies, faculty, staff, post-docs, graduate students, and undergraduate students.*

United States Office of Naval Research N00014-11-10876, Sponsor: Dr. William Mullins  
The Applied Chemical and Morphological Analysis Laboratory (ACMAL) at Michigan Tech  
The Institute for Frontier Materials (IFM) at Deakin University  
The Franklin and Lorraine St. John Trust  
Doctoral Finishing Fellowship, Michigan Tech Graduate School

Prof. Steve Kampe, Prof. Paul Sanders, Prof. Doug Swenson, Prof. Scott Wagner, Prof. Jarek Drelich, Prof. Walt Milligan, Prof. Dieter Adolphs, Prof. Matt Barnett, Dr. Thomas Dorin

Owen Mills, Tom Wood, Paul Fraley, Pat Quimby, Dan Seguin, Jennifer Eikenberry, Jason Griffin, Ruth Kramer, Andrew Sullivan

Dr. Patrick Bowen, Dr. Amberlee Haselhuhn, Dr. Joe Licavoli, Dr. Helen Rau, Dr. Jan-Marten Seitz, Jerome Cornu, Kyle Deane, Marcel Kerkove, Alex Poznak, Karl Warsinski, Shan Zhao, Janine Erickson, Shane Anderson, Brian Milligan, Cam Smith, and Rachel McCollough



## Abstract

Critical exploration of the minimalistic high strength low alloy aluminum (HSLA-Al) paradigm is necessary for the continued development of advanced aluminum alloys. In this study, scandium (Sc) and zirconium (Zr) are examined as the main precipitation strengthening additions, while magnesium (Mg) is added to probe the synergistic effects of solution and precipitation hardening, as well as the grain refinement during solidification afforded by a moderate growth restriction factor. Further, pathways of recrystallization are explored in several potential HSLA-Al systems sans Sc. Aluminum-titanium-boron (Al-Ti-B) and aluminum-titanium-carbon (Al-Ti-C) grain refining master alloys are added to a series of Al-Zr alloys to examine both the reported Zr poisoning effect on grain size reduction and the impact on recrystallization resistance through the use of electron backscattered diffraction (EBSD) imaging.

Results include an analysis of active strengthening mechanisms and advisement for both constitution and thermomechanical processing of HSLA-Al alloys for wrought or near-net shape cast components. The mechanisms of recrystallization are discussed for alloys which contain a bimodal distribution of particles, some of which act as nucleation sites for grain formation during annealing and others which restrict the growth of the newly formed grains.



## Introduction: The Case for HSLA-Al

Developments in aluminum alloying technology have realized the potential of the elements scandium (Sc, atomic number,  $Z = 21$ ) and zirconium (Zr,  $Z = 40$ ) when used in impurity-like quantities, and the steady evolution of imaging methods has advanced to atomic resolution so we can see why and how this works so efficiently. However, in practice, these two dilute additions cannot be made alone without complication. Grain sizes tend to be large and columnar (See Figure 1), making the structures virtually unusable. Strategies, whether through alloying or recrystallization, are needed to refine grain size and create macroscopically isotropic microstructures.

Empirically, as with all alloys, each element here is chosen because it is the best option for its role in developing a useable microstructure, and in most cases each serves more than one purpose. Scandium has been shown to be highly effective, per atom, for strengthening aluminum. Zirconium, which exhibits very limited interdiffusivity in aluminum, has been found to effectively stabilize the scandium-rich precipitates; this symbiotic relationship results in coarsening resistant particles which act as the primary strengthening phase. Titanium has been found to be a powerful segregant during solidification and optimizes conditions for nucleation of new grains in front of the solid-liquid interface, where borides or carbide particles can be added which act as fertile aluminum nucleation sites from which to grow. And magnesium, with high solubility in aluminum, provides strengthening by just sitting around and always feeling a little out-of-place in addition to as-cast grain refinement through a moderate eutectic growth restriction factor. All of these properties rely on mechanisms of slowing down boundaries, whether they are grain boundaries (macroscale), subgrain boundaries (microscale), or dislocations (nanoscale). Models associated with these mechanisms are presented and discussed in all cases.

While we know much about how each of these individual elements will affect the properties of the alloy during certain stages of development, there are un-answered questions regarding the response to thermomechanical processing. It is uncertain what consequences cold work has on the development of nanoscale trialuminide precipitates during aging; understanding how these changes affect engineering properties when using Sc,



Zr, and Ti is prudent. Chapter I addresses this uncertainty as well as examines the combinations of strengthening mechanisms in these alloys in an effort to reduce the amount of required Sc. In Chapter II, a discussion is provided that addresses how trialuminides, and especially  $\text{Al}_3\text{Zr}$ , extensively block grain growth during recrystallization and how the addition of  $\text{TiB}_2$  or  $\text{TiC}$  alters kinetic and thermodynamic barriers to nucleation and grain growth during recrystallization. The interaction between these effects warrants the investigation performed at the end of this contribution.

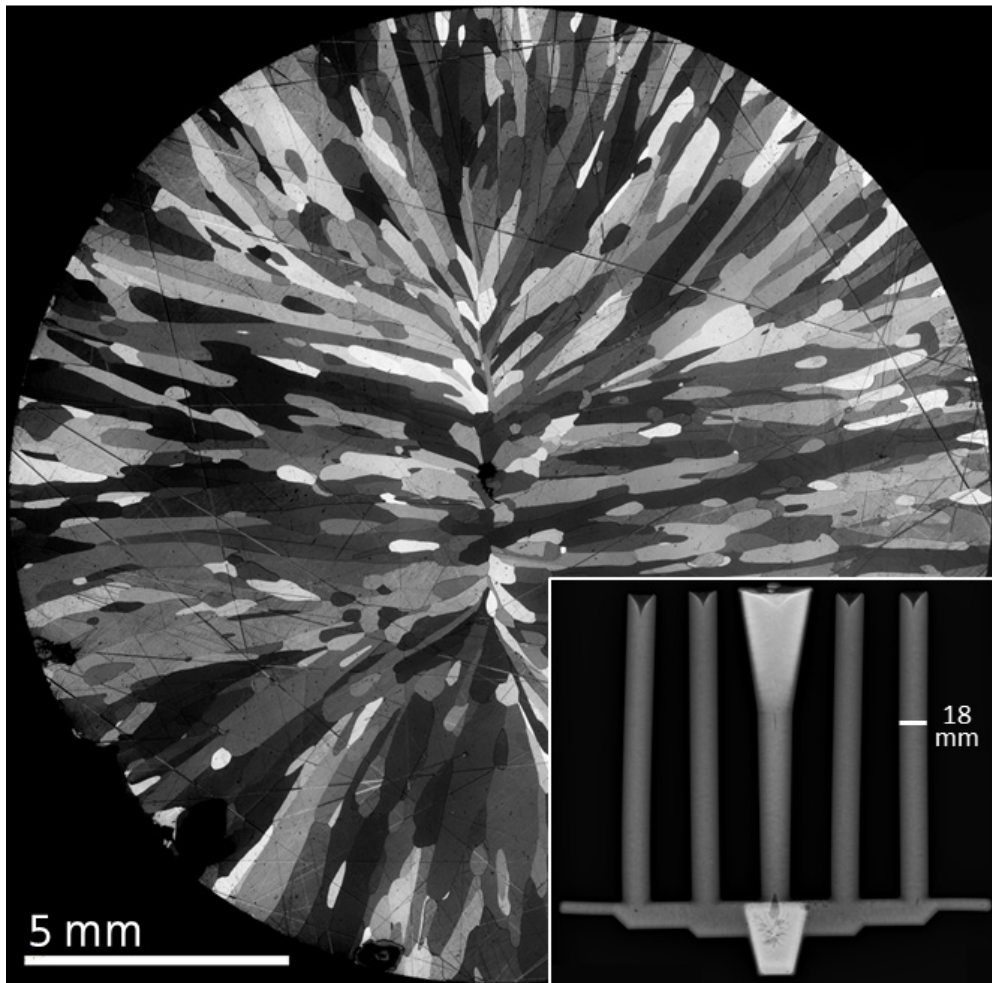


**Figure 1:** As-cast grain structure of Al-0.054 Sc-0.061 Zr revealed by polarized light microscopy on a polished and anodized cross section. Nucleation of grains occurs at the melt/mold interface during an isothermal freezing event and then grow inward resulting in large columnar grains. (Inset) Digital X-ray image of a pure aluminum casting; the scale bar indicates where the anodized cross section was taken and the initial cooling rate was measured for the Al-0.054 Sc-0.061 Zr alloy.

# Chapter I: Precipitation Strengthening of Dilute Al Alloys <sup>1</sup>

## 1. Introduction

### 1.1 Diffusion and Characteristics of Trialuminides

Combined alloying additions of scandium and zirconium in aluminum represent a promising strategy to impart strengthening and microstructural stability at temperatures above half the melting point of aluminum [1-6]. The interdiffusion of scandium in aluminum is roughly three orders of magnitude slower than copper at 400° [7], while zirconium is approximately six orders slower [8], as illustrated through the Arrhenius relationships in Figure 2; interdiffusion constants and references are given in Table 1. Upon aging, the slow diffusivities and good lattice matching of the trialuminide phases of both Sc and Zr result in coherent, nanosized trialuminide precipitates. The presence of these precipitates improves mechanical properties such as elevated temperature strength [9, 10] and creep resistance [5, 11-20] due to their resistance to Ostwald ripening [21, 22] attributable to the extremely low matrix solubilities and slow diffusion rates. However, the maximum solubilities of Sc and Zr in liquid Al around 665°C are 0.233 at% [23] and 0.033 at% [24] resulting in a maximum equilibrium trialuminide volume fraction ( $f$ ) of only about 1.25% at room temperature by lever-rule estimations. As such, dispersoid sizes must be kept very small to achieve small spacings between particles to maximize obstruction of dislocation motion. In addition to dilute aluminum-transition metal (Al-TM) base alloys, it is envisioned that Sc-Zr stabilization and strengthening strategies can be additively applied to conventional aluminum alloys, or otherwise create strengthening opportunities for ambient and elevated temperature applications in essentially pure aluminum.

The driving force behind the development of HSLA-Al alloys is minimalism in alloy design, following on the HSLA paradigm set in the steel industry some 30 years ago. Using as little alloying elements as possible has several benefits including decreased micro galvanic potentials leading to lower corrosion rates, lower cost in the incorporation of alloying additions, well-understood production and processing techniques, and less build-up of

---

<sup>1</sup> The content of Chapter I is intended to be submitted for journal publication.

alloying additions during recycling operations over time. Much influence has been drawn from the Seidman and Dunand research group at Northwestern University, and especially from the thorough and detailed work of former Northwestern graduate student Dr. Keith Knippling from 2006-present, whose work is cited often herein.

A key feature of the Sc addition is low lattice misfit (2.2% at room temperature) between the  $L1_2$   $Al_3Sc$  and FCC aluminum which permits homogeneous coherent nucleation upon aging at 275-300°C and results in a very high number density of intragranular nuclei [4, 14, 25] while zirconium essentially remains in solution due to kinetic limitations. A second heat treatment step at 400-425°C allows  $Al_3Zr$  to nucleate and form as a metastable  $L1_2$  coherent shell on existing  $Al_3Sc$  precipitates [21, 25-27] thereby increasing their size, decreasing interprecipitate spacing, and approximately preserving the precipitate number density. Additionally, the core/shell nature often exhibits enhanced resistance to Ostwald ripening compared to what would be expected for uncoated  $Al_3Sc$  [22]. This may be attributed to the low interdiffusion rate of Zr itself, and the lower misfit (1.6%) of the  $Al_3Zr$  shell producing additional mechanical barriers to diffusion of Sc out of the precipitates. This has also been shown to be effective in Al-Sc-Ti [19] by the same mechanism.

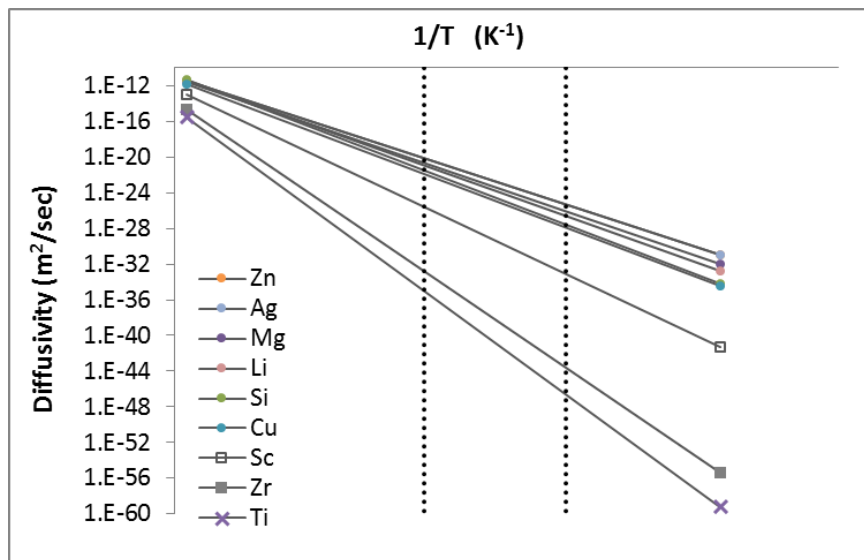


**Figure 2:** Arrhenius relationships for interdiffusion of various alloying additions in aluminum. Diffusion constants for the species above are given in Table 1 with references.

**Table 1:** Intrinsic diffusivity and activation energy for diffusion for various alloying additions in aluminum. The slowest diffusivities reside at the bottom of the table, in the same order as in Figure 2.

	$D_0$ (m <sup>2</sup> /s)	$Q_d$ (kJ/mol)	Ref.
Zn	$1.19 \times 10^{-5}$	116	Du [28]
Ag	$1.18 \times 10^{-5}$	116	Peterson [29]
Mg	$1.49 \times 10^{-5}$	121	Du [28]
Li	$5.30 \times 10^{-5}$	127	Minamino [30]
Si	$2.02 \times 10^{-4}$	136	Fujikawa [31]
Cu	$4.44 \times 10^{-5}$	134	Du [28]
Sc	$2.65 \times 10^{-4}$	168	Kerkove [7]
Zr	$7.28 \times 10^{-2}$	242	Marumo [8]
Ti	$1.12 \times 10^{-1}$	260	Knipling [5]

## 1.2 Strengthening Mechanisms

The yield strength of a metal may be increased by adding “soft” or “hard” obstacles to dislocation motion. Soft obstacles are generally defined to include features that allow dislocations to pass “through” with crystallographic continuity, while hard obstacles necessitate dislocations to bypass for continued movement. Thus, soft obstacles to dislocation motion include the strain fields present due to, for example, solute and to dislocations. Coherent precipitates, by virtue of their crystallographic continuity, often act as soft obstacles to dislocation motion. Hard obstacles include dislocation lines, incoherent precipitates, and high-angle grain boundaries; each of these share the common characteristic of a crystallographic discontinuity that forces dislocations to bow around and/or to move within the volume that exists between their spacings.

Semiquantitatively, individual mechanisms of strengthening for metals can be treated as being additive. The most general description of the concept of additive strengthening can be illustrated as

$$\sigma_y = \sigma_0 + \Delta\sigma_s^m + \Delta\sigma_p^n + \Delta\sigma_D^o + \Delta\sigma_{GS}^p + \Delta\sigma_i^q \quad \text{Equation 1}$$

where the individually-identified mechanisms of strengthening additively contribute to the overall strength of an alloy. Here,  $\sigma_0$  is the yield strength of the material without the

obstacles considered in subsequent terms. Increments illustrated above include those attributable to solute ( $\Delta\sigma_s$ ), particles ( $\Delta\sigma_p$ ), dislocations ( $\Delta\sigma_D$ ), grain size ( $\Delta\sigma_{GS}$ ), and any other conceivable mechanisms that may be present ( $\Delta\sigma_i$ ). In this general form, the individual mechanisms of strengthening are discounted through their respective exponents ( $m$ - $q$ , above), depending on the degree of their independence from the other operative mechanisms. For example, exponents with values of unity (linear additivity) implies complete independence of the mechanism from the others operating; exponents less than unity implies a degree of mechanistic overlap.

As an example, Hornbogen and Starke [31] presented an additivity equation as an approximation to how several mechanisms increase yield strength ( $\sigma_y$ ) of modestly alloyed aluminum by a summation of the individual contributions according to Equation 2.

$$\sigma_Y = \sigma_o + \Delta\sigma_s + (\Delta\sigma_p^2 + \Delta\sigma_D^2)^{1/2} + \frac{k_Y}{\sqrt{d_g}} \quad \text{Equation 2}$$

In Equation 2,  $\sigma_o$  is the as-cast, or fully annealed, yield strength of aluminum,  $\Delta\sigma_s$  is the contribution by solute atoms, which is easily measured in as-cast single-phase material,  $\Delta\sigma_p$  and  $\Delta\sigma_D$  are the contributions from larger precipitates and dislocation lines (i.e. hard obstacles), respectively, and the last term is the Hall-Petch relation for  $\Delta\sigma_{GS}$  where  $k_Y$  is a material dependent constant and  $d_g$  is the grain size.

### 1.2.1 Precipitation, Dislocation, and Solute Strengthening

Interactions between dislocations and coherent precipitates are tied closely to changes in the energy of the dislocation line ( $E_D \approx Gb^2$ ) as it enters and moves through the volume of the precipitate. For example, differences in shear moduli between the matrix and coherent precipitate will serve to either increase or decrease the energy of the segment if dislocation line that resides within the precipitate, creating a repulsion or anchoring effect to the movement of the dislocation. An empirical relation for modulus hardening is given in Equation 3. Similarly, the creation of coherency strain associated with the lattice mismatch will serve as a soft strengthening obstacle (Equation 4). Order strengthening, given by Equation 5 [32], arises from the creation of anti-phase boundaries during shearing of coherent particles and occurs in series to the previous two mechanisms which act together.

$$\Delta\sigma_{Mod} = 0.0055Mb(G_P - G_{Al})^{3/2} \left(\frac{2f}{G_{Al}b^2}\right)^{1/2} \left(\frac{R}{b}\right)^{\frac{3p}{2}-1} \quad \text{Equation 3}$$

$$\Delta\sigma_{Coh} = \chi M(\varepsilon G_{Al})^{3/2} \left(\frac{2Rf}{0.36G_{Al}b}\right)^{1/2} \quad \text{Equation 4}$$

$$\Delta\sigma_{Ord} = M \cdot 0.81 \frac{\gamma_{APB}}{2b} \left(\frac{3\pi f}{8}\right)^{1/2} \quad \text{Equation 5}$$

In Equations 3-5 as applied to Al-Sc-Zr alloys,  $R$  is the average particle radius,  $M$  is the Taylor factor for FCC,  $G_P$  is the shear modulus of the particle,  $G_{Al}$  is the shear modulus of aluminum, and  $b$  is the magnitude of the Al Burger's vector. In Equation 4,  $X$  is a constant,  $\delta$  is the lattice mismatch where  $\varepsilon_{Al_3X} = \frac{|a_{Al} - a_{Al_3X}|}{a_{Al}}$  for  $Al_3Sc$  ( $a = 0.4103$  nm [33]) and  $Al_3Zr$  ( $a = 0.408$  nm [34] and  $a_{Al} = 0.4014$  nm [35]), and  $p$  is an empirically determined constant. Lastly, for Equation 5,  $\gamma_{APB}$  is the anti-phase boundary energy for the close-packed (111) plane, since this is the most likely plane on which slip occurs.

A commonality among the mechanisms associated with coherent particles is that strengthening increments tend to increase with increasing precipitate size. However, coherency strengthening mechanisms tend to have an upper limit associated with a critical precipitate size where crystallographic coherency becomes energetically unfavorable and will no longer be maintained.

Once coherency is lost or if it is not energetically favorable for dislocations to move within precipitates, i.e. as the particles grow, dislocations may instead bend around them and form loops, and the strength increment approximates to Equation 6 [36]. This process is known as Orowan strengthening and is inversely proportional to the spacing between precipitates and decreases with average precipitate radius. More detailed analyses have been carried out to find an empirically closer relation, and Equation 7 [37] is used here.

$$\Delta\sigma_{Orowan} \approx \frac{G_{Al}b}{\lambda_P} \approx \frac{G_{Al}b\sqrt{f}}{2R} \quad \text{Equation 6}$$

$$\Delta\sigma_{Orowan} = M \cdot \frac{0.4 \cdot G_{Al} \cdot b}{\pi\sqrt{1-\nu}} \cdot \frac{\ln\left(\frac{2R}{b}\right)}{\lambda_P} \quad \text{Equation 7}$$

where, for Al-Sc-Zr alloys,  $\nu$  is Poisson's ratio for Al [38] and for a monodispersed population of precipitates, the mean planar radius is  $\bar{R} = \frac{\pi}{4}R$ . The edge-to-edge interprecipitate spacing,  $\lambda_p$ , is given by Equation 8 [32, 39].

$$\lambda_p = \left( \sqrt{\frac{2\pi}{3f}} - \frac{\pi}{2} \right) R \quad \text{Equation 8}$$

The precipitation strengthening mechanisms discussed above are illustrated in Figure 3 as a function of mean precipitate radius for  $f$  of 0.46%. At small radii, only the maximum of  $(\Delta\sigma_{\text{Mod}} + \Delta\sigma_{\text{Coh}})$  or  $\Delta\sigma_{\text{Ord}}$  manifests itself in the observed yield strength, and therefore  $\Delta\sigma_{\text{Ord}}$  is the parameter used at radii  $< 0.5$  nm (effectively, 1 unit cell radius), while the  $(\Delta\sigma_{\text{Mod}} + \Delta\sigma_{\text{Coh}})$  shearing effects are dominant for radii of about 0.5 – 1.0 nm (1-2 unit cell lengths). Maximum precipitation strengthening is predicated to occur at the transition from shearing precipitates to Orowan bowing; this value is known as the critical radius,  $R_{\text{crit}}$ .

The actual strengthening by dislocation-dislocation interactions as a function of their density, or % cold work, is difficult to model and requires detailed computational tools such as finite element modeling. A simple and oft-used empirical relation for work hardening, however, is presented as Equation 9 [40]:

$$\Delta\sigma_D = \alpha G_{Al} b \sqrt{\Delta\rho_D} \quad \text{Equation 9}$$

where  $\alpha$  is a constant on the order of 0.5 [41], and  $\Delta\rho_D$  is the increase in density of free dislocations during cold work, typically on the order of  $10^6$  /m<sup>2</sup> for as-cast aluminum, which tends to plateau around  $10^7$  for aluminum cold worked 20-200% [42]. This is because dislocations in aluminum readily congregate to form subgrain structure consisting of low-angle grain boundaries, reducing the effective grain size, which is then treated in the Hall-Petch manner mentioned above.

A general approximation for the strengthening due to elements in solution relies on the misfit resulting from differences in atomic radii,  $\delta$ . Equation 10 is the empirically derived relation from Bowman [38] where  $c_s$  is the concentration of solute,  $\beta$  is typically between 0.5 and 1, and  $\xi$  is an empirical constant, easily found from as-cast hardness or yield strength measurements.

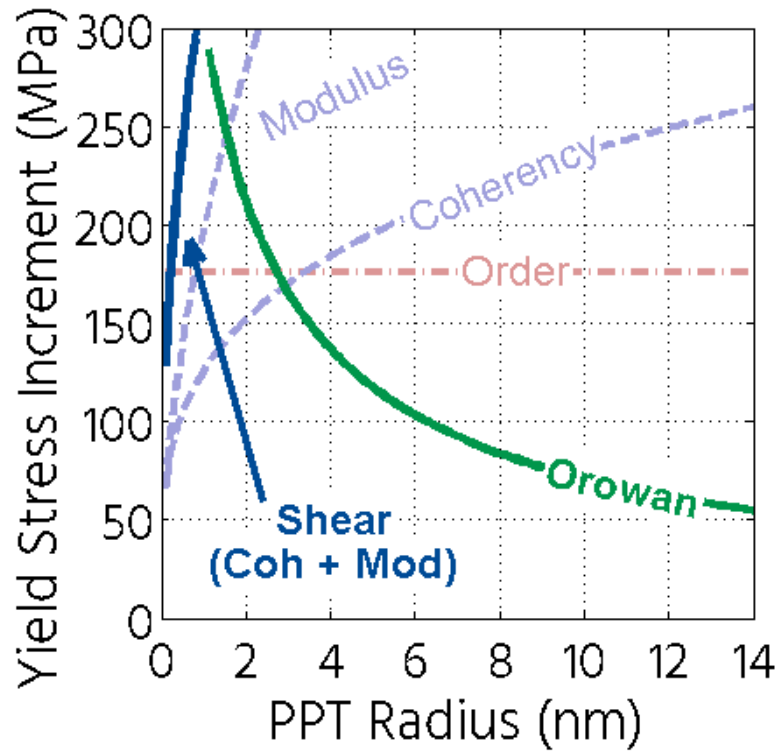


**Figure 3:** Predicted dispersion strengthening due to a 0.46% volume fraction of scandium trialuminide for an Al-0.12 at% Sc alloy. The transition from dislocation shearing of precipitates to bowing is predicted to occur at  $R_{crit} = 1$  nm. Equation 7 is used for the Orowan strengthening approximation here.

$$\Delta\sigma_S = \xi G_{Al} \delta^{3/2} c_S^\beta \quad \text{Equation 10}$$

In the interest of forming an optimized precipitate distribution, there is one characteristic in the literature [14, 18, 43] which stands out: multi-step aging (referred to as “isochronal aging” elsewhere, a misnomer in the author’s opinion). This innovative aging scheme works by starting aging treatments at a low temperature and incrementally increasing temperature after a set amount of time at each temperature. At low temperatures, widespread nucleation is encouraged, then at slightly higher temperature growth of the first to precipitate phase is encouraged, and finally precipitation and growth of the slowest diffusing species occurs at higher temperatures. In the case of Al-Sc-Zr alloys, Zr is the last to come out of solution, and happens to precipitate on existing  $Al_3Sc$  precipitates



which has many benefits as discussed previously. Also, conveniently, this type of aging can be performed on a single, small sample, by a heat-quench-measure-repeat process, allowing a large amount of data to be gleaned from a single sample.

### 1.3 Existing Alloys

Researchers in the former USSR (namely M.E. Drits, N.I. Turkina, E.S. Kadaner, TV Dobatkina, L.S. Toropova, Y.G. Bykov, V.E. Elagin, and Y.A. Filatov, among others) recognized the potent hardening potential of scandium in aluminum in the 1970s [44], following the patent filed by L.A. Willey of Alcoa in 1971 [45], which ultimately led to commercial success of alloy 1570 with a composition in the realm of Al-5 Mg-0.4 Mn-0.1 Ti-0.03 Sc-0.01 Zr (wt%). The most recent incarnation of this alloy, 1570c, is designed for use in reusable rocket components and other aerospace structures and has the ability to be superplastically formed at temperatures near 500°C and strain rates on the order of  $10^{-2} \text{ s}^{-1}$  [46], making this a feasible high volume production alloy that can be formed into complex aerospace components. The stockpile of rare-earth ores and metals in Russia gives the country a competitive edge in this market; scandium is relatively rare in the local cosmic region (see Figure 4) and is difficult to refine [4] (although this is an active area of research) and therefore very expensive in most other places in the world, often making the development of high volume production alloys economically unviable.

### 1.4 HSLA-Al Alloys sans Scandium

In the absence of scandium, zirconium has been shown to be a somewhat effective precipitation strengthener [47, 48], but not nearly as effective as scandium. The lower capacity to strengthen the aluminum matrix does not exclude Zr as the primary alloying addition, however, as the  $\text{Al}_3\text{Zr}$  precipitates have been shown to be highly effective at preventing recrystallization leading to benefits in high temperature strength and creep resistance. Many applications of aluminum alloys do not require extremely high strength, and this represents potential for HSLA-Al systems sans Sc. These systems would likely need additional alloying to refine grain size, using elemental additions such as Mg or Mn, or particle-containing master alloys such as Al-Ti-B or Al-Ti-C. In such alloys, Zr will remain in solution and precipitate later as fine and coherent  $\text{Al}_3\text{Zr}$ . The relatively mild strengthening

potential of these alloys following thermomechanical processing (TMP) and as a function of heat treatment and is examined experimentally here, while the grain refinement strategies and recrystallization resistance is the focus of Chapter II.

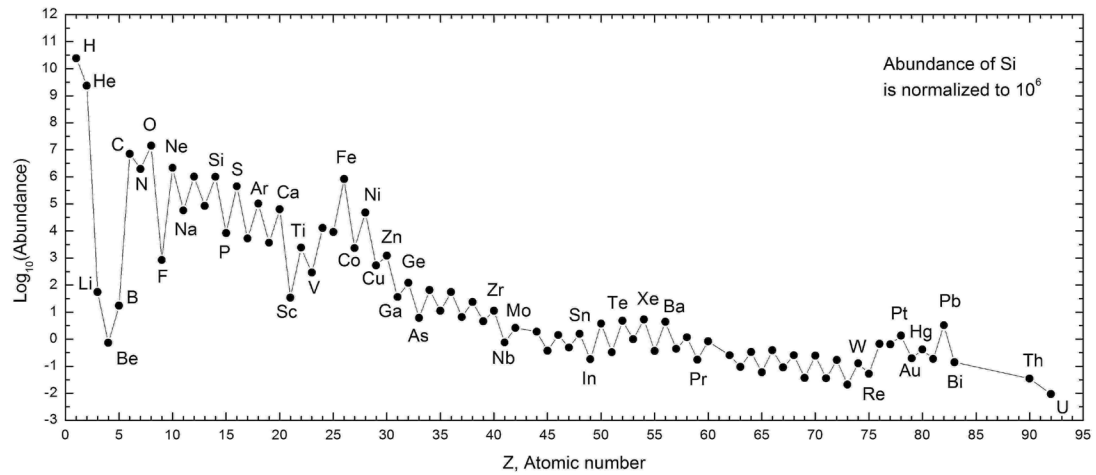


**Figure 4:** Abundance of elements in the Solar System; scandium is rare in comparison to neighboring elements on the periodic table. Source: en.wikipedia, creative commons, uploader: 28bytes

### 1.5 Scope of the Current Study

The maximum microhardness values for Al-Sc-Zr and Al-Mg-Sc-Zr alloys are compared to Al-Zr based alloys following multi-step aging to directly illustrate the strengthening potential of the Al-TM alloys. An optimized TMP route is developed through a series of cold work and aging experiments which track microhardness as a function of aging time and temperature on both as-cast and cold worked variants. Conductivity is also tracked during multi-step aging to assess when precipitation is complete, and if the precipitated phases begin to re-dissolve at high temperatures. In addition, maximum room temperature yield stress increase following thermomechanical processing (TMP) is measured through tensile testing several alloys based on Al-0.06 Sc-0.06 at% Zr with and without Mg. Precipitates resulting from aging are observed using transmission electron microscopy (TEM) and particle size and spacing data is collected to compare the actual to predicted strengthening contributions based on hard and soft obstacle strengthening models.

The main goal of this contribution is to critically examine the effects of as-cast grain size reduction, cold work, and solute incorporation on the age-hardening potential for HSLA-Al alloys to determine if it may be possible to circumvent the use of expensive scandium in these alloys. Specifically, the following hypothesis has been formulated to guide experimentation and analysis:

- 1) If alternative strengthening mechanisms to precipitation hardening (solute, Hall-Petch, and cold work) are incorporated into design and production of HSLA-Al alloys, the necessity for the potent strengthening from  $\text{Al}_3\text{Sc}$  can be partially or wholly mitigated.

The conclusions in Chapter I of this study advise the formulation and optimal TMP for prototypical high-strength low alloy aluminum which could have a number of applications in the transportation sector.

## 2. Methods

### 2.1 Casting

The casting process for Al-Sc-Zr and Al-Mg-Sc-Zr alloys consisted of liquefying large slices of 99.99 wt% Al ingots (Belmont Metals, Brooklyn, NY) through induction heating at 30kW in a graphite crucible under argon cover flow, rotary degassing with commercial purity argon through a graphite lance at a melt temperature of 850°C, adding sections of C.P. Mg (Alfa Aesar, Ward Hill, MA), Al-2.1 wt% Sc master alloy (Stanford Advanced Metals, Irvine, CA), and Al-10.2 wt% Zr master alloy (KBM Affilips, Oss, The Netherlands), then heating and holding the melt for 10 minutes at 900°C. The melt was allowed to cool to 760°C and poured into a cast iron permanent mold coated with boron nitride (BN) (ZYP, Oak Ridge, TN) release agent. This coating helps avoid impurity iron pickup during pouring and allows the castings to be extracted easily. Castings were cooled in-mold for about 10 minutes and then removed from the mold; subsequent cooling proceeded in open air. The crucible used for melting held enough material for seven pours per heat, so a new casting was poured as soon as possible following shakeout of the previous casting. This meant that subsequent castings were poured into a very warm mold, and the cooling rates were much slower. Cooling rates for

several castings were monitored via bare wire type-k thermocouples. Each casting produced four bars, 18.4 mm in diameter, and a total usable length of roughly 650 mm, depending on depth of the shrinkage wells at the tops of the bars. Thin slices from several bars in the castings were taken using a low-speed diamond saw to be dissolved for compositional analysis.

A similar casting process was used in the case of Al-Zr based alloys. Special preparation was undertaken to ensure that as much Zr as possible remained in solution during the casting and solidification process. The bulk master alloy acquired was 10.2 wt% Zr and therefore contained very coarse  $\text{Al}_3\text{Zr}$  precipitates which can be difficult to dissolve in small scale melting experiments. As such, 4 kg of diluted master alloy with target composition of 0.388 wt% was first cast using a tilting induction furnace in the pilot scale foundry at Michigan Tech in a method similar to that described above. Pure aluminum was melted in the graphite crucible under argon cover gas and heated to 850°C measured via stainless steel sheathed type-K thermocouple. The Al-Zr master alloy was then added and induction heating resumed to  $950 \pm 10^\circ\text{C}$ ; this temperature and stirring was maintained for 10 minutes. The melt was then hydraulically tilt-poured into a graphite ladle and poured into a trough style mold coated with BN mold release which produced triangular bars with open air cooling, shown in Figure 5. An internal type-k thermocouple was used to measure the cooling rate of several bars. The remainder of the melt was held at the pouring temperature until shakeout of the first set of bars, at which point a second set of bars was poured in the same manner, although into a warmer mold. These bars were also shaken out as quickly as possible.

The diluted Al-Zr master alloy produced above was then melted with additional pure aluminum in a custom vacuum induction melter (VIM) (Michigan Tech, Houghton, MI) under argon cover gas to 750°C as measured via pyrometer and type-k thermocouple; this melt was held and stirred at 750°C for 30 seconds. Grain refining additions of Al-10 wt% Ti master alloy (Milward, Minneapolis, MN), Al-5 Ti-1 wt% B (AMG Aluminum, Robards, KY) or Al-3 Ti-0.15 wt% C (KBM Affilips, Oss, The Netherlands) were added at the 30 second mark and stirring continued for 60 seconds at 750°C. All compositions were stirred for a total of 90 seconds prior to pouring. A computer controlled servo motor was used to tilt-pour the melt

into a room temperature BN-coated steel mold. A bare wire type-k thermocouple in direct contact with the incoming molten aluminum recorded solidification and cooling rate in situ. Once the solidification isotherm ended and the casting cooled to 100-200°C, it was removed from the mold and cooled in air to room temperature. Chips for compositional analysis were removed from these castings using a clean, unlubricated drill. The single casting pours using this method allowed each composition to be poured into a room temperature mold, so initial cooling rates were ~25 times faster than castings from the foundry.

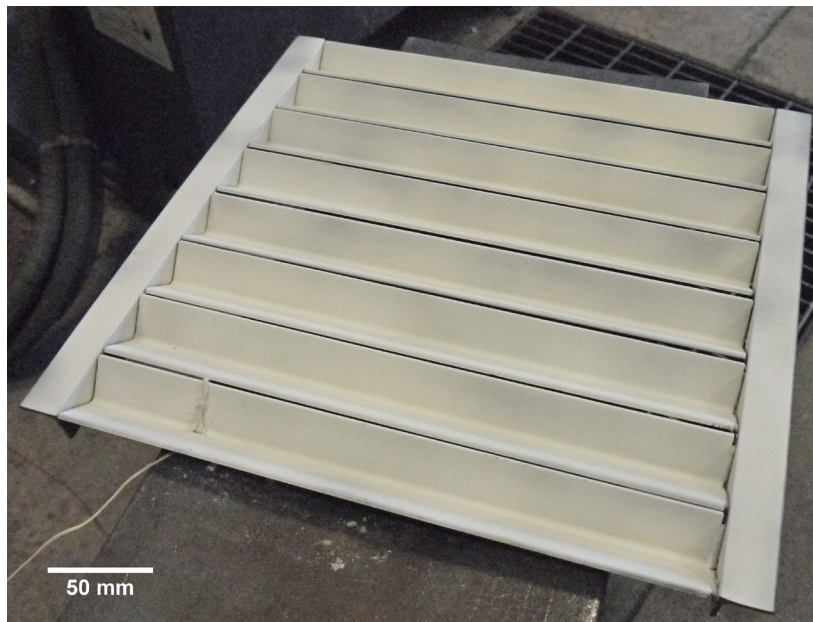


**Figure 5:** Boron nitride coated trough mold used to produce diluted Al-Zr master alloy.

## 2.2 Thermomechanical Processing

Cold-work (CW) was performed at room temperature in a Fenn 3F-2 rotary swager (SPX Corporation, Newington CT) which reduced the as-cast bars sequentially to diameters of 17.5 (9.5% CW), 15.9 (25.3% CW), and 14.4 (38.8% CW) mm. Short term storage was nominally at room temperature. Aging treatments were conducted in box furnaces with a temperature controller calibrated via a bare wire type-K thermocouple positioned next to

the samples. Three types of aging treatments have been examined in this and prior work by the author: isochronal, isothermal, and multi-step. The terminology used corresponds to the heat treatment schemes shown schematically in Figure 6 where isochronal refers to measurements taken after a fixed time interval at a range of temperatures, isothermal refers to measurements taken at several time points at a single temperature, and multi-step refers to measurements taken on the same sample after successive intervals at ever-increasing temperatures. Multi-step aging was performed on all compositions, single and double isothermal aging regimens (where a second isothermal schedule follows the first) were performed on as-cast and as-cold worked samples of Al-0.06 Sc-0.06 at% Zr, and isochronal aging was performed on Al-0.06 Sc-0.06 at% Zr at several levels of cold work to assess changes in initial precipitation behavior.

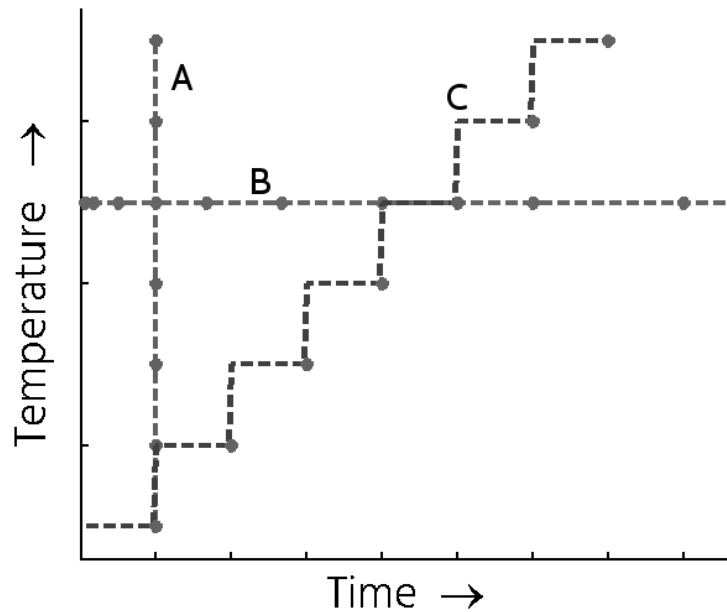


**Figure 6:** Schematic of heat treatment schedules for A) isochronal, B) isothermal, and C) multi-step aging.

For tensile bars from the Al-0.056 Sc-0.058 at% Zr alloy, cast bars were cold worked 38% ( $\varnothing$ 14.4 mm). Half of the bars were then placed in a box furnace at 638°C (above the binary solvus temperature for 0.061 Zr) for 1 hour and quenched in an attempt to achieve a recrystallized and equiaxed grain structure and a homogeneous solute distribution. Artificial

aging was then performed in a convection box furnace from both the as-cold worked and as-homogenized state.

The other compositions that underwent tensile testing (Al-0.063 Sc-0.064 Zr, Al-0.117 Sc-0.028 Zr, Al-1.72 Mg-0.105 Sc-0.049 Zr, and Al-3.88 Mg-0.110 Sc-0.066 at% Zr) were aged from the as-cast condition using a crucible furnace filled with a mixture of 50/50 potassium nitrate/sodium nitrite salt; aging times and temperatures were selected based on results of precipitation hardening studies.

### 2.3 Macroscale Imaging and Compositional Analysis

Transverse and longitudinal sections of the as-cast bars were cut on a high-speed diamond saw, mechanically polished, anodized in either Barker's reagent (3.5%  $\text{HBF}_4$ ) or a 2% HF solution at room temperature, and examined under polarized light utilizing a Nomarski interference contrast filter and a color tint filter on a PMG-3 inverted microscope (Olympus, Tokyo Japan). Porosity was assessed through digital x-ray imaging of select castings on a BuckyDiagnost system (Philips Healthcare, Andover MA) and a SOMATOM Sensation 64 Computed Tomography (CT) scanner (Siemens Healthcare, Malvern PA) at UP Health System-Portage Hospital and Archimedes density measurements on sections of cast and swaged bars. A Perkin Elmer 7000DV Inductively Coupled Plasma Optical Emission Spectrometer (ICP-OES) (Waltham MA) was used to determine alloy compositions including impurity levels. A JSM-6400 (JEOL, Peabody MA) scanning electron microscope (SEM) was used on as-cast samples to check for large primary precipitates and undissolved intermetallic compounds from the master alloys using backscattered electron imaging (BEI).

### 2.4 Microhardness, Conductivity, and Tensile Testing

Microhardness was measured as a function of aging time and temperature on a LECO Vickers microhardness tester (St. Joseph MI). A minimum of 10 indentations were made per sample (one sample per temperature/time step) across multiple grains using a 0.2 kg load and 5 second dwell time; most measurements are averaged from 15 indentations. Conductivity was measured using a Sigmascope SMP10 with an ES40 conductivity probe (Fischer Technology, Windsor CT).

ASTM B557 sub-sized tensile bars were machined from the double aged Al-Sc-Zr and Al-Mg-Sc-Zr bars, with a gage diameter and length of 8.71 and 48.3 mm, respectively. These samples were tested in uniaxial tension at a strain rate of  $5 \times 10^{-4} \text{ s}^{-1}$  on an Instron 4206 frame with a 150 kN load cell (Grove City PA).

## 2.5 Electron Microscopy

TEM examination was performed using a JEOL JEM-2010 (Peabody MA) high resolution microscope outfitted with an Orius SC200 high-speed digital camera (Gatan, Inc., Pleasanton CA). The high-brightness LaB<sub>6</sub> emitter was operated at 200kV to capture bright field images appropriate for measurement of precipitate sizes using the NIH ImageJ open source software from grip sections of tensile bars. Tensile fracture surfaces were imaged in the JSM-6400 SEM using secondary electron imaging (SEI).

## 3. Results

### 3.1 Cooling Rates and Compositions

Data acquisition from internal thermocouples near the top and center of an outermost bar give an initial cooling rate of 1.3°C/sec for the third casting in a set of seven in the foundry, and an initial cooling rate of 30°C/sec when poured into a room temperature mold in the VIM. The drastic difference is due to the initial temperature of the foundry mold (200-300°C) and the larger casting volume; the VIM mold produces just two bars as opposed to four in the foundry mold. Representative cooling curves for both methods are shown in Figure 7. Compositions measured through ICP-OES are given in Table 2. Alloying levels were measured as well as iron and silicon impurity levels.



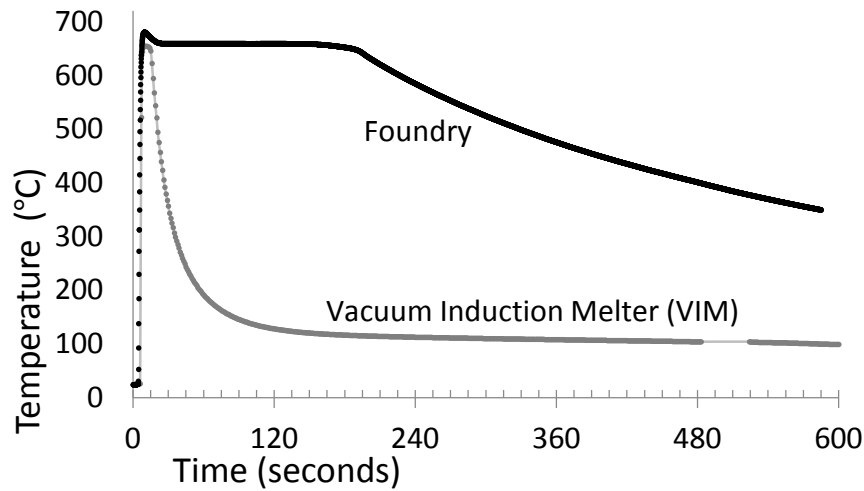


**Figure 7:** Thermocouple cooling curves for a VIM casting poured into room temperature mold and a mid-series foundry casting into a warm mold.

**Table 2:** Concentrations of alloying and impurity elements in at% as measured by ICP-OES. Boron and carbon alloying levels are listed as nominal values. Alloys are listed in order of increasing as-cast hardness (AC HV) - an indication of total solute level. \* indicates nominal value due to undissolved residual during ICP-OES dissolution process.

AC HV Rank	ID	Sc	Zr	Mg	Ti	B (nom)	C (nom)	Si	Fe
1	LP14							0.011	0.003
2	LP17		0.008					0.006	0.002
3	LP16		0.008		0.068		0.014	0.014	0.004
4	LP15		0.009		0.090	0.062		0.010	0.004
5	LP12		0.075					0.011	0.008
6	HTO5A	0.054	0.061					0.006	0.005
7	A1	0.056	0.058					n/a	0.008
8	LP09		0.081		0.069			0.009	0.009
9	LP10		0.073		0.085		0.014	0.013	0.010
10	LP11		0.075		0.075	0.062		0.012	0.008
11	A3	0.061	0.071					0.008	0.006
12	HTO8B	0.063	0.064					0.010	0.009
13	A4	0.070	0.045					0.082	0.006
14	H14A	0.120	0.027					0.003	0.003
15	B4	0.140	0.017					0.005	0.008
16	LP13		0.029		0.4*		0.080	0.023	0.018
17	H24A	0.106	0.052	1.650				0.000	0.005
18	H34A	0.110	0.066	3.883				0.003	0.005

### 3.2 As-cast Grain Structures and Porosity

As-cast grain structure for a ternary Al-Sc-Zr alloy is revealed through anodization for several compositions in Figure 1. For alloys without magnesium or titanium additions, the structure consists of columnar millimeter-scale grains with a notable centerline parallel to the parting line of the permanent mold; heat is conducted less efficiently near the parting line. Magnesium reduces grain size due to the elevated growth restriction factor at the concentrations used (discussed below), and titanium reduces grain size significantly due to a very high partition coefficient (discussed extensively in Chapter II), which is especially effective when carbides, borides, or primary aluminides are present which act as heterogeneous nucleation stimuli. A comparison of these microstructures is presented in Figure 8. Porosity observations from digital x-ray images have a resolution of about 0.5 mm, and this scale of porosity is mainly limited to gating and riser sections. Shrinkage is allowed to occur at the tops of the bars by design through the use of a bottom-fill mold design. Some defects are observed in the bar sections, especially when poured in the VIM; examples of these castings are given in Appendix II. Useable sections such bars were recovered in all cases.

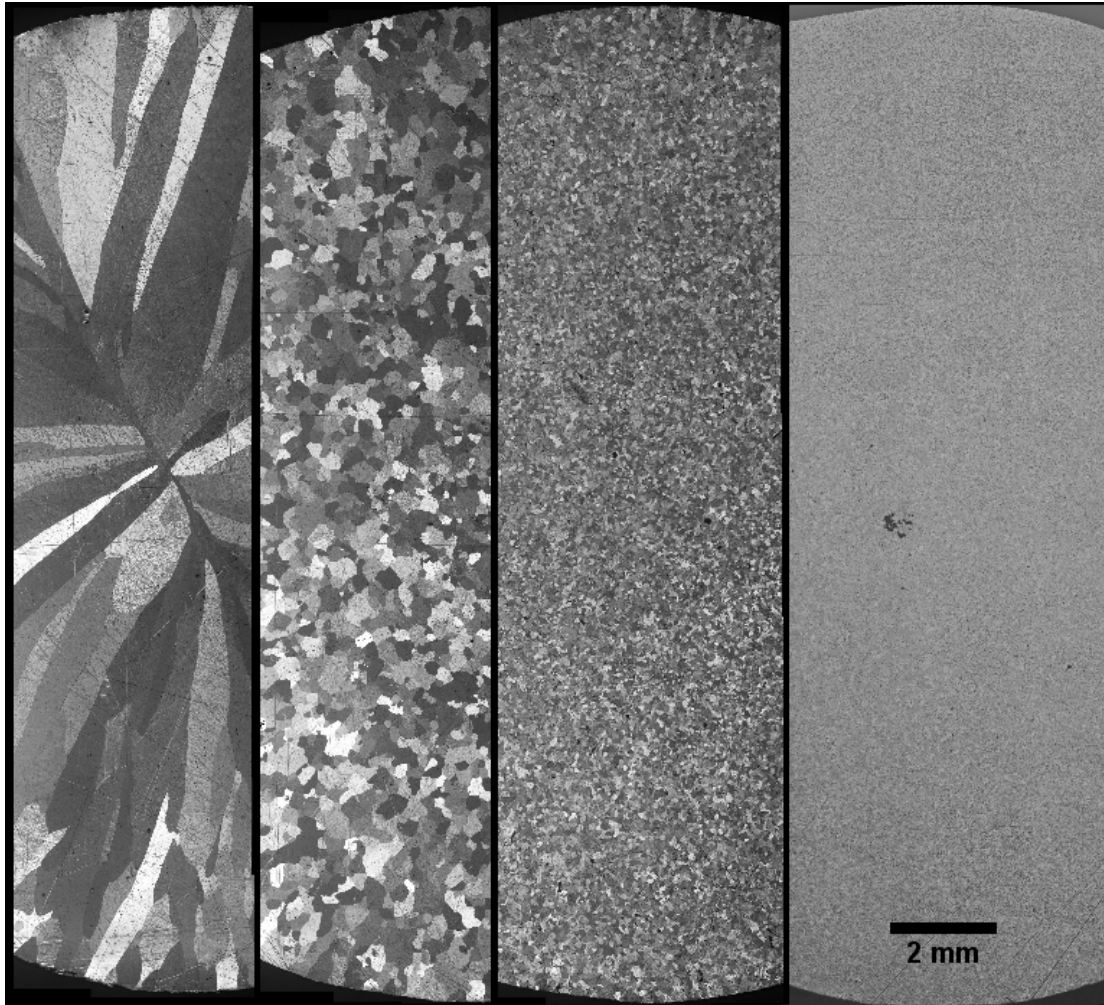


**Figure 8:** As-cast grain structures for several alloys. From left to right: Al-0.07 Sc-0.045 Zr, Al-1.65 Mg-0.106 Sc-0.052 Zr, Al-3.88 Mg-0.110 Sc-0.066 Zr, and Al-0.075 Zr-0.068 Ti-0.014 C. The first three were foundry cast (cooling rate: 1.3°C/s), and the fourth was VIM cast (cooling rate: 30°C/s).

### 3.3 Multi-step and Two-step Isothermal Aging Curves

Literature aging treatments suggest that obtaining maximum microhardness in Al-Sc-Zr alloys requires a multi-step aging treatment with three hour aging intervals at temperatures starting at 200-250°C and ending at 400-450°C [14, 43]. Multi-step aging studies were performed for various Al-Sc-Zr and Al-Mg-Sc-Zr alloys and the hardness responses are shown in Figure 9 and Figure 10, respectively, in comparison to literature

values. Conductivity tracked during these treatments are not discussed in detail; the data is given in Appendix II. In addition, the multi-step aging response is overlaid with isochronal measurements from Ref [49] in Figure 11. The latter samples were cold worked 0, 10, 25, 39, and 52% and then single step (isochronally) aged for three hours at 200, 244, 311, 340, 363, 416, or 490°C. The lower bound for the isochronal samples in Figure 11 comes from the 0% CW samples, while the upper bound represents the maximum observed for any level of cold work at a given temperature, giving an expected attainable microhardness region for this type of processing and demonstrating the optimum single step aging temperature of no more than 300°C [49].

To confirm heat treatment times sufficient to fully precipitate the  $\text{Al}_3\text{Sc}$  and  $\text{Al}_3\text{Zr}$ , single and double isothermal aging hardness studies were conducted, shown in Figure 12. Aging at 275 and 300°C yields a room temperature microhardness plateau around 500 MPa after 6 hours, which remains virtually unchanged after an additional 18 hours. Secondary aging at 375 and 400°C (following an initial 16 hours at either 275 or 300°C) provides an additional strengthening increment maximized after 6 hours and without decrease through an additional 18 hours. The same aging study was conducted following 38% cold work and produced only slightly higher peak microhardness in comparison to as-cast and aged samples, despite the initial 60 MPa difference in hardness resulting from cold-work. From these data, an aging regimen of 6 hours at 275°C + >6 hours at 400°C was determined to sufficiently remove all supersaturated solute from the matrix and produce elevated yield strength.

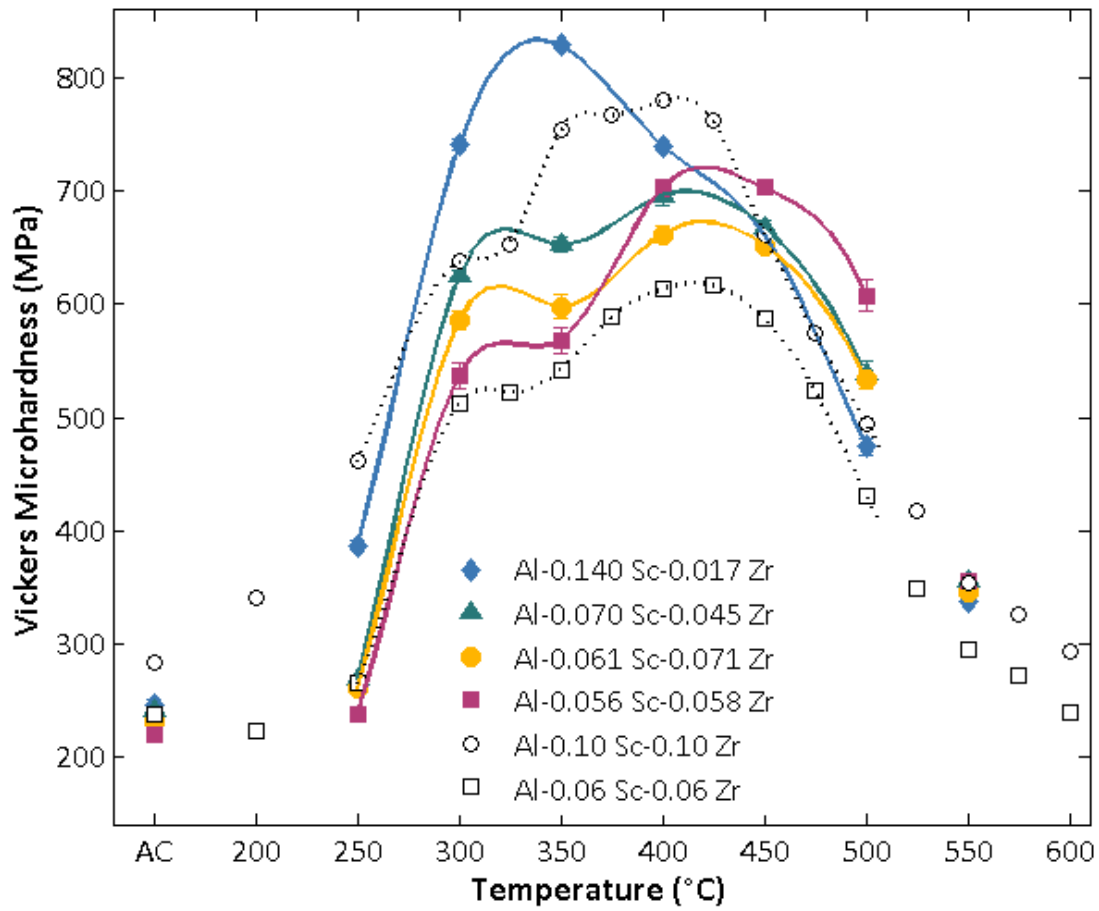


**Figure 9:** Microhardness response for multi-step aging of as-cast Al-Sc-Zr alloys, where the dashed lines are reference curves adopted from the work of Knipling et al. [14, 43].

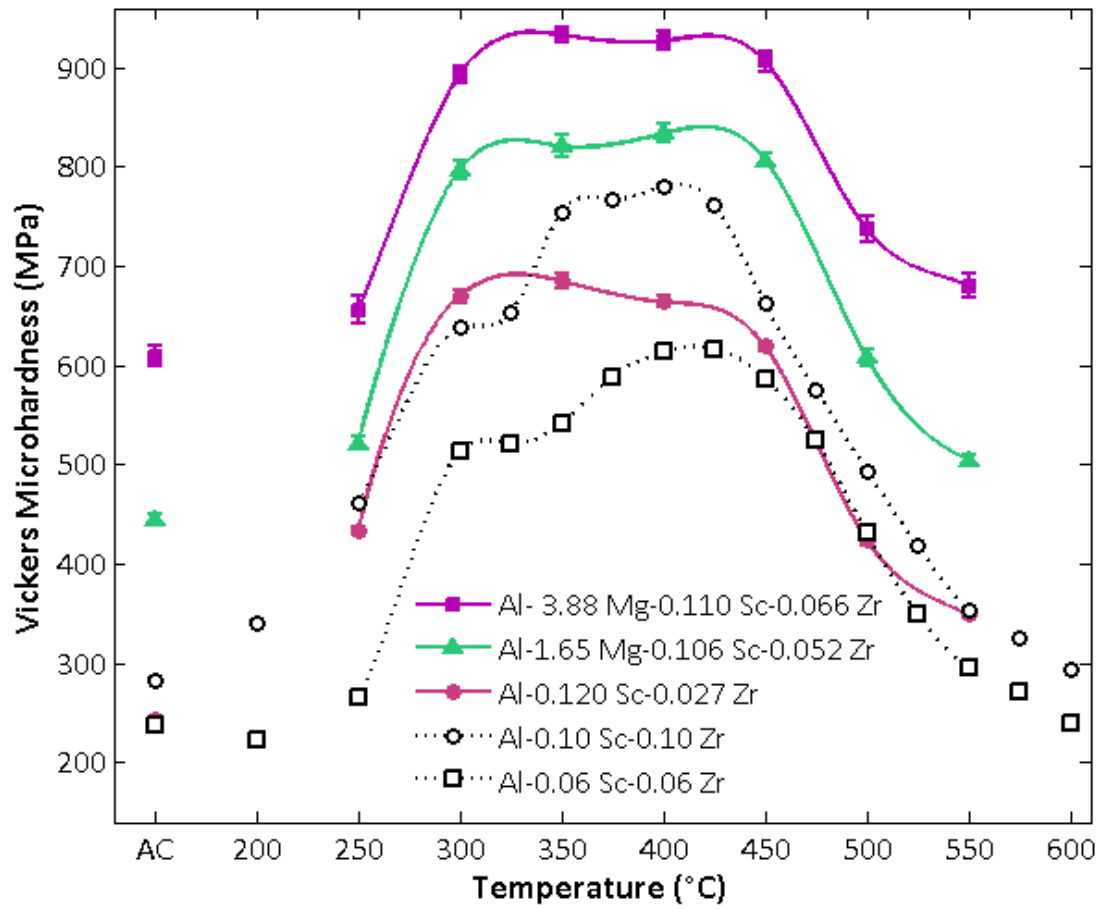


**Figure 10:** Microhardness response for multi-step aging of as-cast Al-Mg-Sc-Zr alloys, where the dashed lines are reference curves adopted from the work of Knipling et al.[14, 43].

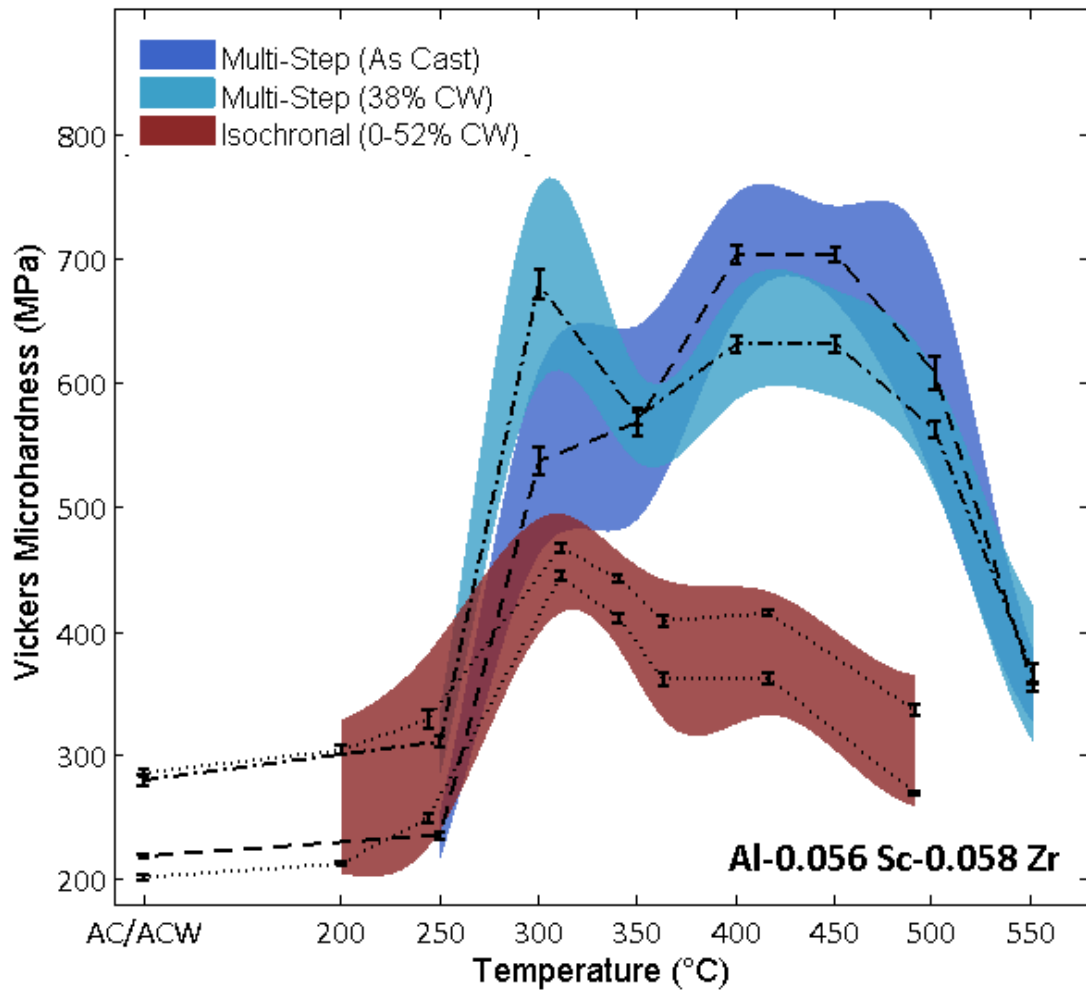


**Figure 11:** Multi-step aging treatments for as-cast and 38% cold worked Al-0.056 Sc-0.058 Zr in comparison to isochronally aged Al-0.056 Sc-0.058 Zr. For the latter series, the lower bound is from as-cast and aged samples, while the upper line represents the highest hardness obtained after cold work and a single three hour aging treatment at a given temperature (adopted from McNamara et al. [49]). Shaded regions are 95% confidence intervals.

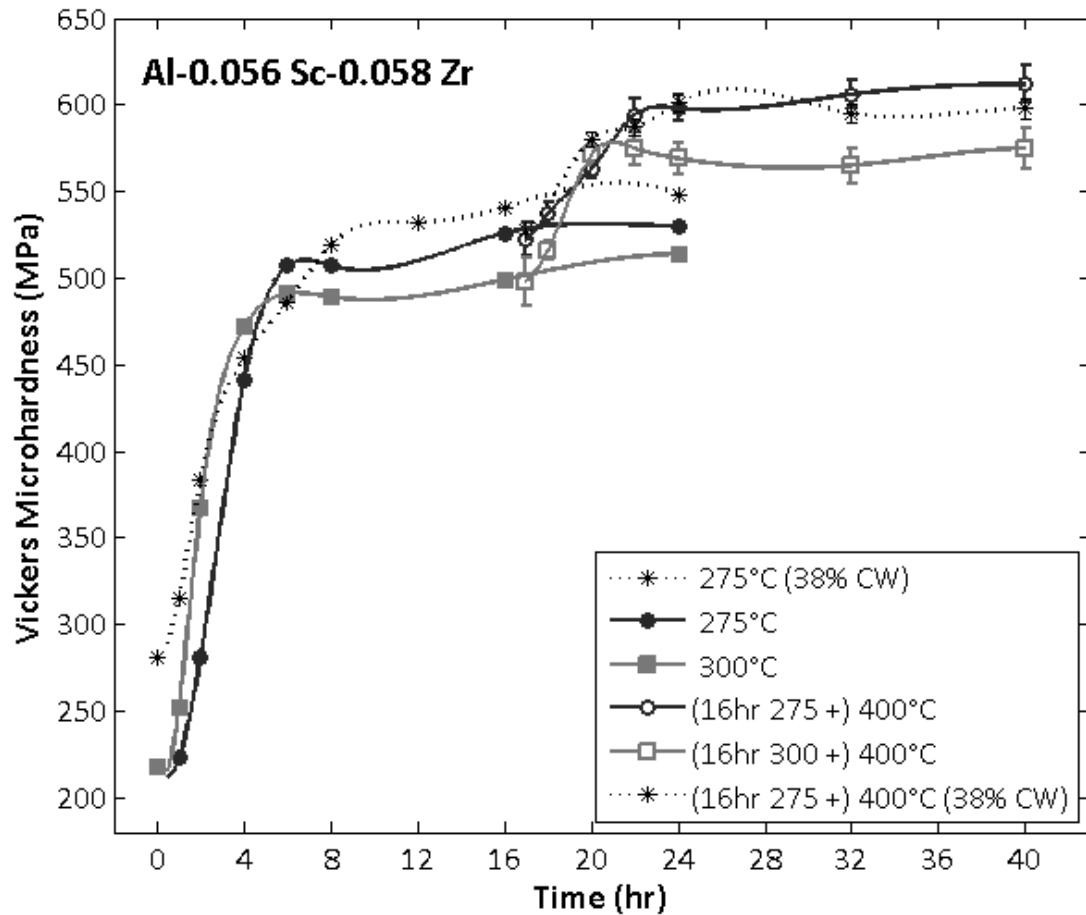


**Figure 12:** Microhardness response during single and double isothermal aging for an Al-0.056 Sc-0.058 at% Zr alloy starting from the as-cast or 38% CW condition.

### 3.4 Comparison of Peak Microhardness for Al-Sc-Zr and Al-Zr Alloys

The Al-Zr alloys were also multi-step aged from 250 to 400°C in three hour increments at 50° spacing. The observed hardness for these alloys following the 400°C step is compared to that of Al-Sc-Zr and Al-Mg-Sc-Zr alloys in Figure 13, where the alloys are ranked along the x-axis according to as-cast hardness, given as a dashed line. Extremely mild hardening responses are observed for the Al-Zr based alloys, and in contrast to the Al-Sc-Zr alloys, double aging produced stronger microstructures than multi-step aging of alloys with 0.07 at% Zr. The increase in hardness following aging and 75% cold work is given for the Al-Zr alloys to demonstrate potential for wrought products.



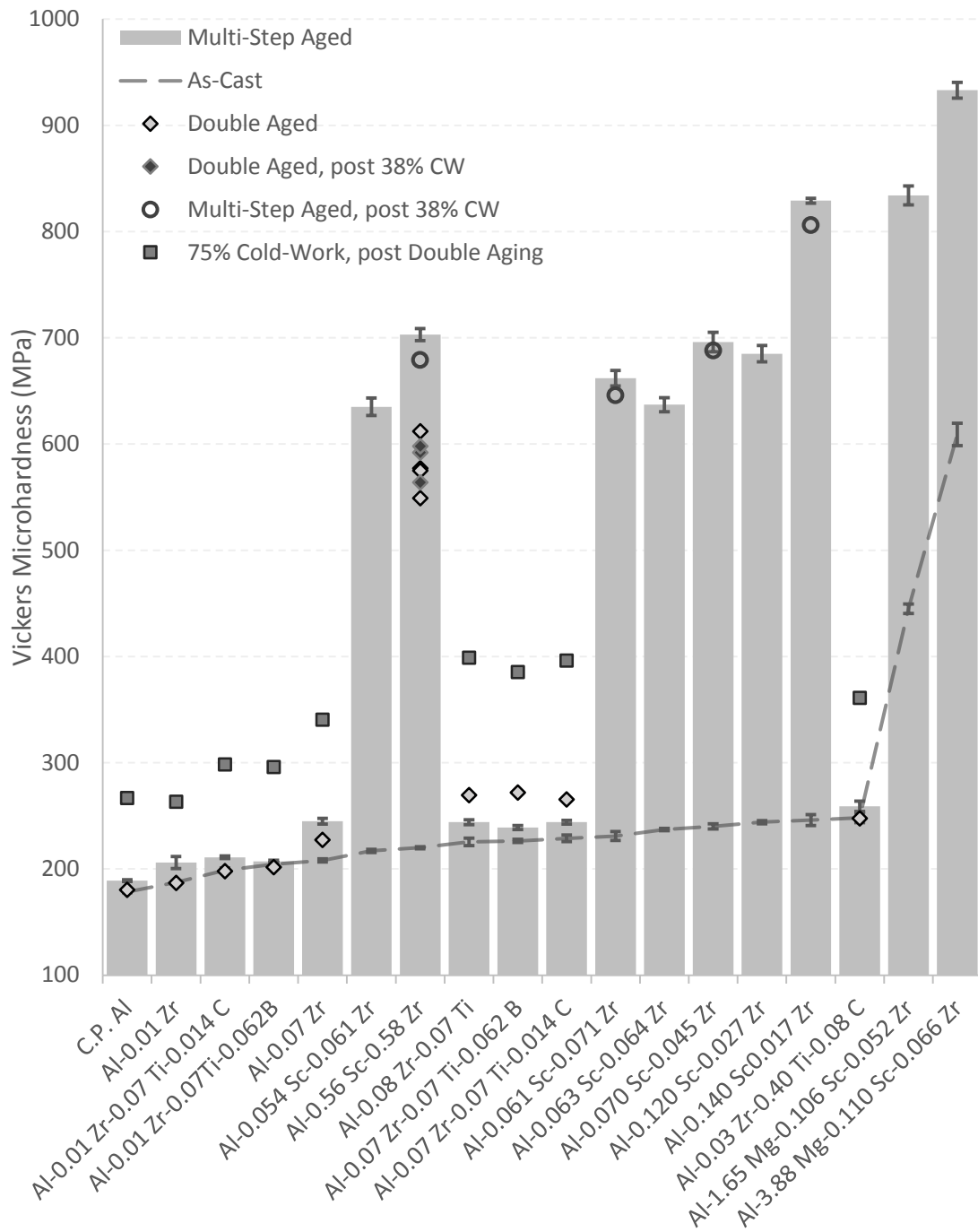


**Figure 13:** Comparison of microhardness response for various Al-Sc-Zr and Al-Zr alloys following multi-step aging, double-aging, and cold work (before and after aging, for some alloys). Compositions are listed in at%.

### 3.5 Tensile Stress-Strain Curves for Al-Sc-Zr and Al-Mg-Sc-Zr

Tensile bars were aged based on diffusivity considerations and microhardness responses to produce the maximum volume fraction of trialuminides. Furthermore, overaged distributions were desired for ease of observation in post-mortem TEM, SEM, and subsequent strengthening mechanism analyses. An aging regimen of 16 hr at 275°C followed by 16 hr at 400°C was chosen for the tensile bars in this study based on the simplicity of the approach, even though higher absolute microhardness values were observed for multi-step aged samples. Tensile engineering stress-strain curves are given in Figure 14. Al-Sc-Zr bars which were subjected to a one hour solutionization treatment prior to double-aging yielded at  $122 \pm 3$  MPa (0.02 offset), and exhibited 4% strain to the onset of necking, and 9% at fracture. The same composition aged from the cold worked condition yielded at  $151 \pm 2$  MPa and exhibited about 12% strain to the onset of necking, and 15% at fracture, compared to  $148 \pm 2$  MPa yield strength with 16% strain to necking and 17% at failure for a very similar alloy aged from the as-cast condition. Upon addition of magnesium, yield strength increased to  $178 \pm 2$  MPa and  $193 \pm 2$  MPa for a 1.72 at% and 3.88 at% addition, respectively, while elongation decreased significantly. A full list of values for yield stress, ultimate tensile strength (UTS), % uniform elongation, and total elongation are presented in Table 3.

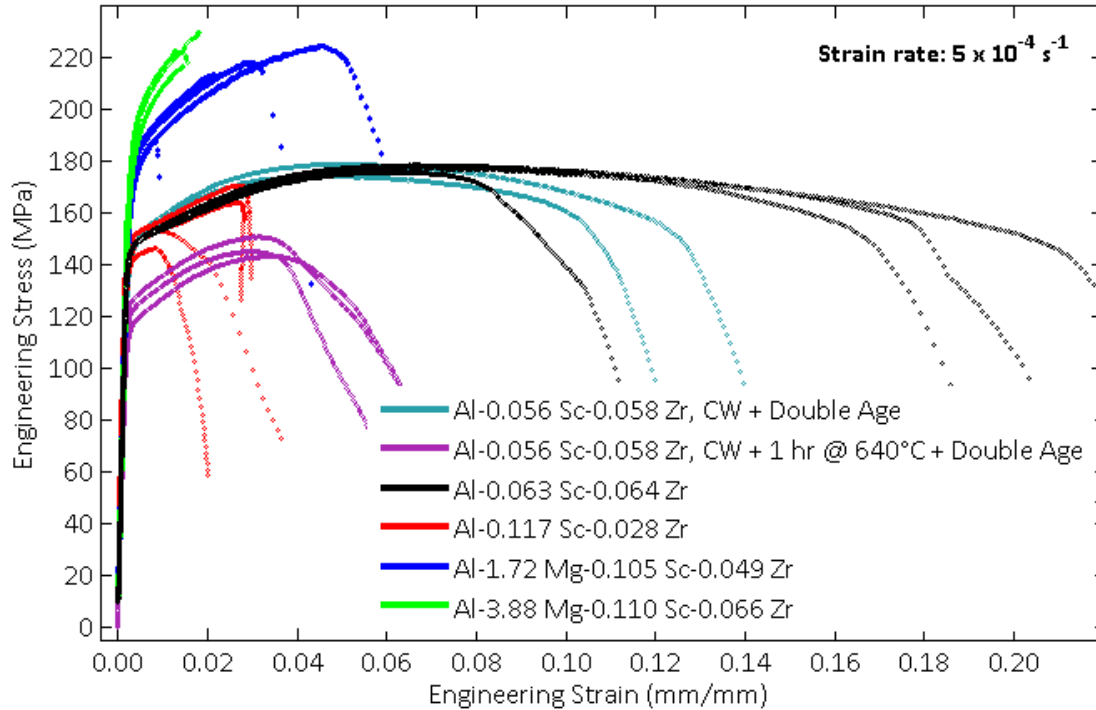


**Figure 14:** Engineering stress-strain curves for several alloys. The magnesium alloy curves end abruptly as they often failed outside the extensometer, and the Al-0.117 Sc-0.028 at% Zr alloy was observed to fail at inclusions and thus had very poor elongation compared to the other ternary samples.

**Table 3:** Uniaxial tensile properties for alloys represented in Figure 14 with standard error. Notes: Total elongation was measured using calipers for the bottom four alloys here; many ultimately failed outside of the 25.4 mm extensometer; the Al-117 Sc-0.028 was also observed to fail at inclusions, resulting in poor elongation performance.

Alloy (at%)	Condition	$\sigma_{YS,0.02}$ (MPa)	UTS (MPa)	Uniform %El	Total %El
Al-0.056 Sc-0.058 Zr	CW + Double Aged	151 ± 2	177 ± 2	11.5 ± 1.2	15.1 ± 0.1
Al-0.056 Sc-0.058 Zr	CW + Sol'n + Double Aged	122 ± 3	147 ± 2	3.4 ± 0.1	8.9 ± 0.6
Al-0.063 Sc-0.064 Zr	Double Aged	148 ± 0.1	178 ± 0.6	16.1 ± 2.8	17 ± 1.2
Al-0.117 Sc-0.028 Zr	Double Aged	148 ± 2	159 ± 5	1.9 ± 0.4	5.1 ± 0.6
Al-1.72 Mg-0.105 Sc-0.049 Zr	Double Aged	178 ± 2	211 ± 8	2.5 ± 0.7	5.9 ± 1.1
Al-3.88 Mg-0.110 Sc-0.066 Zr	Double Aged	193 ± 2	223 ± 4	1.6 ± 0.1	3.3 ± 0.5

### 3.6 Post-mortem TEM Imaging of Nanoscale Precipitates and SEM Fractography

Thin slices from grip sections in the Al-0.056 Sc-0.058 Zr cold worked and aged bar were imaged in brightfield TEM for precipitate size analysis. Examples of the captured images are presented in Figure 15. For this composition and condition, a total of 55 trialuminide precipitates were measured giving an average dispersoid radius of  $4.4 \pm 0.86$  nm (st dev). A secondary electron image of the fracture surface from the same bar is presented in Figure 16, illustrating the gross intergranular fracture during uniaxial tensile testing.

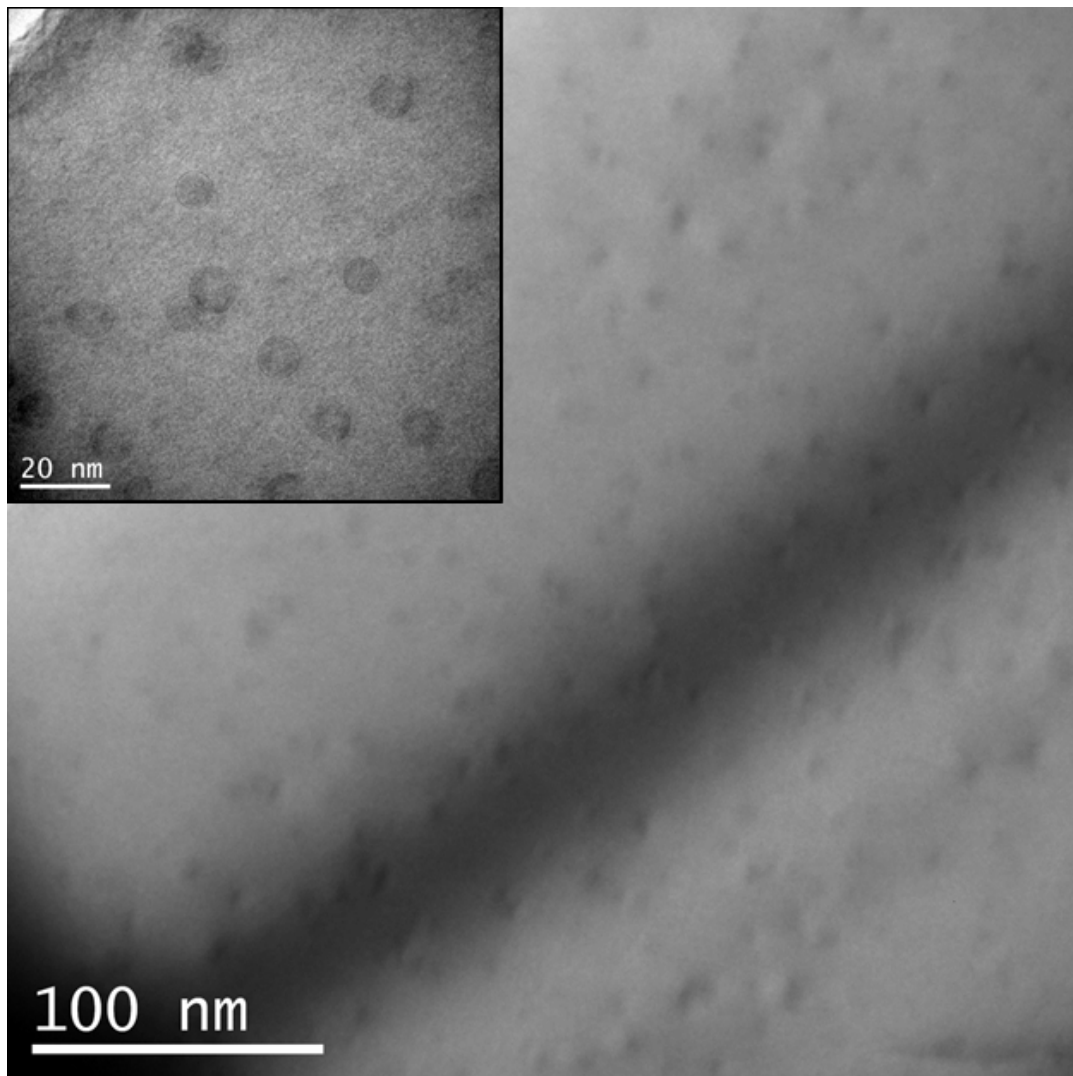


**Figure 15:** A fine dispersion of precipitates formed during double-aging of Al - 0.056 Sc - 0.058 Zr as viewed in brightfield TEM. (Inset) Five fields of view at roughly 7x higher magnification containing a total of 55 precipitates were used for dispersoid size measurement.

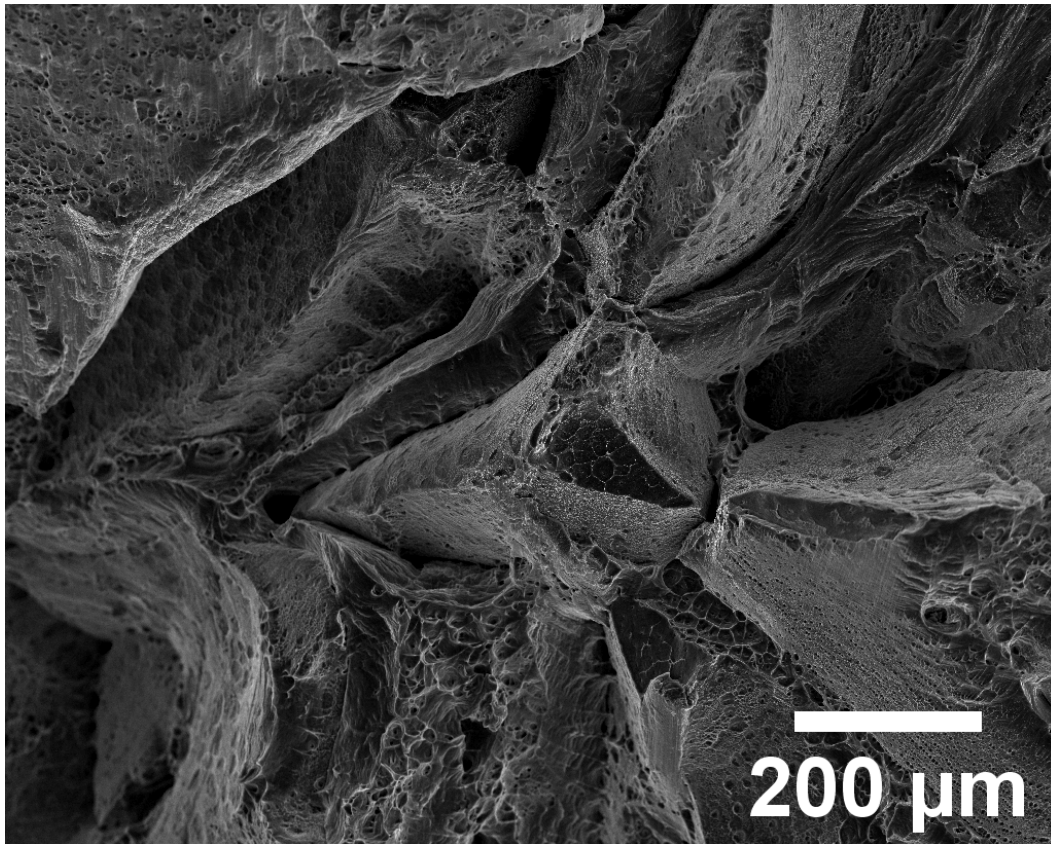


**Figure 16:** SEM secondary electron image near center of a fractured tensile bar in the cold worked and double aged condition. Void nucleation and coalescence is apparent on grain boundaries indicating intergranular fracture.

## 4. Discussion

### 4.1 Quality of Castings

As-cast microstructures for dilute Al-Sc-Zr alloys exhibit large columnar grains which nucleate on the mold walls and propagate towards the center of the solidifying bars. In the foundry castings, there is a centerline in the grain structure which is parallel to the partition line of the mold, as heat is withdrawn from the melt most efficiently perpendicular to the partition line. Large grained, columnar castings are undesirable in practical applications since mechanical properties become much more anisotropic. Specifically, cracks which form

during fatigue can propagate large distances along these boundaries, and void coalescence leading to failure becomes more prevalent during tensile loading. The remnants of this latter effect are directly observed in Figure 16. Grain refinement through alloying or increased cooling rate is necessary in order to produce a more uniform microstructure while retaining both Sc and Zr in solid solution for strengthening purposes. Rapid cooling is often impossible when producing large castings in industry, and the use of grain refining additions is preferred in these cases.

#### 4.1.1 Grain Refinement

When magnesium is added to the foundry melt, grain size decreases and grain aspect ratios approach unity, as shown in Figure 8. While the Al-Mg is a eutectic system and therefore hypoeutectic compositions do not form any primary precipitates to act as grain nuclei, there is still a constitutional supercooling effect which is described by the growth restriction factor,  $Q$ , given by Equation 11 [50]:

$$Q = mc_0(k - 1) \quad \text{Equation 11}$$

where  $m$  is the slope of the binary liquidus, assumed linear,  $c_0$  is the concentration of the element of interest, and  $k = c_s/c_l$  at the interface temperature is the partition coefficient. Values of  $m$  and  $k$  are given for Zr, Ti, and Mg in Table 4, taken directly from [50], where  $m$  reflects concentrations in wt%. The value of  $Q$  is an indicator for the level of thermodynamic influence of solute on growth velocity of dendritic tips or radial growth in spherically modelled grains. In general, solute decreases the solid/liquid interface velocity during solidification which allows time for the formation of new stable nuclei ahead of the interface and can enrich the liquid ahead of the interface producing constitutional undercooling. For magnesium, at levels of 1.65 and 3.88 at%, growth restriction factors are 4.5 and 10.6, respectively. However, the currently accepted models for grain refinement [51] still require the presence of nucleant particles in the melt on which these new grains form. In the present study, no primary particles were detected in the 1.65 and 3.88 at% Mg alloys and Fe and Si impurity levels were measured at very low concentrations, although the nucleant particles could be un-resolvable in the JSM-6400 tungsten filament SEM. Further investigation is warranted using a higher resolution instrument.

**Table 4:** Growth restriction factors ( $Q$ ) for the concentrations of alloying elements in alloys where grain refinement was observed. Values of  $m$  and  $k$  are from Ref [50].

Element	$k$	$m$	$(k-1)m$	$c_0$ (at%)	$c_0$ (wt%)	$Q$ (K)
Ti	9	30.7	245.6	0.07	0.12	30.5
				0.09	0.16	39.1
				0.40	0.71	173.6
Zr	2.5	4.5	6.8	0.01	0.03	0.2
				0.06	0.20	1.4
				0.08	0.27	1.8
Mg	0.51	-6.2	3.0	1.65	1.49	4.5
				3.88	3.50	10.6

The grain sizes in the Al-Zr-Ti alloys cannot be directly compared to the Sc- and Sc-Mg- compositions, as the former were cooled at a much faster rate using the VIM casting process. Cooling rate has a large effect on the resultant grain size, and these compositions are therefore only internally comparable. In doing so, the addition of titanium promotes equiaxed grain formation and a drastic reduction of as-cast grain size compared to the pure aluminum and Al-0.01 at% Zr alloy cast using the VIM due to the large values of  $k$  and  $m$  for the Al-Ti system relative to those for Al-Zr. The differences in these systems are discussed in more detail in Chapter II of this contribution.

#### 4.2 Hardness Increases from Mg, Ti, Ti-B, and Ti-C Additions

Though grain size decreases with Mg, Ti, Ti-B, and Ti-C additions, Hall-Petch strengthening is not anticipated to play a role in the increases in as-cast and aged hardness values obtained for these alloy, since the test itself is designed to measure intragranular hardness. For the most highly refined alloy (Al-0.30 Zr-0.40 Ti-0.08 at% C), the indentation size is roughly the same as the grain size. Solute strengthening is expected to play a significant role, however, especially in the case of Mg alloys and the highest Ti level alloy. From the as-cast hardness measurements relative to pure aluminum cast in the VIM (178 MPa Vickers,  $H_V$ ), Table 5 lists the hardness increases attributed to solution strengthening.

**Table 5:** Solute strengthening as observed by increase in as-cast microhardness relative to pure aluminum cast in the VIM. As-cast hardness is given with  $\pm$  standard error, compositions are in at%.

ID	H <sub>v</sub> , As-cast (MPa)	$\Delta$ H <sub>v</sub> Solution (MPa)
99.99% Al	178 $\pm$ 0.7	-
Al-0.01 Zr	187 $\pm$ 1.1	9
Al-0.01 Zr-0.07 Ti-0.062 C	199 $\pm$ 2.1	21
Al-0.01 Zr-0.07 Ti-0.014 B	204 $\pm$ 1.4	26
Al-0.07 Zr	208 $\pm$ 1.5	30
Al-0.054 Sc-0.061 Zr	217 $\pm$ 1.5	39
Al-0.056 Sc-0.058 Zr	220 $\pm$ 1.0	42
Al-0.08 Zr-0.07 Ti	225 $\pm$ 3.6	47
Al-0.07 Zr-0.07 Ti-0.062 B	226 $\pm$ 1.5	48
Al-0.07 Zr-0.07 Ti-0.014 C	229 $\pm$ 3.2	51
Al-0.061 Sc-0.071 Zr	231 $\pm$ 4.1	53
Al-0.063 Sc-0.064 Zr	237 $\pm$ 1.1	59
Al-0.070 Sc-0.045 Zr	240 $\pm$ 2.4	62
Al-0.120 Sc-0.027 Zr	244 $\pm$ 1.4	66
Al-0.140 Sc-0.017 Zr	246 $\pm$ 5.2	68
Al-0.03 Zr-0.40 Ti-0.08 C	248 $\pm$ 4.5	70
Al-1.72 Mg-0.106 Sc-0.052 Zr	445 $\pm$ 4.5	267
Al-3.88 Mg-0.110 Sc-0.066 Zr	609 $\pm$ 10.5	431

Solute strengthening was also apparent in tensile tested Al-Mg-Sc-Zr bars when compared to bars with similar Sc and Zr content, cast and aged in the same manner. With the addition of 1.72 at% Mg, the measured increases in yield strength and UTS were 30 and 52 MPa, respectively. For an addition of 3.88 at% Mg, yield strength and UTS increased by 45 and 64 MPa, respectively. Part of these strength increases are also due to the reduction in grain size, where grain boundaries also serve as effective obstacles for dislocation motion. According to the Hall-Petch relation (last term of Equation 2) based on measured grain sizes of  $228 \pm 5 \mu\text{m}$  and  $57 \pm 3 \mu\text{m}$  for 1.72 and 3.88 at% Mg, the yield strength increments are 4.64 and 9.27 MPa, respectively.



### 4.3 Increase of Hardness and Yield Strength through Precipitation

The changes in microhardness following multi-step heat treatment for the alloys shown in Figures 9 and 10 are given below in Table 6, where A1 represents the hardness after the 350°C aging step, and A2 is the hardness after the 400°C aging step, corresponding to the sequential precipitation of Al<sub>3</sub>Sc and Al<sub>3</sub>Zr.  $\Delta\sigma$ , A1 corresponds to the difference in hardness relative to the as-cast state, while  $\Delta\sigma$ , A2 corresponds to the difference relative to A1. These hardness increments are also plotted against Sc:Zr ratio in Figure 17. A decrease in hardness at the higher temperature aging step is observed for the alloys which contain relatively high levels of Sc and low levels of Zr, rows 5 and 6 in Table 6. This is likely due to the ripening of Al<sub>3</sub>Sc precipitates at 400°C without the protective shell of Al<sub>3</sub>Zr, as the concentration of Zr is too low to stabilize all of the particles sufficiently. Also, it is noted that when Mg is added, the increase in hardness due to aging is not as high as would be expected given the level of Sc present in the Mg-added alloys, suggesting some minor interference of Mg on precipitation of Al<sub>3</sub>Sc.

A comparison of theoretical and experimental yield strength and microhardness values is given in Table 7. Theoretical yield strengths were obtained using Equations 2-10, Table 8 lists values for the constants used in these equations, and conversion to theoretical microhardness is given using the approximation  $H_V = 3\sigma_Y$  [40]. The particle strengthening contributions constitute most of the predicted hardness and these equations are highly sensitive to particle radius and, consequently, interparticle spacing. Only one TEM measurement was made (discussed in Section 4.3.2) to determine average particle radius on the Al-0.056 Sc-0.058 Zr alloy following 38% CW and Double-Isothermal (Double-IT) aging. The multi-step aged samples are expected to have a slightly finer distribution of precipitates and the particle strengthening estimations for these samples are based on an average particle radius of 4 nm. The double aged samples are expected to have the same or slightly larger average radius than the sample measured, and a particle radius of 5 nm is used for these approximations. In all cases, the estimated particle radii result in Orowan looping being the preferred mechanism for dislocation motion around these particles and thus  $\Delta\sigma_p$  does not reflect the predictions for coherency or modulus strengthening associated with

dislocation shear of particles. For solute strengthening, a value of  $\xi = 4$  was chosen based on the as-cast hardness increases shown in Table 7.

**Table 6:** Observed increase in Vickers microhardness during multi-step aging, where A1 is after the 350°C step and A2 after the 400°C step. Hardness is given with  $\pm$  standard error; compositions are in at%.

ID	H <sub>v</sub> , As-Cast (MPa)	H <sub>v</sub> , A1 (MPa)	$\Delta$ H <sub>v</sub> , A1	H <sub>v</sub> , A2 (MPa)	$\Delta$ H <sub>v</sub> , A2
99.99 Al	178 $\pm$ 0.7	180 $\pm$ 4.6	<b>2</b>	180 $\pm$ 4.6	<b>0</b>
Al-0.056 Sc-0.058 Zr	220 $\pm$ 1.0	568 $\pm$ 11.4	<b>348</b>	703 $\pm$ 7.3	<b>135</b>
Al-0.061 Sc-0.071 Zr	231 $\pm$ 4.1	598 $\pm$ 10.9	<b>367</b>	662 $\pm$ 7.3	<b>64</b>
Al-0.070 Sc-0.045 Zr	240 $\pm$ 2.4	653 $\pm$ 7.0	<b>413</b>	696 $\pm$ 9.1	<b>43</b>
Al-0.120 Sc-0.027 Zr	244 $\pm$ 1.4	685 $\pm$ 7.7	<b>441</b>	664 $\pm$ 5.9	<b>-21</b>
Al-0.140 Sc-0.017 Zr	246 $\pm$ 5.2	829 $\pm$ 2.3	<b>583</b>	740 $\pm$ 4.3	<b>-89</b>
Al-1.65 Mg-0.106 Sc-0.052 Zr	445 $\pm$ 4.5	821 $\pm$ 10.6	<b>376</b>	834 $\pm$ 9.0	<b>13</b>
Al-3.88 Mg-0.110 Sc-0.066 Zr	609 $\pm$ 10.5	933 $\pm$ 7.4	<b>324</b>	927 $\pm$ 9.6	<b>-6</b>

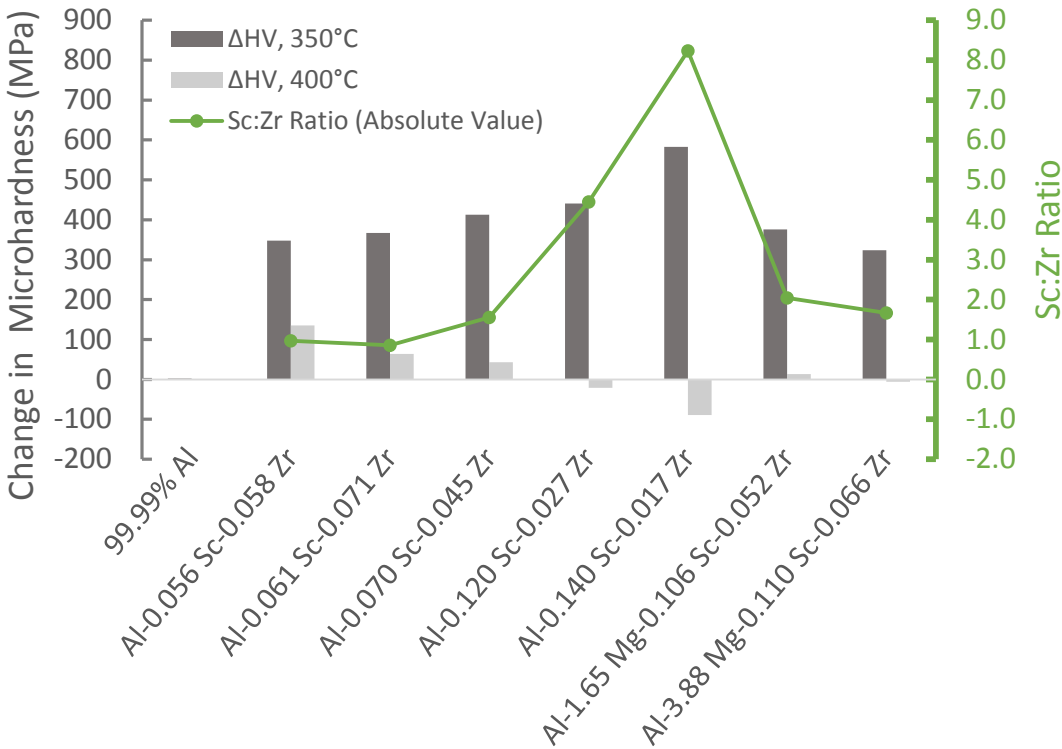


**Figure 17:** Changes in microhardness following the 350 and 400°C aging steps in comparison with Sc:Zr atomic ratios.

**Table 7:** Theoretical and experimental strengthening values obtained for several Al-Sc-Zr and Al-Mg-Sc-Zr alloys.

Composition (at %)	Aging	$\Delta\sigma_P$	$\Delta\sigma_S$	$\Delta\sigma_{GS}$	$\Delta\sigma_D$	$\sigma_Y$ (Th.)	$\sigma_Y$ (Exper.)	Hv (Th.)	Hv (Exper.)
		MPa	MPa	MPa	MPa	MPa	MPa	MPa	MPa
Al-0.056 Sc-0.058 Zr	Multi	269	-	-	-	<b>285</b>	-	<b>855</b>	<b>703</b>
Al-0.063 Sc-0.064 Zr	Multi	290	-	-	-	<b>290</b>	-	<b>869</b>	<b>637</b>
Al-0.061 Sc-0.071 Zr	Multi	305	-	-	-	<b>305</b>	-	<b>916</b>	<b>662</b>
Al-0.070 Sc-0.045 Zr	Multi	253	-	-	-	<b>253</b>	-	<b>759</b>	<b>696</b>
Al-0.120 Sc-0.027 Zr	Multi	269	-	-	-	<b>269</b>	-	<b>808</b>	<b>685</b>
Al-0.140 Sc-0.017 Zr	Multi	272	-	-	-	<b>272</b>	-	<b>815</b>	<b>829</b>
Al-1.65 Mg-0.106 Sc-0.052 Zr	Multi	302	62	5	-	<b>369</b>	-	<b>1107</b>	<b>834</b>
Al-3.88 Mg-0.110 Sc-0.066 Zr	Multi	337	146	9	-	<b>492</b>	-	<b>1476</b>	<b>933</b>
Al-0.056 Sc-0.058 Zr	CW + Double-IT	252	-	-	36	<b>293</b>	<b>151</b>	<b>880</b>	<b>595</b>
Al-0.063 Sc-0.064 Zr	Double-IT	249	-	-	-	<b>249</b>	<b>148</b>	<b>746</b>	<b>606</b>
Al-0.120 Sc-0.027 Zr	Double-IT	231	-	-	-	<b>231</b>	<b>148</b>	<b>693</b>	-
Al-1.65 Mg-0.106 Sc-0.052 Zr	Double-IT	259	62	5	-	<b>326</b>	<b>178</b>	<b>978</b>	-
Al-3.88 Mg-0.110 Sc-0.066 Zr	Double-IT	289	146	9	-	<b>444</b>	<b>193</b>	<b>1332</b>	-

**Table 8:** Constants used in strengthening equations to predict theoretical yield strength and hardness.

$X$ [32]	$\rho$ [32]	$\xi$	$\nu$ [38]	$\alpha$ [41]	$k_y$ [38] (MN/m <sup>3/2</sup> )	$\beta$ [38]	
<b>2.6</b>	<b>0.85</b>	<b>4</b>	<b>0.35</b>	<b>0.5</b>	<b>0.07</b>	<b>1</b>	
$\sigma_0$ (MPa)	$b$ [52] (m)	$\gamma_{APB}$ [43] (J/m <sup>2</sup> )	$M$ [38]	$G_{Al}$ [52] (Pa)	$G_{Al3Sc}$ [53] (Pa)	$G_{Al3Zr}$ [54] (Pa)	$G_{Al3Ti}$ [55] (Pa)
<b>16</b>	<b>2.86E-10</b>	<b>0.5</b>	<b>3.06</b>	<b>2.5E+10</b>	<b>6.8E+10</b>	<b>9.5E+10</b>	<b>7.1E+10</b>
$\epsilon_{Al3Sc}$	$\epsilon_{Al3Zr}$	$\epsilon_{Al3Ti}$	$\delta_{Mg}$	$\delta_{Sc}$	$\delta_{Zr}$	$\delta_{Ti}$	
<b>0.0222</b>	<b>0.0164</b>	<b>0.0234</b>	<b>0.1189</b>	<b>0.1329</b>	<b>0.1189</b>	<b>0.028</b>	

To illustrate the trends observed in Table 7, the theoretical and observed values of hardness for multi-step aged Al-Sc-Zr and Al-Mg-Sc-Zr alloys are plotted in Figure 18. The first conclusion that can be made is that Mg-containing alloys exhibit significantly less hardness than would be anticipated from the solute and precipitation strengthening contributions. For example, the 1.65 at% Mg alloy produced the same hardness as the highest Sc-containing alloy, while both had approximately the same overall Sc+Zr concentration; the predicted hardness for the former alloy is 292 MPa higher than the latter.

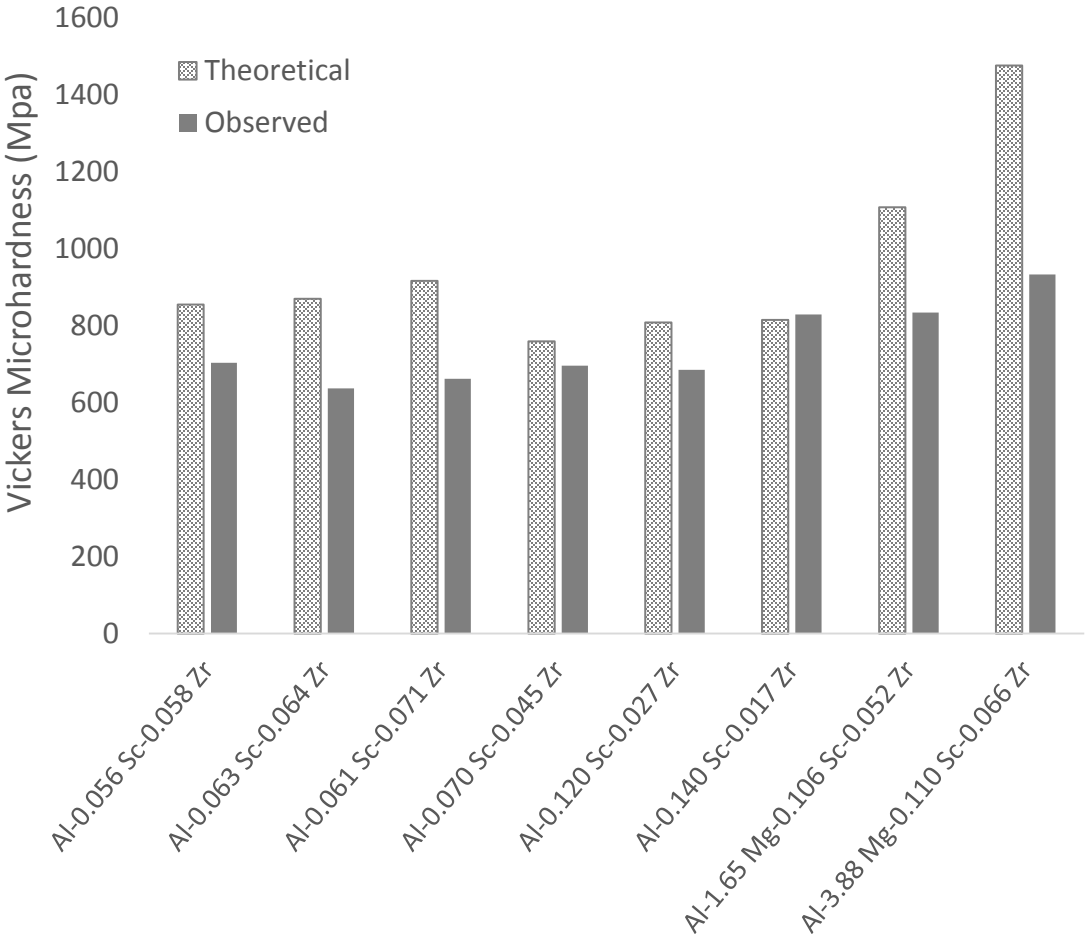


**Figure 18:** Comparison of theoretical and maximum observed microhardness for the alloys of Figures 9 and 10.

#### 4.3.1 Effect of Mg, Ti, Ti-B, and Ti-C on Precipitation Hardening

Mg in solution does not have an effect on the ability of Sc and Zr to precipitate and strengthen the material as evidenced by the multi-step aging curves in Figure 10, but it does have an effect on the magnitude of observed strengthening evidenced by Figure 17. The characteristic first bump in microhardness around 300°C is followed by a second bump at 400-450°C corresponding to the nucleation and growth events of  $\text{Al}_3\text{Sc}$  and  $\text{Al}_3\text{Zr}$ , respectively, but the observed values are about 15% less than alloys with comparable levels of Sc and Zr and 0% Mg. The overall observed strengthening for these alloys also falls well below predicted values which is not fully accounted for by the difference in precipitation hardening. Therefore, the solution hardening effect is also not utilized fully in the aged samples. Current phase diagrams for Al-Mg-Sc (350°C), Al-Mg-Zr (400°C), Mg-Sc, and Mg-Zr, as accessed through the online ASM Phase Diagram Database, do not indicate the formation of any binary or ternary intermetallic compounds for concentrations less than 10-12% Mg, and the dilute Sc and Zr concentrations used here. Therefore, Mg segregation and clustering is likely responsible for the decreased post-aging solute strengthening.

In the alloys without Sc nor Mg, at both Zr levels in the grain refined alloys, precipitation strengthening was less effective when Al-Ti-B is added compared to Al-Ti-C, though it is noted that none of the four alloys hardened significantly in the absence of Sc, shown in Figure 13.

#### 4.3.2 Effect of Cold Work on Aging of Al-Sc-Zr Alloys

While there is an initial advantage to cold work prior to aging in terms of hardness, once precipitation temperatures for  $\text{Al}_3\text{Zr}$  are reached, extensive recovery occurs and the strengthening due to excess dislocations diminishes. For the multi-step and double-isothermally aged samples, prior cold work appears to be detrimental to the age-hardening process. This can be explained in terms of increased heterogeneity in the number density and particle sizes of the precipitate distribution. Precipitates form more readily in regions of elevated dislocation density due to higher thermodynamic driving force for growth in highly misoriented regions. Increased nucleation occurs on dislocation lines in these regions, and while the local interparticle spacing would be locally smaller, interparticle spacing increases

in regions of relatively low dislocation density leading to decreased overall strengthening. In addition to a weaker distribution, the particles also grow faster which leads to earlier overaging. A thorough TEM-based study would be the ideal way to analyze these effects in detail.

Higher magnification images of the region in Figure 15 were used to measure an average precipitate radius of  $4.4 \pm 0.86$  nm from 55 precipitates; the distribution of precipitate sizes is given in Figure 19. The estimated average edge-to-edge interprecipitate spacing,  $\lambda$ , is approximately 55 nm, through Equation 8 [32, 39] for a monodispersed array of particles in the alloy examined here (i.e.  $f = 1.06\%$  from lever rule estimation,  $R = 4.4$  nm). Orowan strengthening is expected to be dominant for the 4.4 nm average precipitate size with a strengthening increment of about 210 MPa. The measured yield strength of 151 MPa does not agree well with the linear addition of the nominal yield strength of 99.8 wt% aluminum (16 MPa [56]) and the predicted Orowan strengthening increment. As previously mentioned, the yield strength measured in tension also conflicts with microhardness measurements which suggest much higher hardening potential for this alloy.

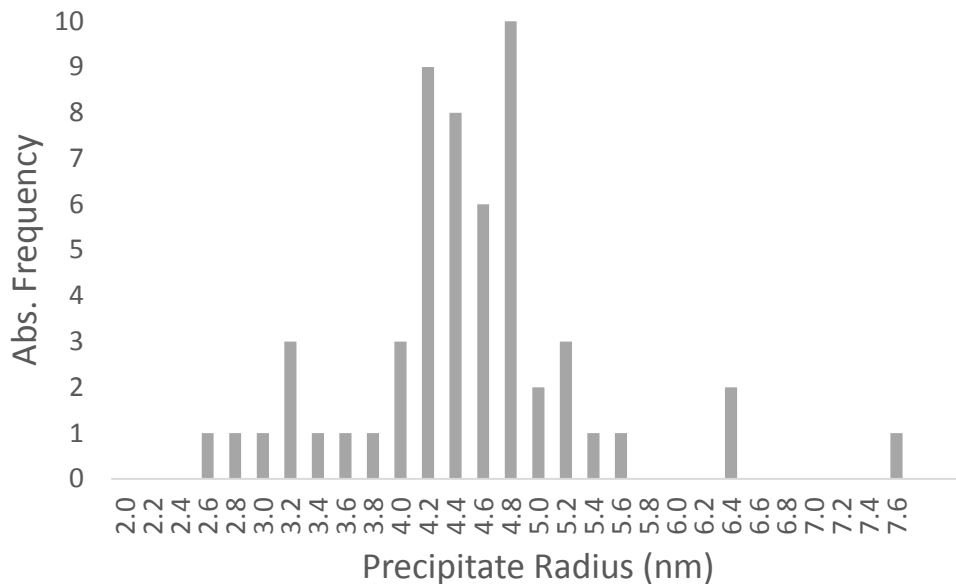


**Figure 19:** Precipitate size distribution measured from brightfield TEM images of Al-0.056 Sc-0.058 at% Zr following cold work and double aging treatment of tensile bars.

All Al-0.056 Sc-0.058 at% Zr as well as the Al-0.063 Sc-0.064 Zr tensile samples exhibited necking and ultimate failure along a plane roughly 45° from the testing direction. Examination of the fracture surfaces reveals that these bars failed intergranularly; the fracture surfaces (e.g. Figure 16) mimic the as-cast grain structure shown in Figure 1. A significant reduction in strength and elongation was observed when bars were solutionized after cold working (Table 3). The bars which exhibited low yield strength in the cold worked, solutionized, and double aged condition have a qualitatively higher microvoid density on grain boundaries indicating that the interiors of the grains are much stronger than the boundaries, and that the solutionization treatment further weakened the grain boundaries leading to lower tensile strength and elongation. This is also evidenced through post-mortem microscopy, in which it was observed that grains remained columnar with a clear partition line; nucleation of strain-free grains, or any refinement at all, was not apparent indicating that the solutionization treatment was ineffective. It is possible the bars did not reach a high enough temperature or the time spent at temperature was too brief to dissolve solute clusters/precipitates in order for new equiaxed grains to develop. From thermocouple measurements of this and similar aging treatments in resistance furnaces, it is argued that the heating rate is much too slow. In the resistance furnace, the solutionization temperature for 0.054 Sc of 520°C [23] was likely reached but the 630°C [24] necessary to re-dissolve the 0.061 Zr may not have been reached in an hour and the already developed distribution blocked recrystallization. A furnace treatment with more intimate contact should be used, such as a crucible furnace (salt pot). However, these types of immersion furnaces are typically limited to temperatures <500°C, which would not be high enough to solutionize Sc nor Zr.

The deleterious effect of an attempted solutionization treatment has been observed before, specifically in the findings of Knipling et al. [14] in Al-0.06 Sc-0.06 at% Zr and Jia et al. [57] in Al-Zr-Mn. Knipling et al. observed significant segregation of Zr during solidification of their castings and, as a result, the local concentration of Zr in dendritic cores exceeded the solubility limit of 0.071 at% at 640°C and Zr-rich precipitates formed during solutionization. This unintentional precipitation only occurred in the enriched regions and did reduce the potential strengthening that later aging treatments afford through a more homogeneous

dispersion. In the present study, this would explain the lower yield strength and lack of recrystallized microstructure, but not necessarily the deficient uniform plastic deformation and elongation.

#### 4.4 Challenges

There can be some difficulty in obtaining supersaturated solid solutions with Zr and Sc additions. Approximate diffusion distances for both Sc and Zr at several temperatures and times are presented in Table 9; diffusivity is determined by extrapolating  $\ln(D)$  vs  $1/T$  literature data to the temperatures of interest using an Arrhenius fit (per Figure 2) and diffusion distance is approximated by  $d = (2Dt)^{1/2}$ . The diffusion distance for scandium after six hours at 400°C is roughly one micron, indicating that even in the foundry, the Al-Sc-Zr and Al-Mg-Sc-Zr castings cool quickly enough (<15 minutes) to avoid primary precipitation by the fastest diffusing species of precipitate formers present. No primary precipitates were detected in foundry castings through backscattered imaging in the SEM.

**Table 9:** Estimated diffusivities and diffusion distances after 6 hours ( $d_6$ ) and 18 hours ( $d_{18}$ ) for Sc and Zr in aluminum. For scandium,  $D = 2.65 \times 10^{-4} \cdot \exp(-168,000/RT)$  [58] and for Zirconium,  $D = 7.28 \times 10^{-2} \cdot \exp(-242,000/RT)$  [8].

	Sc in Al			Zr in Al		
	D (m <sup>2</sup> /s)	$d_6$ (nm)	$d_{18}$ (nm)	D (m <sup>2</sup> /s)	$d_6$ (nm)	$d_{18}$ (nm)
275°C	$2.57 \times 10^{-20}$	33.3	57.7	$6.24 \times 10^{-25}$	0.2	0.3
300°C	$1.28 \times 10^{-19}$	74.5	129	$6.34 \times 10^{-24}$	0.5	0.9
375°C	$7.61 \times 10^{-18}$	573	993	$2.27 \times 10^{-21}$	9.9	17
400°C	$2.42 \times 10^{-17}$	1020	1770	$1.20 \times 10^{-20}$	23	40.

Upon aging a metal in practice, a single value of precipitate radius is never realized; there is always a distribution of particle sizes. During deformation, whether cold work or damage during end-use, small (i.e., soft) particles shear while larger particles are looped by moving dislocations. The particular slip system on which small particles are sheared becomes even more favorable after dislocations have sheared some of the obstacles, since the remaining particle cross sectional area is reduced, and shear-banding may result. This form of inhomogeneous deformation has lasting consequences and so overaged distributions are



typically desired in order to reduce the number of very small precipitates, at the cost of some yield strength by effectively increasing interparticle spacing.

A very narrow distribution of core-shell precipitates has recently been reported for the Al-Li-Sc system [59]. A double aging treatment is used where the first step is at high-temperature to precipitate  $\text{Al}_3(\text{Li}_{1-x}, \text{Sc}_x)$  rapidly, and the second step is performed at a lower temperature, allowing the remaining Li to form a shell on the existing particles. The innovative feature of this system is that during the shell-forming step, small precipitates grow faster than the large ones due to all of the existing particles being larger than the critical size for nucleation of  $\text{Al}_3\text{Li}$ ; the authors term these temperature and particle size conditions the size-focusing regime. The authors also relate the formation of these distributions to burst nucleation effects observed in colloidal solutions, qualitatively described by La Mer and Dinegar [60, 61] and quantitatively modeled by Robb and Privman [62], where an initially low monomer concentration in solution nucleates a narrow range of particles, and an injection of concentrated monomer increases size of the smallest particles faster than the larger ones, resulting in a narrow distribution of colloidal particle sizes (See [59-62] for more details). It may be possible to apply a modified aging treatment of this type to Al-Sc-Zr alloys, which could narrow the particle size spectrum (Figure 19) significantly. The high temperature aging temperature would need to be in the 450-500°C range to precipitate  $\text{Al}_3(\text{Sc}, \text{Zr})$  and retain some Sc in solution. There have been reports of heterogeneous particle distributions when aging Zr-containing alloys at high temperatures due to segregation of Zr during solidification which is not apparent with Sc, but if an isothermal 'pause' is added between 200 and 250°C during heating to the first aging temperature, it is feasible that a homogeneous distribution could be attained by allowing some  $\text{Al}_3\text{Sc}$  to nucleate first. Rapid heating to the high temperature step would be necessary to avoid rapidly coarsening the  $\text{Al}_3\text{Sc}$  distribution. Upon reaching the high temperature aging step, diffusion of Zr becomes appreciable and the precipitates may then grow via precipitation of  $\text{Al}_3\text{Zr}$ , and at this temperature, some Sc would prefer to stay in solution. Finally, the alloy could be direct quenched to an aging temperature around 300-325°C to bring all remaining Sc out of solution, which would increase the size of smaller precipitates faster than larger ones due to curvature, or size-focusing, effects. A schematic of this hypothetical aging treatment for Al-

Sc-Zr alloys is given in Figure 20. This type of treatment could potentially produce a narrow range of particle radii and interparticle spacing thereby increasing the observed yield strength and microhardness, without sacrificing much thermal stability.

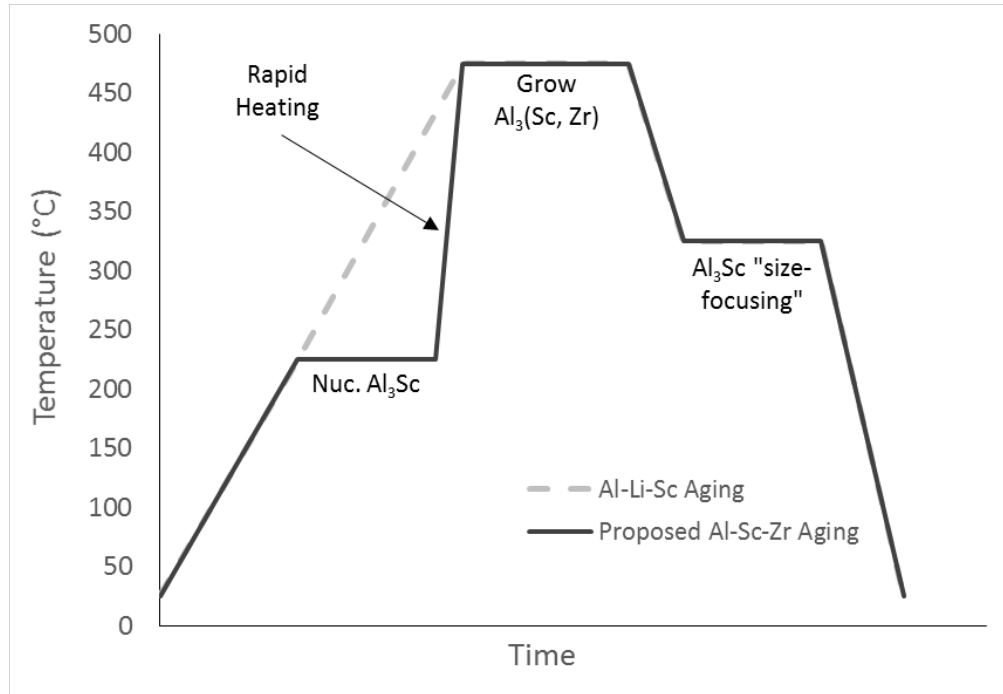


**Figure 20:** Hypothetical Al-Sc-Zr aging treatment to produce a narrow particle size distribution and improve mechanical properties.

Another difficulty when casting aluminum with Sc and Zr is solute segregation upon solidification. This effect results in areas of high and low solute concentrations, which consequently produces regions of high and low precipitate densities upon aging and therefore interparticle spacing [63]. There are two types: micro- and macro-segregation, where the former is also termed ‘dendritic segregation’ and the latter is of more concern in large ingots and is not considered here. Microsegregation occurs naturally as a result of non-equilibrium solidification, described by the Scheil equation, where the last to form solid has an elevated concentration of solute elements relative to the melt composition for eutectic systems, and is depleted of solute in peritectic systems, yielding solute-rich for the former, or solute-poor interdendritic channels for the latter [64]. In typical aluminum casting alloys, microsegregation is mitigated by solutionization treatments which allow significant solid

state diffusion to occur, but those treatments either become impossible or take prohibitively long times when dealing with slow-diffusing peritectic-type additions, such as Ti, Zr, and many of the rare-earth elements, which form highly stable aluminides. However, the grain refining efficacy of these same elements, and especially with the introduction of inoculant TiC or TiB<sub>2</sub> particles, continually interrupts the solid-liquid interface during solidification and limits this effect, especially when castings are cooled quickly thereby decreasing the width of dendrite arms as well as the interdendritic channels, so much so that the solidification is then described as 'non-dendritic'.

Lastly, it is recognized that the conversion from microhardness to yield strength, and vice versa, is a very rough estimate and exact correlation is not expected due to the fact that plastic deformation has definitely occurred during microhardness tests. While the hardness values come from multi-step aging treatments, and the tensile bars were double-aged, it is still useful to compare the observed yield strength increases. For example, the highest Mg content alloy had a hardness of  $933 \pm 9.6$  MPa, or a predicted yield strength of 311 MPa, but the tensile bars tested for this alloy averaged just  $193 \pm 2$  MPa, a difference of 37.9%. For the Al-0.056 Sc-0.058 Zr alloy, this difference is 35.6%.

## Conclusions

- A double aging treatment of 16 hr @ 275°C + 16 hr @ 400°C produces precipitates with average radii of 4.4 nm and tensile yield strength around 151 MPa in Al-0.056 Sc-0.058 at% Zr. This is an underperformance compared with predictions made by strengthening mechanism estimations as well as empirical hardness data.
- Alloys without scandium displayed very little precipitation hardening, indicating that Sc is a necessary addition for HSLA-Al near-net shape casting applications. Further, the most efficient precipitation is observed when equiatomic additions of Sc and Zr are made (Table 7 and Figure 17) in terms of microhardness.
- Grain refinement using Ti-B and Ti-C additions increase grain isotropy and Hall-Petch strengthening. Slight increases in yield and ultimate strength are expected, though tensile bars were not produced for this study. Samples which were 75% cold worked following aging reached microhardness values circa 400 MPa; therefore wrought

alloys based on the Al-Zr system may be feasible with, admittedly, mild age-hardening potential.

- Cold work prior to multi-step and double isothermal aging is mitigated by recovery at the required aging temperatures for Zr precipitation. This strengthening mechanism insufficient to partially replace Sc as an alloying addition.
- Fracture occurs via intergranular microvoid formation and rupture along a plane roughly 45° from the tensile testing axis; grain boundaries are the weak link in the large grained Al-Sc-Zr microstructure.
- A 1 hour solutionization treatment in a 638°C furnace directly following cold work is insufficient to homogenize the microstructure, and ultimately results in lower yield strength, ultimate strength, and elongation following the same double aging treatment.



## Chapter II: Recrystallization Resistance in Grain Refined Dilute Al-Zr Alloys <sup>2</sup>

### 1. Introduction

#### 1.1 Use of Zr in Combination with Al-Ti-B, Al-Ti-C

The aluminum-zirconium binary system features several intermetallic compounds on the Zr-rich side of the diagram but the entire Al-rich side of the diagram is dominated by  $\text{Al}_3\text{Zr}$  [65] (in wt%), formed through peritectic solidification. The solubility of Zr in pure aluminum at the peritectic temperature of 660.8°C [65] is only 0.033 at% (0.11 wt%) [24, 66]. At concentrations above the liquid solubility limit,  $\text{Al}_3\text{Zr}$  rapidly precipitates with the tetragonal  $\text{D}_{023}$  structure. As a result, in much of the aluminum that is intentionally alloyed with Zr, there exists a large amount of primary  $\text{Al}_3\text{Zr}$ , owing to the steep liquidus. The 20-100 micron diameter precipitates, though structurally tetragonal, have good lattice matching with FCC aluminum and serve as efficient nucleation points during solidification [67-71]. However, it has also been acknowledged that Zr is useful as a precipitation strengthener [5, 72] and recrystallization inhibitor [34, 73-78] when the metastable  $\text{L}_{12}$  structured  $\text{Al}_3\text{Zr}$  is formed in dilute alloys during aging treatments. Though a large volume of  $\text{Al}_3\text{Zr}$  formed during aging is not possible due to the very limited solubility, interparticle spacing can be kept low if precipitate sizes are in the nanometer range. In this case, the strategy favors achieving the maximum amount of Zr in solid solution.

If a hypoperitectic Zr addition is made by itself, castings develop large columnar grains that grow down thermal gradients, away from the mold walls. In practical cases, fine grained microstructures are desired as hot tearing becomes more unlikely and mechanical properties are more isotropic and so a strategy to refine the grain structure of dilute Al-Zr and other Al-TM systems is required. Fast cooling rates have a dramatic effect on grain size, as the undercooling required for nucleation and growth of new grains is reached much faster in the liquid ahead of the solidification front. In practice, it is often difficult to use fast cooling rates because mass production typically requires starting with large volumes of

---

<sup>2</sup> The content of Chapter II is intended to be submitted for journal publication.

material, traditional billets or continuous cast slabs for example. Another method is to introduce grain refining alloy additions.

Titanium is a well-known grain refining addition which acts as a powerful segregant, effectively slowing down the solidification interface by continually expelling aluminum atoms into the liquid ahead of the interface. Titanium also forms an  $\text{Al}_3\text{Ti}$  compound with a metastable  $\text{L}_{12}$  structure [79], and a stable  $\text{DO}_{22}$  structure with good lattice matching with aluminum [80]. Al-Ti-B and Al-Ti-C grain refiners are industry-proven and often used in low concentrations, with excess Ti to promote grain growth restriction. However, Zr has been reported to interrupt the grain refinement mechanism of Al-Ti-B [81-84] but since Zr is used in concentrations 3-10x the liquid solubility limit in current commercial alloys, a limited number of studies [82] have been performed on very dilute additions of Zr combined with Al-Ti-B or Al-Ti-C. With hypoperitectic additions, Zr may not interfere with the grain refinement mechanism and then be able to precipitate as  $\text{Al}_3\text{Zr}$  during aging to act as a strong recrystallization inhibitor.

The success of Al-Ti-X grain refiners in commercial grain refinement is due to two factors: the potency of inoculation particles,  $\text{TiB}_2$  in the case of Al-Ti-B and  $\text{TiC}$  in the case of Al-Ti-C, and the large growth restriction factor of solute Ti. There has been much controversy over the mechanisms which govern the refinement process [50, 69, 82-86], and much debate on whether the limiting factor in efficacy of refiners is the inoculant potency or the action of the solute, but the consensus is that both effects are necessary, reflected in a recent analytical model developed by Easton and St. John [87]. Though the alloy was glassy, had high levels of Ni, and was solidified rapidly from a much higher temperature than used for Al alloys, the exact mechanism by which nucleation occurs on  $\text{TiB}_2$  particles seems to have been demonstrated through a study by Schumacher and Greer [88] nearly twenty years ago using a novel melt spinner technique to investigate the early stages of nucleation. They found that a layer of  $\text{Al}_3\text{Ti}$  forms on the  $\text{TiB}_2$  particles prior to nucleation. A follow-up paper using the same method was performed to investigate the reason behind Zr-poisoning [81]. The authors concluded that zirconium interrupts the formation of the  $\text{Al}_3\text{Ti}$  layer that forms on  $\text{TiB}_2$  particles by substitution for Ti primarily in the  $\text{TiB}_2$  phase, although the obvious caveat was that this melt was held at 1150°C for several minutes which changes how Zr might

interact with the pre-existing  $TiB_2$  particles. In other studies, it was found that Zr-poisoning was much less of a problem when using Al-Ti-C [89], and this master alloy has risen in popularity as production methods have improved. While the effects of Zr on Al-Ti-B and Al-Ti-C have been studied in detail, the unique aspect of the current contribution is the use of electron backscattered diffraction (EBSD) to study the effect of Al-Ti-B and Al-Ti-C on the recrystallization resistance afforded by  $Al_3Zr$ .

## 1.2 Recrystallization Resistance

### 1.2.1 Optimizing the Precipitate Distribution

The earliest report on the effectiveness of Zr in retarding recrystallization indicated nothing special [90] at levels of 0.03, 0.21, and 0.45 wt%, and in fact, similar additions (by atomic fraction) of Mn were much more effective at preventing recrystallization following extrusion and one hour anneals ranging from 320 to 620°C. However, this study was performed on the solid solution obtained directly following chill casting, and no aging treatment was performed before or after deformation. Later reports (e.g. [74, 78]) established the efficacy not of Zr in solution, but of the very small dispersoids that form slowly during aging.

Artificial aging of aluminum-zirconium was then studied in detail using rapidly solidified hyperperitectic alloys by Ryum in 1969 [74] and Nes and Ryum in 1971 [91] followed by a subperitectic 0.18 wt% Zr alloy in 1972 [34]. Interesting fan-shaped precipitation features were observed in the hyperperitectic alloys which did not have any crystallographic dependence on the matrix, unlike similar precipitation features observed for  $Ni_3Al$  in nickel. These curved arrays of  $DO_{23}$  structured  $Al_3Zr$  were determined to be the result of discontinuous precipitation of  $Al_3Zr$  at moving grain boundaries in the supersaturated matrix. In practice, rapid solidification is rare and the hyperperitectic compositions produce primary  $Al_3Zr$  during casting. While these hyperperitectic alloys do display age-hardening upon heat treatment from precipitation of  $Al_3Zr$  from the remaining Zr in solid solution, the distribution of Zr throughout the microstructure is not ideal from an anti-recrystallization standpoint. The primary precipitates rob the matrix of solute available for the later aging treatment and are not effective as recrystallization inhibitors themselves.



Dilute additions can be quenched into solid solution up to a concentration of about 0.06 at% (0.20 wt%) by chill casting. In these alloys, an ideal Al matrix supersaturated in Zr allows the formation of fully coherent and randomly distributed  $\text{Al}_3\text{Zr}$  particles [34], which are approximately spherical hard obstacles to moving dislocations, low-angle grain boundaries (LAGB), and high-angle grain boundaries (HAGB). Upon annealing after mechanical deformation, they are too small to act as recrystallization nucleation sites [92], and force the structure to find another mode of reducing the stored energy of cold work.

J.D. Robson [93] developed a model to predict the optimum recrystallization resistant precipitate distribution in Al-Zr alloys. The results of this work indicate that a two-step treatment is most effective with an initial incubation period at  $T_1 = 0.88(T_2)$  followed by an extended aging time at  $T_2$ . Robson also suggests using a very slow heating rate (20 K/hr) to reach both temperatures; a heating rate of 60 K/hr is used herein as this is the lowest afforded by the controller on the crucible furnace. This has the effect of producing a wider distribution of precipitate sizes which increases the Zener pinning pressure exerted on a moving boundary. Eivani et al. [94] showed a 50% reduction in percent recrystallization of alloy 7020 containing 0.13 wt% Zr by using a heating rate of 323 instead of 523 K/hr to the solutionization temperature of 510°C attributed to higher Zener pinning pressure caused by a wider range of precipitate sizes.

The very low diffusivity of zirconium means long aging times at temperatures which are typically reserved for solutionization of commercial alloys (see Figure 2 and Table 1 for Zr and Ti). Ultimately, while these alloys are not expected to have exceptional yield strength, this strategy may provide a platform for fine-grained, wrought-processed, thermally-stable alloys.

Limited but influential work has been done in the ternary Al-Ti-Zr system in regard to precipitation reactions [71, 72, 95]. Knipling et al. [72, 95] recognized the potential of these alloys for higher temperature applications outside of the range of current aluminum alloys. Both Al-Ti and Al-Zr are terminal peritectic systems with low liquid and solid solubilities. The equilibrium phase that forms from supersaturated solid solution in both of these systems is  $\text{Al}_3\text{X}$ , and both  $\text{Al}_3\text{Zr}$  and  $\text{Al}_3\text{Ti}$  are tetragonal in structure, though a metastable form in the

cubic L1<sub>2</sub> configuration exists beforehand in both cases. Significant mutual solubility of Zr in Al<sub>3</sub>Ti and Ti in Al<sub>3</sub>Zr and the ternary alloy resulted in significantly higher hardness than either binary alloy [72, 95]. The difficulties encountered with these alloys, however, was the significant partitioning of solute to the cores of solidifying grains, which leaves very solute-poor interdendritic regions and therefore heterogeneous precipitate distributions upon aging.

### 1.2.2 Mechanisms of Recrystallization

It has been shown that nanoscale zirconium trialuminide [73-78] and scandium trialuminide [22, 77, 96, 97] both produce very fine precipitates with the L1<sub>2</sub> structure and stabilize fine grain structures through the same mechanism by exerting Zener pinning pressure on moving low and high-angle grain boundaries [46, 96, 98-103]. Dilute aluminum-zirconium alloys develop a fine subgrain structure when significant deformation occurs due to the high stacking fault energy of the Al matrix. Upon heating, recovery occurs as dislocations begin to undergo diffusion-accommodated migration in order for the structure to approach a lower energy state. Some dislocations interact and annihilate, while others reach subgrain boundaries where they are pinned by the trialuminide precipitates. Accumulation of dislocations at these boundaries has been shown to convert these low-angle subgrain boundaries to high-angle grain boundaries in alloys containing very fine precipitates. If the alloy is further annealed, grain rotations tend to occur which result in some grain growth [104, 105]. This particular mode of recrystallization results in retention of the texture and grain shape introduced during processing (i.e. elongated grains in the rolling direction) and is known as continuous recrystallization. A recent model by Ferry et al. [106, 107] treats the grain rotation mechanism as diffusion accommodated rotation within an orientation gradient and in the presence of fine scale particles.

A similar effect been termed grain boundary sliding (GBS) in other sources [46, 96, 98, 99], though the latter terminology is typically applied to the evolution of mechanically loaded specimens with an efficient pinning second phase present, such as in superplastic alloys. The precipitates themselves are highly stable against growth and do not coarsen significantly up to temperatures approaching 475°C [108]. When superplastic material is

deformed at elevated temperature (450-500°C) and strain rate ( $10^{-1}$ - $10^{-2}$  s $^{-1}$ ), elongations in excess of 1000% may be realized (e.g. [103]). A binary Al-Zr alloy was even shown to exhibit 500% elongation at 500°C and a strain rate of  $10^{-1}$  s $^{-1}$  [101]. The effect of very fine Al<sub>3</sub>Zr was utilized in the development of Supral in the mid-1970s, a commercial Al-Cu-Zr alloy [78, 109, 110], where Cu is added in this particular alloy to lower the stacking fault energy of the matrix and provide more driving force for dynamic recrystallization to occur, while the nanoscale trialuminides stabilize grain size and allow superior formability. During the 1990's, much interest was devoted to understanding the next logical step, adding zirconium to commercial grade 7XXX, 6XXX, and 2XXX alloys for grain size control, as well as utilizing superplasticity in other systems such as Ni-Al [111]. Additionally, precipitate-free zones became less precipitate-free and some alloys that could only be joined mechanically became weldable. In addition, it was quickly found that all of these properties got even better when used in conjunction with Sc.

### 1.2.3 Particle Stimulated Nucleation

In commercial aluminum alloys, recrystallized grains are often observed to have nucleated at large intermetallic particles which may be added to the melt, formed during solidification and cooling, or formed during thermal treatment. The volume of material up to one particle diameter away from an incoherent intermetallic becomes much more distorted than the surrounding matrix during deformation and this region serves as an effective nucleation zone for strain free grains upon heating the material which may occur during working or afterwards. This effect was studied in detail [92] based on the effects observed by Humphreys [41, 112] and has now been termed particle stimulated nucleation (PSN). The model given by Sandstrom provides the particle size necessary to promote nucleation of a strain free grain following a given amount of deformation. In pure aluminum, at a deformation of 80%, the particle must be greater than 2 μm in size. At 50% deformation, the critical size is 4 μm, and this value increases rapidly with decreasing strain. This is based on the observation that the deformation zone around the particle must be equal to or greater than the classically determined critical radius for nucleation of a recrystallized grain ( $R_{CR}$ ), otherwise the grain cannot continue to grow into the relatively undeformed matrix outside of this zone. Nes and Ørsund [113] improved upon this by considering a second case in which

the strain free grain nucleates in the deformation zone, but not on the nucleant particle itself at the center of the deformation zone, based on observations in Al-Mn alloys that random texture was obtained after annealing at high temperatures and remnants of the rolling texture remained after annealing at lower temperatures indicating a change in recrystallization behavior [114]. The nuclei generated away from the center of the deformation zone had an orientation dependence on the surrounding matrix, while those that nucleate at the center are randomly oriented. As a result, a fully recrystallized grain structure shows random orientation texture in the case of nucleation at the center of the deformation zones, and will exhibit remnants of the deformation texture if matrix oriented subgrains form and consume the deformation zones. Their model successfully captured this effect, and Nes and co-author Marthinsen [42] went on to develop a ‘unified theory of deformation’ for aluminum alloys.

#### 1.2.4 Predicting Recrystallized Grain Size during Static Annealing

There has been much interest in understanding the pinning pressure exerted by very small trialuminide precipitates in low-alloyed aluminum. Zener, whose work was communicated by C.S. Smith [115], derived a rough expression for the pinning pressure exerted by a particle on a boundary. He then elaborated for the case of pinning by a population of particles on a boundary, given by Equation 12 [116]. Although much work has been done to refine this original expression, his estimate has remained empirically accurate for low volume fractions of precipitates, as reviewed by Nes et al. [116, 117]. With a homogeneous spatial distribution of ideal spherical precipitates, pinning pressure is estimated as:

$$P_Z = \beta \frac{f\gamma}{R} \quad \text{Equation 12}$$

where  $f$  is the volume fraction of pinning precipitates,  $\gamma$  the boundary interface energy, a result of the differences in surface tension, and  $R$  is the average particle radius. Zener and Smith’s original value of  $\beta$  is 0.75, but it varies up to about 2.25 depending on the subsequent analysis cited (1.5 is most common [116]). In reality, there are many complications when dealing with the 3-D treatment of a boundary moving through a field of

precipitates. To name a few, the size and spatial distribution [93, 94], shape [118], coherency [119], and potential boundary-induced reversion of precipitates [116] as well as the curvature of the boundary [116] and attractive and restraining effects by particles in front and behind the boundary [117, 120], respectively. What is relevant here is that pinning particles must be as small as possible (Equation 12) and coherency increases the pinning pressure, approximately twofold [116, 119]. This latter effect is the result of the strain field produced in the vicinity of coherent particles, where very little strain is present surrounding incoherent particles, and is significant in the alloys considered here.

Particles produced through age-hardening of an Al-Zr solid solution are most effective as both grain boundary pinners and precipitation hardeners at diameters one to two orders of magnitude smaller than the  $R_{CR}$  for heavily worked aluminum and so they do not serve as nucleation sites for recrystallized grains. In the absence of PSN, new grains form in three ways during static annealing in a material with very fine precipitates: subgrain growth and coalescence, nucleation and growth in anisotropic deformation regions (e.g. shear bands), or nucleation and growth at prior grain boundaries. However, when a grain refiner such as Al-Ti-C or Al-Ti-B is utilized in the casting process for Al-Zr alloys, large intermetallic particles which serve as nucleation sites for the original grains are present and continue to serve as efficient nucleation sites for recrystallized grains.

Wert and Austin [121] have provided a model to predict the recrystallized grain size in systems containing both nucleating particles and dispersed pinning particles in aluminum by expanding on Nes et al.'s [122] previous work. This model bases the transformations observed during recrystallization on Johnson-Mehl-Avrami concepts developed much earlier for phase transformations. Wert and Austin [121] compare the expected grain sizes following recrystallization ( $D_R$ ) for site-saturated and Johnson-Mehl kinetic cases:

$$D_R(SS) = [N_V(d_c)]^{-1/3} \quad \text{Equation 13}$$

$$D_R(JM) = \left[ \frac{G}{vN_V(d_c)} \right]^{1/4} \quad \text{Equation 14}$$

where  $N_V(d_c)$  refers to the density of particles with diameters larger than the critical diameter to form a large enough deformation zone during processing to nucleate a new

grain during annealing,  $\nu$  is the nucleation frequency, and  $G$  is the growth rate of the newly nucleated grain. The growth rate is expressed as:

$$G = M(P_D - P_Z) \quad \text{Equation 15}$$

where  $P_D$  is the driving pressure for recrystallization due to deformation and  $M$  is the mobility of the boundary;  $P_Z$  is the Zener pinning effect, described by Equation 12. Wert and Austin assume nucleation and growth rates are constant in this model, as no empirical data existed at the time to incorporate the effect of recovery on these two aspects. As a critical parameter in the model for growth rate, the stored energy due to deformation ( $P_D$ ) was experimentally determined by calorimetry techniques following different levels of cold work for an Al-0.115 at% Zr alloy [121]. Consolidation of the above equations gives:

$$D_R(JM) = K_{JM} \left[ \frac{P_D - P_Z}{N_V(a_c)} \right]^{1/4} \quad \text{Equation 16}$$

where  $K_{JM}$  includes the boundary mobility and nucleation frequency and is treated as an empirical constant. According to this relation, as the number density of nucleation sites (TiB<sub>2</sub> and TiC particles) and the volume fraction of Zener pinning particles (Al<sub>3</sub>Zr and Al<sub>3</sub>Ti precipitates) increase, grain size decreases.

In the present alloys, when no grain refining additions are made the relation breaks down and it is predicted that recrystallization will occur “continuously”, i.e., by subgrain rotation, as discussed in section 1.2.2. In these cases, retention of the texture and grain aspect ratios in the swaging direction from cold work are expected to remain following recrystallization. When grain refiners are added, equiaxed recrystallization nuclei are predicted to form via PSN, and Zener-pinning limited growth of these new grains occurs to grain sizes predicted by Equation 16.

### 1.3 Mitigation of Dendritic Segregation

An issue that is prevalent when casting Al-Zr alloys is dendritic segregation. The partitioning of solute near a solidification interface results in Zr-rich interdendritic cores which become prone to formation of Al<sub>3</sub>Zr during cooling according to Scheil-governed dendritic solidification. Consequently, the interdendritic channels and areas near grain

boundaries, poor in zirconium, do not form a high enough density of precipitates upon aging to effectively resist grain and subgrain boundary motion [93]. Homogenization treatments are typically used to re-distribute solute in aluminum alloys, but this becomes difficult or impossible with the combined slow diffusivity of Zr and high stability of the terminal Al-rich phase in peritectic type alloys. In comparison to binary Al-Zr alloys, microsegregation of Zr may be reduced as the dendritic solidification is confined to smaller and smaller cells which are themselves continually interrupted by new nucleation events on TiB<sub>2</sub> and TiC particles in the grain refined alloys here.

#### 1.4 Scope of this Contribution

The scanning capabilities of modern EBSD equipped electron microscopes have enabled complex studies to be performed that accurately reveal as-cast and recrystallization structures in Al-Zr alloys over a range of compositions and severity of thermomechanical processing (TMP) treatment (e.g. [98, 103]). In this study, efficacy of Al-Ti-B and Al-Ti-C grain refining additions and their interactions with Zr is assessed through changes in as-cast grain size. The swaging technique used herein then produces a single precise level of cold work as a result of sample geometry during deformation processing. Samples are annealed under rapid heating and quenching conditions to observe the change in density of HAGB and LAGB at 400 and 500°C as a measure of amount of recrystallization. Grain sizes and aspect ratios in the longitudinal plane relative to as-cast grain sizes are measured as an assessment of the mechanism of recrystallization.

Specifically, two hypotheses are tested:

- 1) If the concentration of Zr is increased from sub-peritectic (<0.03 at%) to hyper-peritectic (>0.03 at%) levels, the grain refinement capacity of commercial Al-Ti-B and Al-Ti-C decreases due to Zr-poisoning of the refinement mechanism.
- 2) If TiC or TiB<sub>2</sub> particles are present in peak-aged Al-Zr, the recrystallization mechanism will change from subgrain coarsening to particle stimulated nucleation (PSN).

## 2 Methods

### 2.1 Casting

An Al-Zr master alloy was first dilution cast to a target composition of 0.115 at% in the foundry via the method described in Chapter I of this contribution. This was done to ensure all existing  $\text{Al}_3\text{Zr}$  in the 10.2% Zr master alloy was fully dissolved before producing the final Al-Zr compositions in smaller heats. For the subsequent smaller heats of the target compositions, a graphite crucible and 650 grams of charge material were inductively heated under argon cover gas and poured into a boron nitride coated steel mold at room temperature using a computer-controlled servo motor in a custom vacuum induction melter (VIM) (Michigan Tech, Houghton MI). Grain refining additions of Al-10 wt% Ti (Milward, Minneapolis MN), Al-5 Ti-1 wt% B (AMG Aluminum, Robards KY), or Al-3 Ti-0.15 wt% C (KBM Affilips, Oss The Netherlands) master alloys were added 60 seconds prior to pouring.

The mold produced two bars 19 mm in diameter and 150 mm long of each composition for study purposes, in addition to the gating and sprues. An unlubricated and clean 13 mm drill was used to remove material from the gating of each casting to be dissolved in  $\text{HCL}+\text{HNO}_3$  for ICP-OES compositional analysis. Additionally, the castings were subjected to x-ray imaging using a BuckyDiagnost system (Philips Healthcare, Andover MA) operated at 67 kV at UP Health System-Portage Hospital for identification of any shrinkage porosity or other casting anomalies. Resolution of this technique is on the order of 0.5 mm.

The bars were marked and removed from each casting; 10 mm long slices were taken from the bottom and top of each bar and mounted for reflected light and scanning electron microscopy of the transverse sections. Using a high speed diamond saw, 4 mm slices were taken for longitudinal sections.

### 2.2 Thermomechanical Processing

The bars were double-aged in liquid salt of a 50/50  $\text{KNO}_3\text{-NaNO}_2$  solution in crucible furnaces at 375 and 410-440°C with ramp rates of 60°C/hr to each temperature. Full bars were aged this way in a single processing step (no quench between aging steps). Samples of



aged bars were taken and mounted for SEM, while the remainders of the bars continued to the cold work process.

A single level of cold work was obtained via a rotary swager (Fenn, Newington CT). Diameters of the bars were reduced from 19 mm to 9.5 mm in 6 steps for a total of 75% reduction in cross-sectional area (%CW). Again, archive samples were taken for SEM. Cold worked samples were allowed to stabilize at room temperature for 24+ hours before annealing treatments. Two orientations were examined in this work, NDND and NDSD, where ND refers to any direction normal to the working surface of the rotary dies and SD to the swaging direction (direction of feed). This coordinate system is shown schematically in Figure 21.

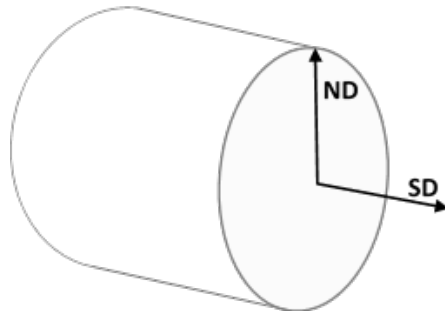


**Figure 21:** Schematic representation of normal and swaging directions; the transverse section corresponds to the NDND plane.

Finally, the swaged bars were cut into 6 mm slices using a high speed diamond saw, these pieces were then labeled and de-burred. One 6 mm slice from each composition went in a small basket for immersion in the crucible furnace containing a 50/50 mix of  $\text{KNO}_3$  and  $\text{NaNO}_2$  at either 400, 450, or 500°C for 24 hours followed by quenching into room temperature water. A complication arose for the NDND 500°C treatment, where the lab was inaccessible due to an unannounced “practice” emergency shutdown of the building, so these samples were annealed for 48 hours. Temperature was recorded throughout each treatment.

Vickers microhardness was measured (Leco, St. Joseph MI) throughout processing with a minimum of 15 indentations per sample, spaced at 1 mm, and conductivity was

measured (Fischer Technology, Windsor, CT) on as-cast and aged specimens, as the diameters of cold worked and annealed samples were too small to measure with the current instrumentation.

### 2.3 Optical and Electron Microscopy

Reflected light microscopy was performed on a PMG-3 metallograph (Olympus, Tokyo Japan) with the use of a polarizing filter, an adjustable Nomarski interference contrast filter, and a color tint filter. A three megapixel camera output images to imaging software run on an Eee 1000HE netbook (Asus USA, Fremont CA). Each sample was imaged from top to bottom in three columns with overlapping edges. Each series of images (21 for cold worked or annealed samples, 39 for AC or Aged) was stitched in Image Composite Editor (Microsoft, Redmond WA) which aligned the images and can create an overlay which blends the frame edges together resulting in a full seamless picture of the grain structure, although lighting conditions are critical for this latter operation and it was not always used due to variations across the image sensor when acquiring the micrographs. Grain sizes were measured optically for large grained samples by the lineal intercept method using circular geometry to minimize elongated grain effects on average grain diameter. In these cases (pure Al, for example), grains were so large that the stitched composite images were used for grain size measurements.

Initial backscattered and secondary electron imaging (BSE, SEI) was performed at 20 kV on a JEOL JSM-6400 (Peabody MA). Scanning electron backscatter diffraction (EBSD), electron dispersive spectroscopy (EDS), and foreshattered electron imaging (FSE) was performed in collaboration with the Institute for Frontier Materials (IFM) at Deakin University on a JEOL JSM-7800F (Peabody, MA) equipped with an Oxford X-Max EDS detector and Oxford NanoNordys EBSD detector (Abingdon, UK). The metallographic samples used for prior analyses were electropolished in a perchloric acid solution (see Appendix I for details) for EBSD measurements. Sample tilt was 70° when acquiring foreshattered and EBSD data, and all EBSD scans were collected at 20 kV, unless coupled with EDS spectra, in which case voltage was dropped to 10 kV to minimize the interaction volume. EBSD image processing included a noise reduction algorithm which was iterated to 0.00% noise, as well as wild peak

reduction. Grain sizes for the refined microstructures were measured automatically using an ellipse-fit algorithm on EBSD scans using the Oxford Channel5 software (Abingdon, UK) with grain boundaries defined as having greater than 15° misorientation between regions. Scale bars were added using the open-source NIH ImageJ editor; brightness and contrast enhancements were made using FastStone (open-source) for clarity. Metallographic preparation is detailed in Appendix I.

### 3 Results

#### 3.1 Alloying Levels

Nominal and experimental compositions determined by ICP-OES are given in Table 10. Fe and Si were measured at less than 0.02 at% in all cases. Only nominal concentrations for boron and carbon are given, as these are exceedingly difficult to measure by ICP-OES. Additionally, the LP13 composition had undissolved residue remaining following digestion for ICP-OES, and the Ti reading was very low, so this value is unknown, but is on the order of 5x the other Ti-added concentrations and so an exact measurement is not strictly necessary.

**Table 10:** ICP-OES measured compositions of LP series alloys

AC HV rank	ID	Zirconium (at %)		Titanium (at %)		Boron (at %)	Carbon (at %)	
		Nom.	Act.	Nom.	Act.	Nom.	Nom.	
1	LP14	-	<b>0.000</b>	-	<b>0.000</b>	-	-	Control
2	LP17	0.010	<b>0.008</b>	-	<b>0.00</b>	-	-	Low-Zr
3	LP16	0.010	<b>0.008</b>	0.070	<b>0.068</b>	-	0.014	
4	LP15	0.010	<b>0.009</b>	0.070	<b>0.090</b>	0.062	-	
5	LP12	0.030	<b>0.075</b>	-	<b>0.001</b>	-	-	High-Zr
6	LP09	0.030	<b>0.081</b>	0.070	<b>0.069</b>	-	-	
7	LP11	0.030	<b>0.075</b>	0.070	<b>0.075</b>	0.062	-	
8	LP10	0.030	<b>0.073</b>	0.070	<b>0.085</b>	-	0.014	
9	LP13	0.015	<b>0.029</b>	0.400	<b>N/A</b>	-	0.080	High-TiCar

Vickers microhardness measurements taken in the as-cast, aged, and cold worked state are shown in Chapter I of this publication, Figure 13. Conductivity for as-cast (AC) and

as-cold-worked (ACW) material is included in Section 4.2, in conjunction with a discussion of hardness data.

## 3.2 Optical and Electron Microscopy

### 3.2.1 As-cast Microstructures

Representative FSE images with EBSD overlays of as-cast structures for all nine alloys are shown in Figure 22. These EBSD scans were used for grain size measurements using the Channel5 software for the refined alloys; samples with very large grains were measured using composite images created from stitching optical micrographs together; an example of this is given in Figure 23. As a disclaimer, some polishing artifacts exist in the optical images, and are not discussed as microstructural features. Primarily, this refers to randomly distributed pitting which occurs when voltage is too high during electropolishing, and scratches from diamond polishing steps, which may be 1-10  $\mu\text{m}$  wide. The Al-Ti-B and Al-Ti-C grain refiners produce highly refined microstructures. Dispersed boron and carbon laden particles serve as efficient nucleation sites; grains in these castings are equiaxed and decrease in size dramatically.

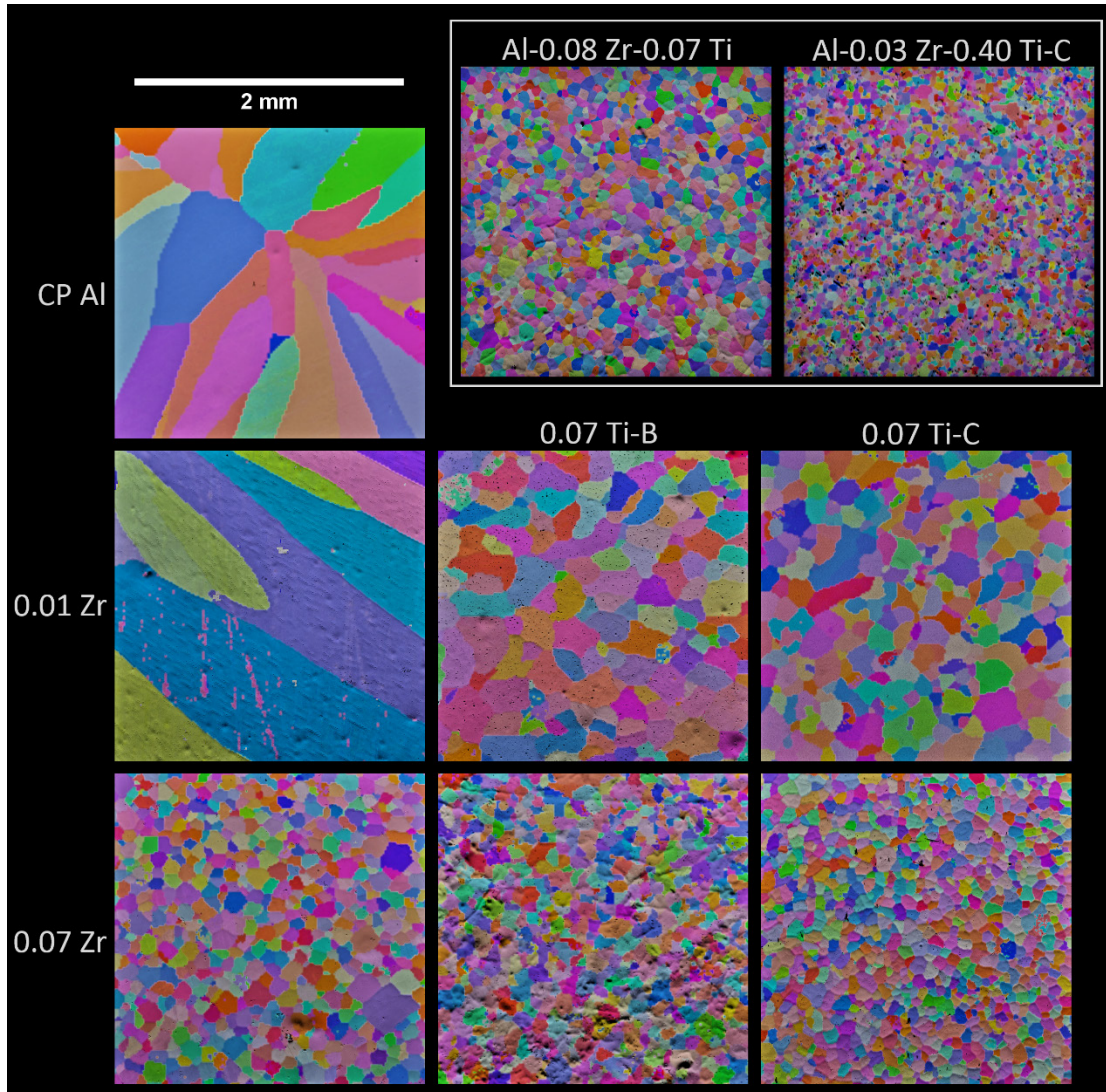


**Figure 22:** Representative FSE images with EBSD overlays for as-cast Al-Zr alloys; all panels are presented at the same scale.



**Figure 23:** Stitched macrograph of 99.99% Al for grain size measurements

Backscattered and secondary electron imaging are used to check the as-cast structures for the presence of impurities, microscale voids, and primary  $\text{Al}_3\text{Zr}$  precipitates. The SEM is also a useful tool for assessing the relative distribution of Ti and Zr by using EDS x-ray mapping. EDS maps for Zr and Ti are shown for alloys Al-0.01 Zr-0.07 Ti-0.062 at% B and Al-0.03 Zr-0.40 Ti-0.080 at% C in Figures 24 and 25, respectively. Precipitates formed during artificial aging, however, were not directly observed even with the field emission (FEG) equipped SEM. No microstructural changes, including grain size, are observed in optical micrographs of aged sections, and those images are omitted here.

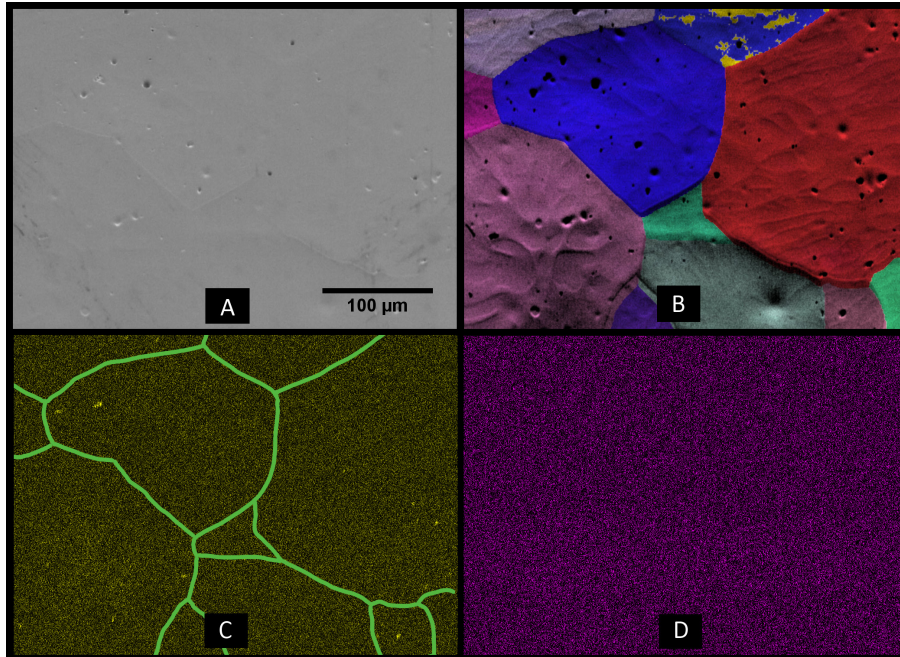


**Figure 24:** As-cast Al-0.01 Zr-0.07 Ti-0.062 at% B alloy. A) Backscattered image; B) Fore-scattered image with EBSD overlay; C) EDS x-ray map of Ti with traced boundaries from panel B; D) EDS x-ray map of Zr

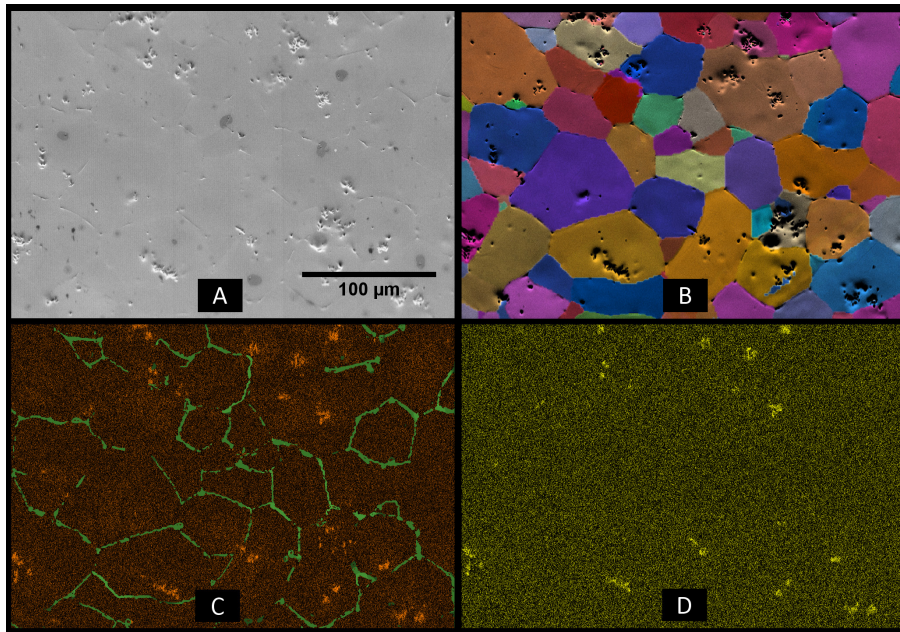


**Figure 25:** As-cast Al-0.03 Zr-0.40 Ti-0.08 C alloy. A) Backscattered image; B) Fore-scattered image with EBSD overlay; C) EDS x-ray map of Ti with traced boundaries from panel B; D) EDS x-ray map of Zr

### 3.2.2 Thermomechanically Processed Microstructures

For pure aluminum prepared through the same processing as the alloyed samples in this study, EBSD scans are presented in Figure 26 as a reference. Cold worked and annealed sections are generally imaged in two planes: NDND and NDSD, where ND is the direction normal to the swager die surface (i.e. radial), and SD is the swaging direction. In some cases, low ( $>2^\circ$ ) and high-angle ( $>15^\circ$ ) grain boundaries are highlighted with thin black and thin white lines, respectively. Panels C and D of Figure 26 are a single image of the cold worked NDSD orientation where the right half has grain boundaries shown in black and white (D) and the left half does not (C) illustrating the very fine subgrain structure that is formed in pure aluminum following 75% cold work. Upon annealing at 400 and 500°C, shown in panels E and F, respectively, the NDND structure is fully recrystallized and equiaxed, as is the NDSD section (panel G) after annealing at 500°C.

Cold worked NDND and NDSD sections for the four alloys containing 0.07 at% Zr are shown in Figures 27 and 28, respectively. NDND sections following 24 hr at 400 and 500°C are shown in Figures 29 and 30, respectively. Finally, NDSD sections following 24 hr at 500°C are shown in Figure 31. For consistency, the panels in Figures 27-31 correspond to the same compositions in each figure, i.e. **A)** Al-0.08 Zr-0.07 at% Ti; **B)** Al-0.07 Zr-0.07 Ti-0.014 at% C; **C)** Al-0.07 Zr-0.07 Ti-0.062 at% B; **D)** Al-0.07 at% Zr.



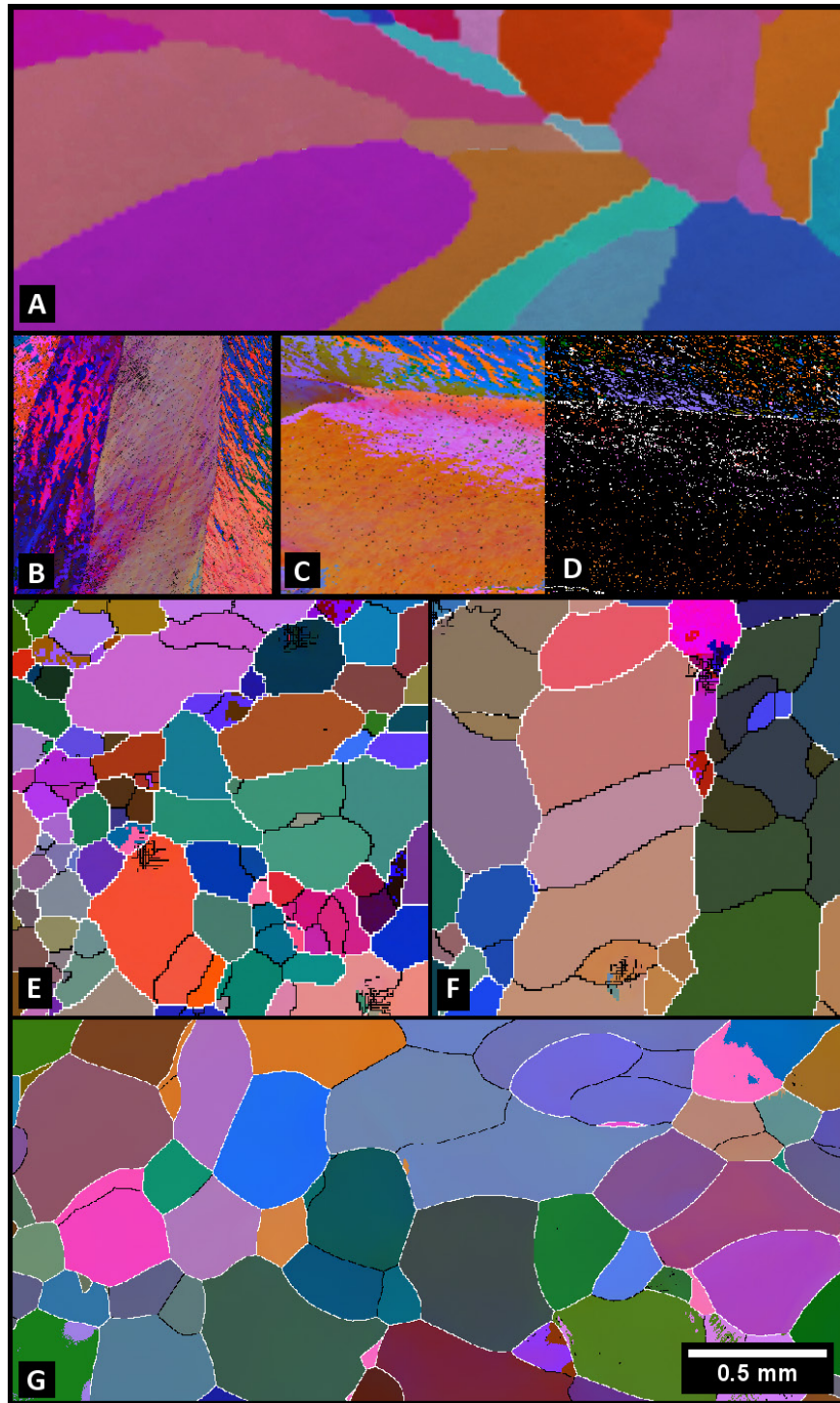


**Figure 26:** EBSD maps of pure aluminum represented throughout processing. A) As-cast; B) 75% cold work, NDND orientation; C) 75% cold work, NDS orientation; D) continued from C with LAGB shown in black, and HAGB in white; E) Annealed 24 hours at 400°C, NDND; F) Annealed 48 hours at 500°C, NDND; G) Annealed 48 hours at 500°C, NDS orientation.

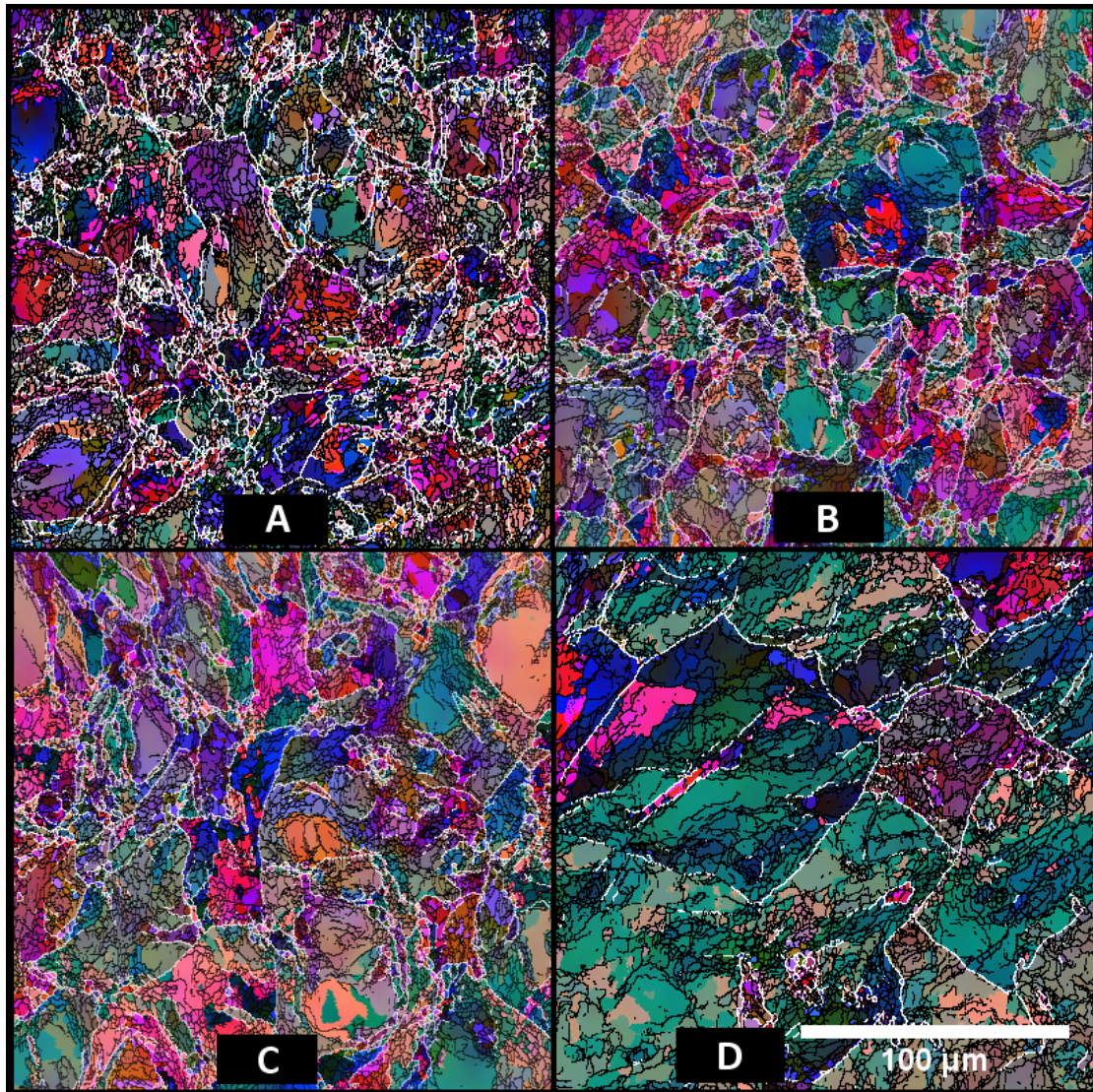


**Figure 27:** As-cold worked (75%) EBSD scans from NDND sections with HAGB ( $>15^\circ$ ) highlighted in white, and LAGB ( $>2^\circ$ ) in black. A) Al-0.08 Zr-0.07 Ti, B) Al-0.07 Zr-0.07 Ti-C, C) Al-0.07 Zr-0.07 Ti-B, and D) Al-0.07 at% Zr

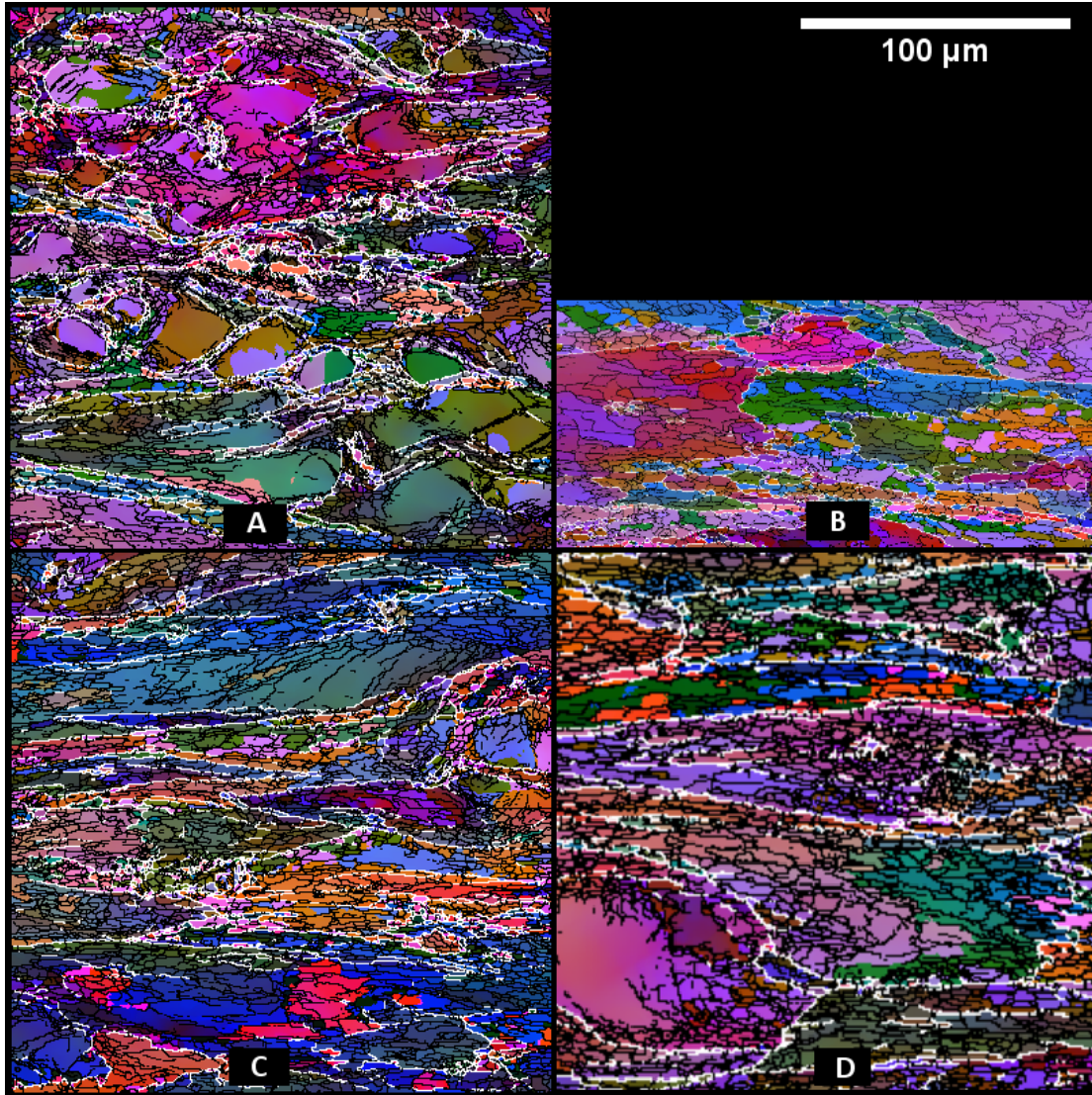


**Figure 28:** As-cold worked (75%) EBSD scans from NDSD sections with HAGB ( $>15^\circ$ ) highlighted in white, and LAGB ( $>2^\circ$ ) in black. A) Al-0.08 Zr-0.07 Ti, B) Al-0.07 Zr-0.07 Ti-C, C) Al-0.07 Zr-0.07 Ti-B, and D) Al-0.07 at% Zr

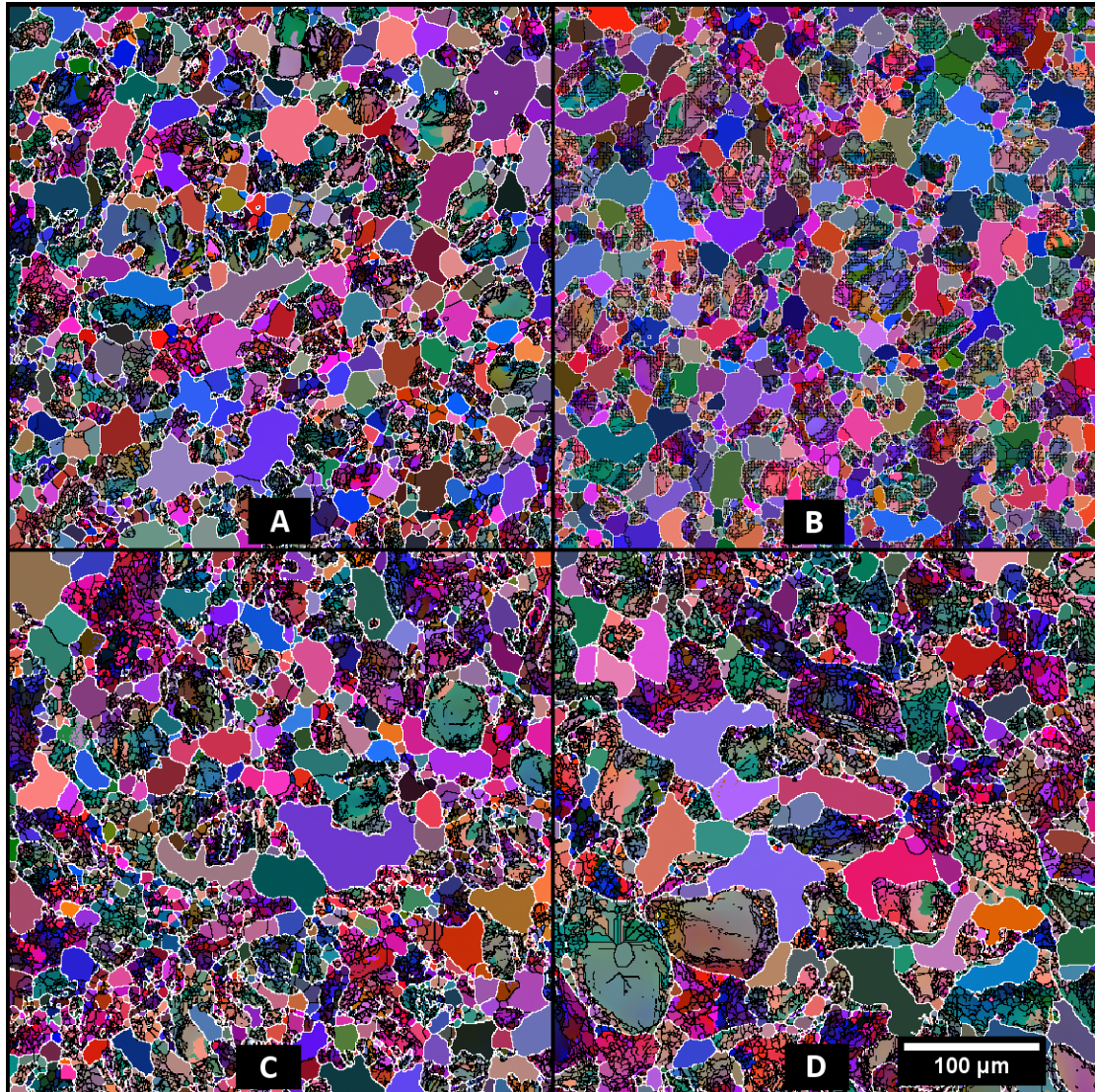


**Figure 29:** Partially recrystallized microstructures following 24 hr at 400°C. EBSD scans from NDND sections with HAGB ( $>15^\circ$ ) highlighted in white, and LAGB ( $>2^\circ$ ) in black. A) Al-0.08 Zr-0.07 Ti, B) Al-0.07 Zr-0.07 Ti-C, C) Al-0.07 Zr-0.07 Ti-B, and D) Al-0.07 at% Zr

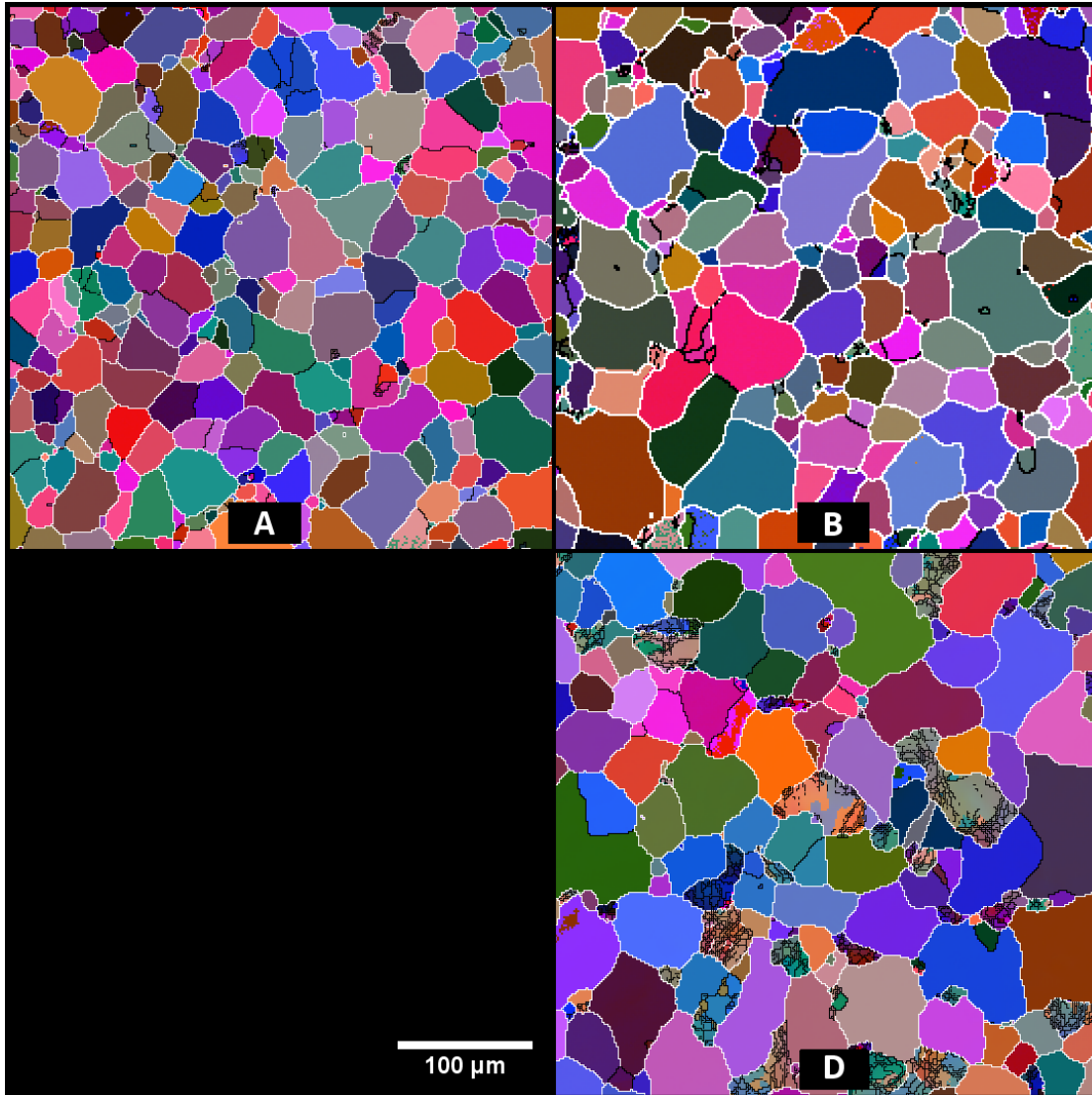


**Figure 30:** Partially recrystallized structures following 24 hr at 500°C. EBSD scans from NDND sections with HAGB (>15°) highlighted in white, and LAGB (>2°) in black: A) Al-0.08 Zr-0.07 Ti, B) Al-0.07 Zr-0.07 Ti-C, (Al-0.07 Zr-0.07 Ti-0.062 was not successfully imaged for this condition), and D) 48 hr at 500°C: Al-0.07 at% Zr

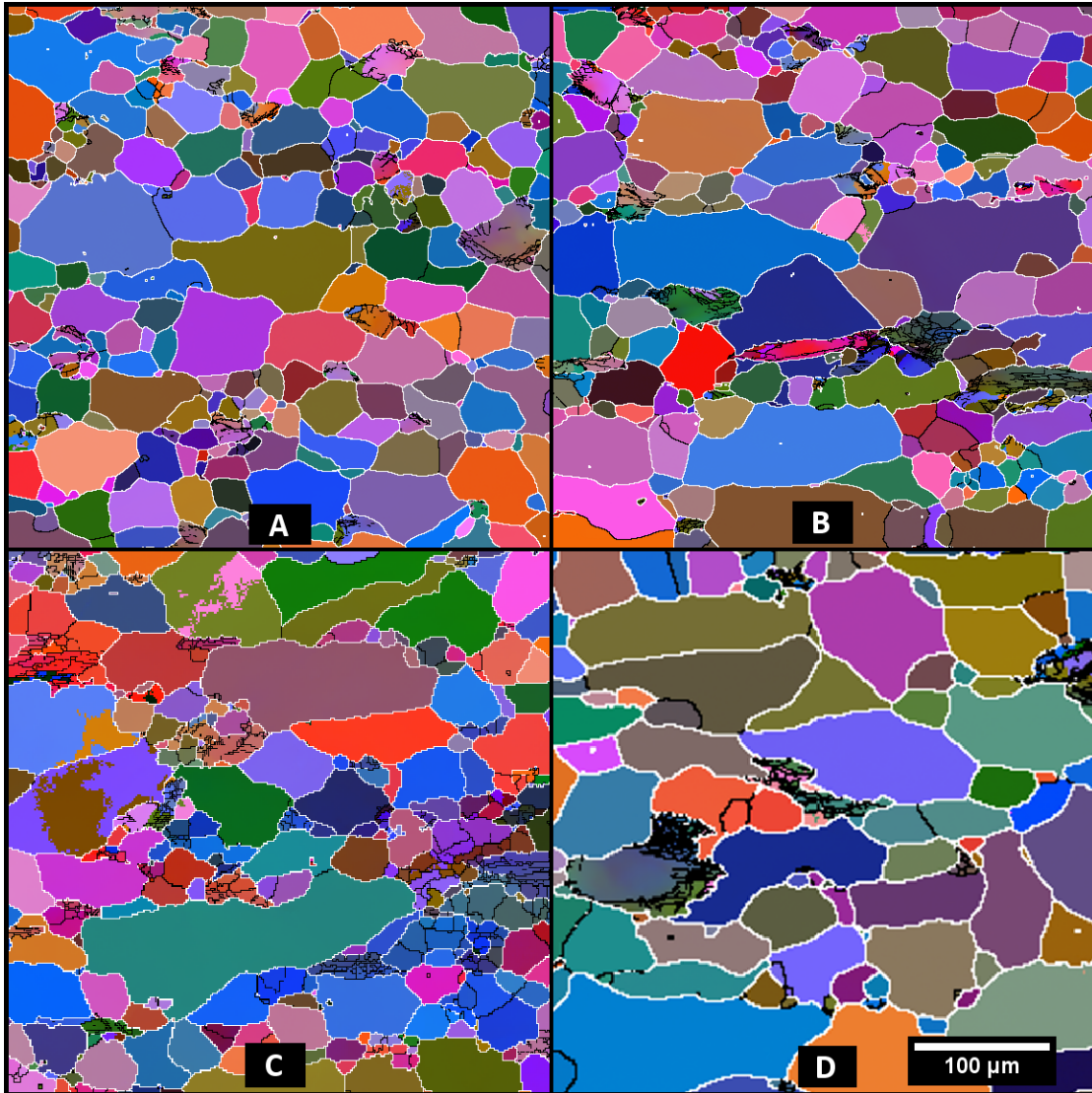


**Figure 31:** Microstructures following a 24 hr anneal at 500°C; EBSD scans from NDND sections with HAGB ( $>15^\circ$ ) highlighted in white, and LAGB ( $>2^\circ$ ) in black. A) Al-0.08 Zr-0.07 Ti, B) Al-0.07 Zr-0.07 Ti-C, C) Al-0.07 Zr-0.07 Ti-B, and D) Al-0.07 at% Zr

## 4 Discussion

### 4.1 Determination of Grain Size and As-cast Observations

Pure aluminum and Al-0.01 Zr exhibit columnar grain structure as a result of heterogeneous nucleation on mold walls and solidification proceeding down the thermal gradient (generated through conduction by the mold) towards the centers of the castings

(Figure 22). Very little nucleation occurs in front of advancing grain boundaries, indicated by the full radial span of many of the columnar grains. For the alloys which exhibit equiaxed structure in the as-cast state, average grain diameters are shown in Figure 32. As-cast and aged hardness values are also presented in Figure 32, which illustrates the ability of the material to harden due to solute Ti and Zr remaining in solution. It is noted that Al-Ti-C is more effective than Al-Ti-B at reducing grain size when added to Al-0.01 at% Zr, and this is also reflected in the increased hardenability upon aging. Both of these effects are evidence of Zr interaction with the Al-Ti-B master alloy during solidification, and not with the Al-Ti-C, consistent with literature observations [69, 89]. This trend is repeated when these two master alloys are added to Al-0.07 at% Zr.

The EDS x-ray map of a dilute Al-0.01 Zr-0.07 Ti-0.062 at% B in Figure 24 shows a few Ti-rich precipitates at both grain boundaries and centers of grains, presumed to be  $TiB_2$  inoculant particles. It is common for relatively few particles to participate as grain nuclei during solidification, while many are pushed to grain boundaries. The same technique applied to the heavily grain refined Al-0.03 Zr-0.40 Ti-0.080 at% C (Figure 25) reveals many large Ti-rich particles at grain centers, in clusters in many cases. Further, panel D shows the segregation of Zr to these particles, indicating significant interaction of solute Zr with the inoculant particles. Although a poisoning effect was not directly observed as this alloy had a small grain size averaging  $35.7 \mu m$  and there a Zr-free alloy cast with this level of Al-Ti-C was not produced, there was near-zero aging response (Figure 32) as a result of a lack of Zr remaining in solution.

Near the bottom of the cast bars of Al-0.07 at% Zr (bottom of Figure 33), some columnar grains were observed at the mold walls which transitioned to a refined structure about 4 mm toward center. At the top of the mold, this casting is fully refined with the only evidence of columnar structure near the center in the last to solidify liquid (top of Figure 33). Where the microstructure is refined indicates a change in nucleation rate and/or mechanism. This could be due to primary  $Al_3Zr$  precipitation and subsequent grain nucleation during solidification, increase in impurity concentration due to segregation, or due to an increase in effective supercooling leading to increased nucleation in the liquid. The fastest local cooling rates in the bar sections were obtained at the top of the mold where the

room temperature mold remained relatively isolated from the large thermal mass of the gating section at the bottom of the mold. Near the bottom, the initial cooling rate was slower and some columnar grains formed initially. Grain size for this casting represented in Figure 32 was measured in the fully refined region.

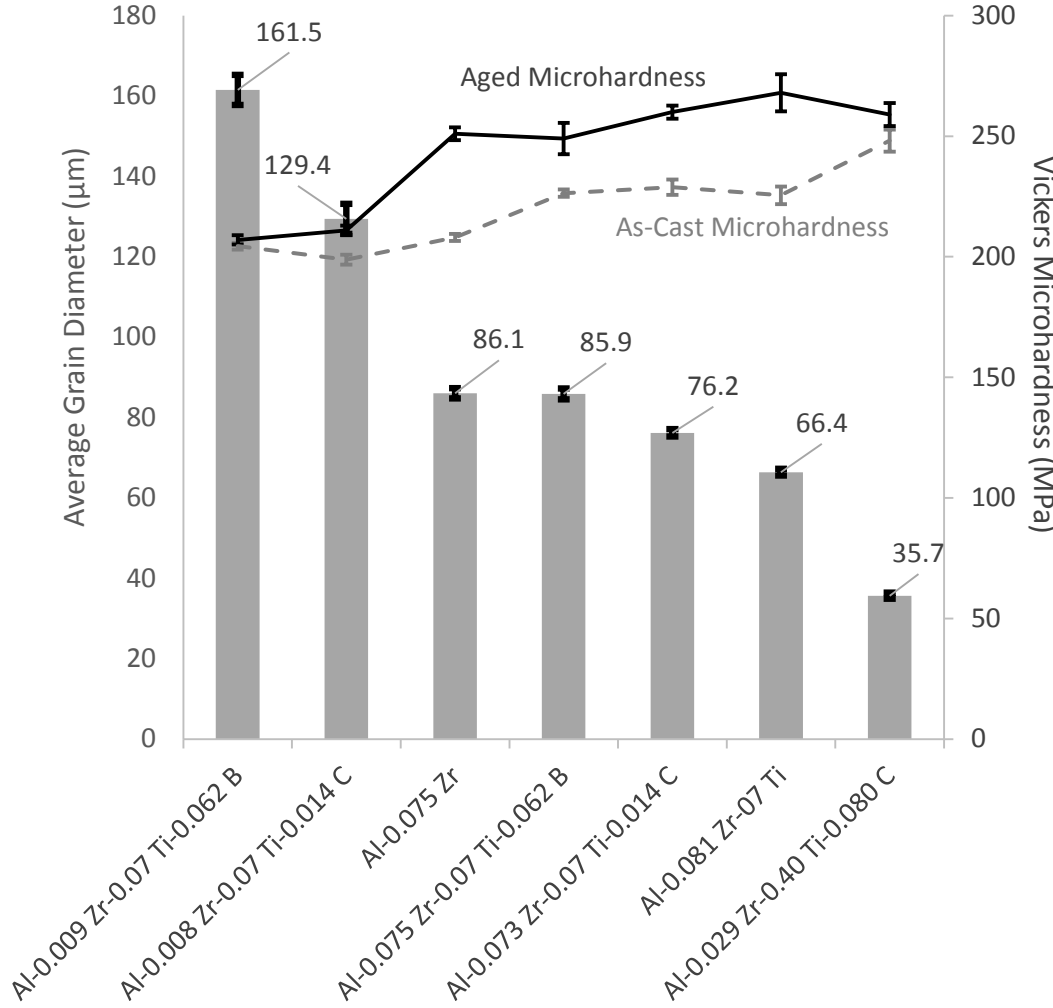


**Figure 32:** Average as-cast grain sizes and microhardness as a function of alloying content in at%. Aged microhardness is also shown as an indication of hardening potential.



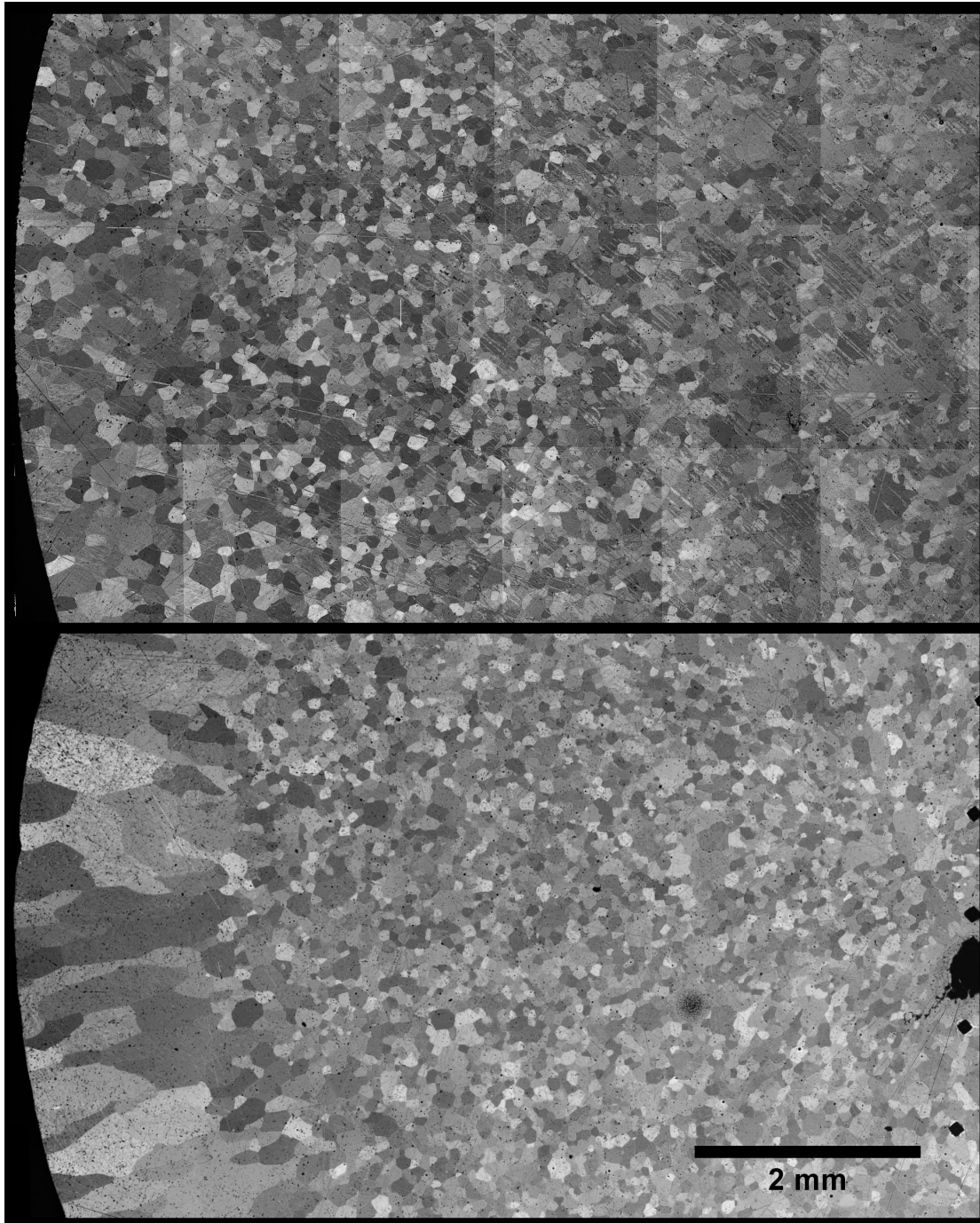


**Figure 33:** Optical micrographs from two locations on an Al-0.075 at% Zr bar cast in the VIM. Top - fully refined and equiaxed structure near the top of the bar, and Bottom - some columnar grains transitioning to equiaxed structure near bottom of casting with slower local cooling rate. A small amount of porosity can also be observed near center, as well as some Vickers microhardness indents.

## 4.2 Changes in Hardness and Conductivity during TMP

By tracking microhardness throughout processing, an overall idea of the internal changes taking place in the alloys can be gained. Increases in hardness indicate the formation of barriers to dislocation motion while decreased hardness signifies the removal of those barriers. These values are presented in Figure 34.

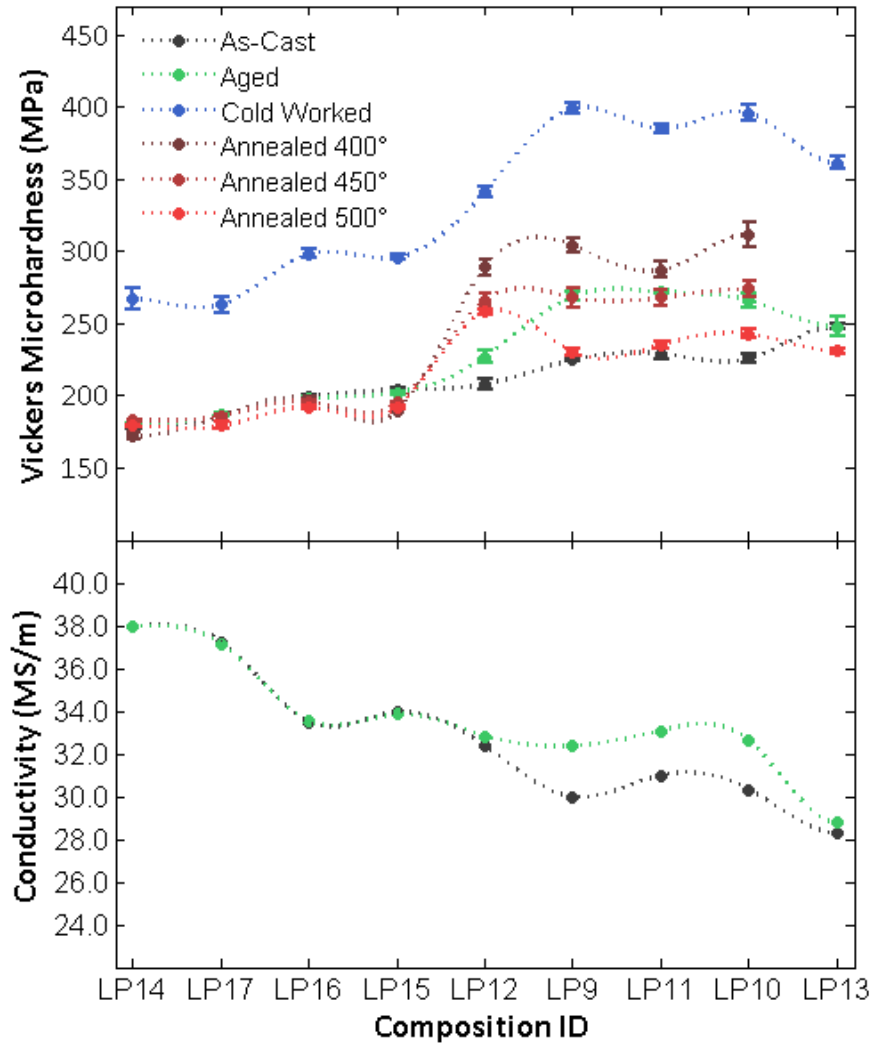


**Figure 34:** Hardness (top) and conductivity (bottom) measured whenever possible during processing. Standard error is given for hardness, while the standard error in conductivity measurements is less than 0.03 MS/m in all cases. Note: the retained hardness following annealing at 400, 450 and 500°C for the LP09, LP10, LP11, and LP12 castings; these are the same partially recrystallized structures shown through EBSD in Figures 23-27, the x-axis nomenclature refers to that used in Table 10, for brevity.

Hardness measured on as-cast samples increases with increasing alloying content, owing to more solute cast into solid solution; the exception here is binary Al-0.07 at% Zr which showed higher hardness than Al-0.07 Ti-0.01 at% Zr alloys. Upon artificial aging, the alloys with 0.07 at% Zr hardened significantly while all others neither increased nor decreased in hardness. 75% cold work added about 120 MPa to the 0.07 Zr alloys and 90-100 MPa to the lower Zr-content alloys, with the Al-0.07 Zr-0.07 at% Ti and Al-0.07 Zr-0.07 Ti-0.014 at% C alloys having the highest hardness at  $399 \pm 4.4$  and  $396 \pm 3.9$  MPa, respectively, after this step.

The low- and high-Zr alloys diverge further upon annealing at 400, 450, and 500°C. Alloys with 0.01 Zr or less revert to as-cast hardness in 24 hr at 400°C, while alloys with 0.07 Zr retain much of the cold work during these treatments, only falling to about 300 MPa after 24 hr at 400°C, and 270 MPa after 24 hr at 450°C. After 24 hr at 500°C, all alloys except binary Al-0.07 at% Zr reverted to as-cast hardness. The binary Al-0.07 at% Zr was more stable in terms of hardness even after twice as long as the other 0.07 at% Zr alloys at 500°C, only dropping to  $258 \pm 1.9$  MPa, 50 MPa more than as-cast, and 30 MPa more than in the aged-condition. This is due to the lack of interaction with Ti-rich particles and a consequently more effective distribution of  $\text{Al}_3\text{Zr}$  formed upon aging.

The 0.07 Zr-0.07 Ti, 0.07 Zr-0.07 Ti-0.062 B, and 0.07 Zr-0.07 Ti-0.014 at% C are tightly grouped throughout initial processing, starting with an as-cast hardness around 230, increasing to 265 following aging, and then close to 400 MPa following swaging. However, upon annealing at 400°C, the alloy with Al-Ti-B decreases in hardness more than the other two, indicating a comparative lack of stability. These alloys then re-converge when subjected to higher over-aging temperatures.

The Al-0.03 Zr-0.40 Ti-0.08 at% C alloy had the highest initial hardness but showed no age-hardening response. This correlates with the observations from EDS x-ray mapping, in which strong segregation of Zr to the Ti-rich particles was apparent, which would severely limit Zr in solution available for age hardening. However, the overall strength of this alloy is comparable to Al-0.07 at% Zr following cold work. Unfortunately, there is only one more

data point for this alloy, after 48 hr at 500°C, where it does show less stability compared to Al-0.07 at% Zr at this time and temperature.

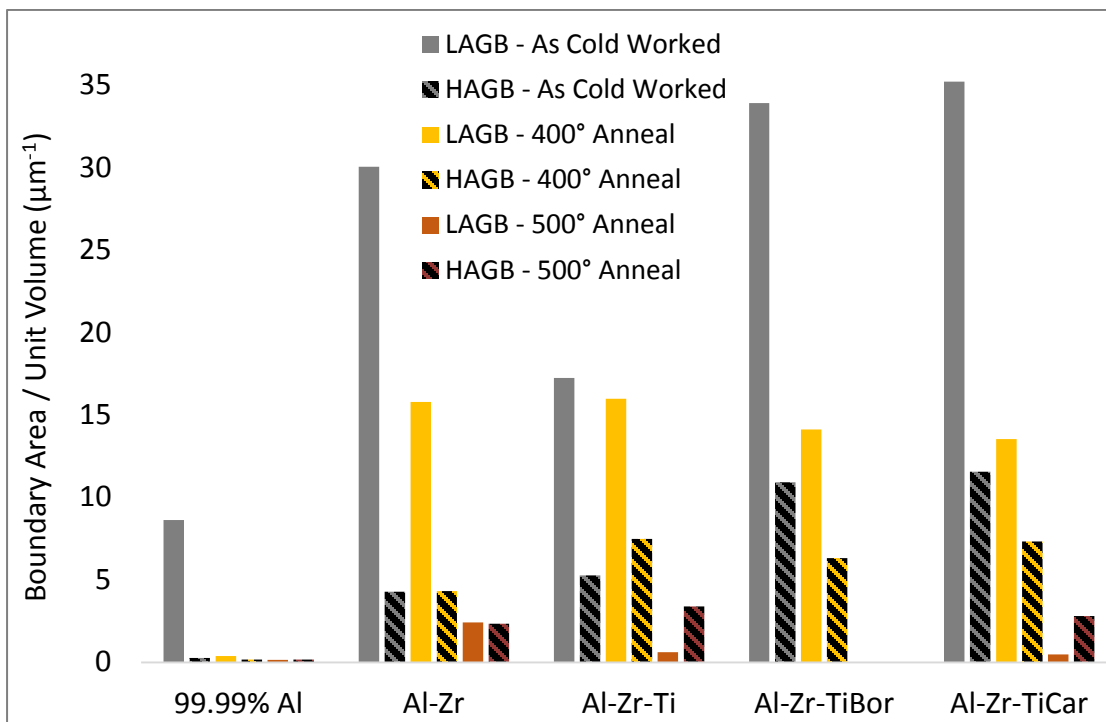
As solute is removed from solution during precipitation hardening, the mean free path for electrons increases which allows current to flow more readily through the metal. Because of this effect, electrical eddy current conductivity measurements often accompany hardness data to link the changes in hardness to concentration of solute left in solid solution. These measurements are highly sensitive to changes in atomic arrangements, yet easy to perform with handheld instrumentation. However, due to geometric constraints of the conductivity probe which require a minimum circular area 12.7 mm in diameter for measurement, only pre-cold worked samples were able to be measured for this study, i.e. as-cast and aged.

Pure aluminum has the highest conductivity at 37.99 MS/m, which does not change upon aging. AC and aged Al-0.01 at% Zr are near to this value as well, at 37.24 and 37.13 MS/m, respectively. Conductivity change between as-cast and aged samples is only observed for the 0.07 at% Zr alloys, which is consistent with the hardness data above. The binary Al-0.07 Zr alloy does not show as large of a change in conductivity, did not harden as much as expected during aging, and exhibited refined equiaxed grain structure, indicating primary precipitation of  $\text{Al}_3\text{Zr}$  during casting which depleted the matrix of solute Zr. It is noteworthy that the Al-Ti-B alloys have higher conductivity than Al-Ti-C alloys at the same Zr level. Boron is known to clean up impurities in metal alloys and semiconductors [123], yet in this case all of the added B and C are expected to be bound in pre-existing  $\text{TiB}_2$  and  $\text{TiC}$  since the solubilities in aluminum are negligible, and excess Ti for constitutional undercooling purposes is present. This indicates that boron is influencing conductivity while still bound to Ti by forming compounds with impurity atoms or Zr in solution; the latter is consistent with other observations in this study.

#### 4.3 Low- and High-Angle Grain Boundaries

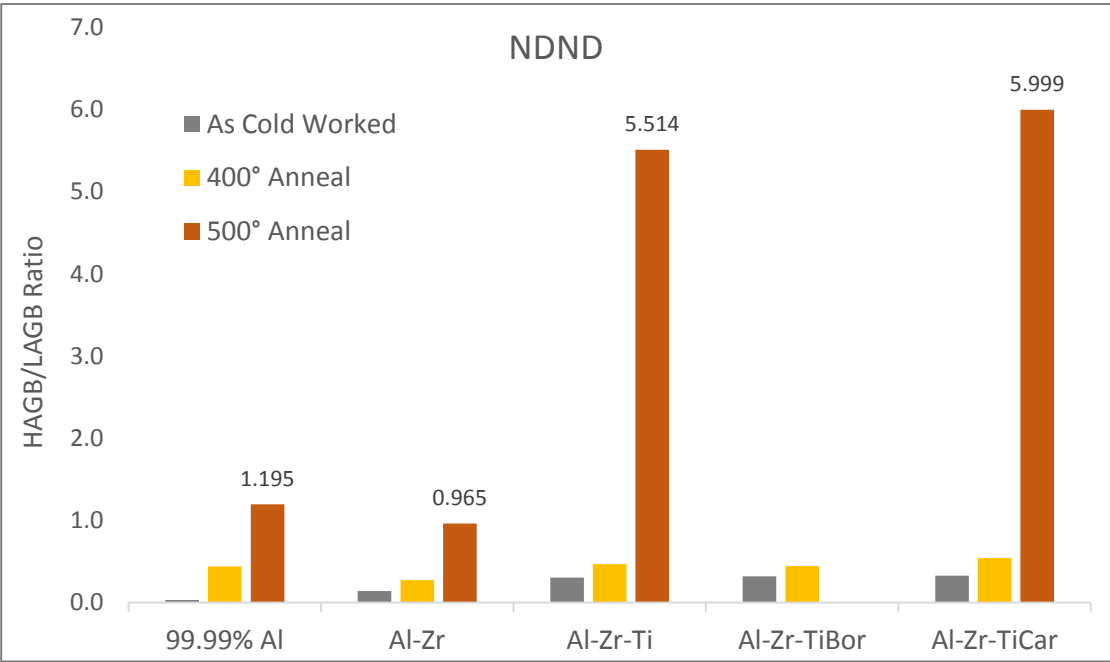
To quantify the effects observed in the EBSD scans for the alloys containing Al-0.07 at% Zr, the densities of low and high-angle boundaries were measured using a line intercept method on the EBSD scans of Figures 27-30. These values are presented in the bar chart in

Figure 35 in comparison to pure aluminum which was measured on a larger scan area so as to include at least one pre-existing high-angle boundary. In the cold-worked state, the density of HAGB increases in the alloys with grain refining additions relative to the compositions without those additions, possibly as a result of the more homogenous Orowan-type deformation mechanism being operative when relatively large particles are present as opposed to the shearing effects observed in Al-Zr and Al-Ti-Zr. All alloys retained a similar amount of LAGB area in the NDND orientation following annealing at 400°C indicating a significant amount of pinning from the 0.07 at% Zr addition. In contrast, only the Al-Zr binary alloy retained a significant density of LAGB area in the NDND orientation after the 500°C anneal and slightly lower density of HAGB area, and this sample was annealed twice as long (48 hr) compared to the other alloy compositions, as previously mentioned. This indicates that the large particles do, in fact, de-stabilize the microstructure at elevated temperatures.



**Figure 35:** Boundary area per unit volume for low- and high-angle boundaries in the as-cold worked and 400°C annealed samples. The Al-Zr-Ti-B NDND 500° sample is not included as an EBSD map was not collected for this sample.

The ratios of high/low-angle boundary density are presented in Figure 36 for the NDND orientation, and in Figure 37 for the NDSD orientation. A low value of this ratio typically indicates a significant amount of pinning pressure relative to growth pressure as LAGB area is retained and development of increased HAGB area is restricted, however, in the case of 99.99% Al, this value is low due to a very large grain size as well as scan size and therefore only relatively few boundaries are sampled over a larger area (See Figure 26, panels F and G). All other samples were imaged at a constant and higher magnification, and also contain many more boundaries of both types. In the NDND orientation (Figure 36), the HAGB/LAGB ratio is very similar for all alloys after annealing at 400°C, but this ratio is roughly 5x that of binary Al-Zr after annealing at 500°C for Al-Zr-Ti and Al-Zr-Ti-C. This clearly demonstrates the increased susceptibility to recrystallization of these alloys compared to binary Al-Zr.



**Figure 36:** High/low-angle grain boundary measured ratios on NDND samples in the as-cold-worked, 400°C, and 500°C annealed states. The Al-Zr-Ti-B NDND 500° sample is not included, as an EBSD map was not collected for this sample.

In the NDSO orientation, as was qualitatively observed in the EBSD images of Figures 30 and 31, there is retained subgrain structure in all samples and a clear difference between binary Al-Zr and the grain refined alloys is not apparent. The Al-Zr-Ti alloy was the least resistant to recrystallization indicating that the pinning pressure from small particles in this alloy were not nearly as effective as in the Al-Zr binary alloy. One explanation is that the precipitates in the ternary alloy are larger (i.e., over-aged) in comparison to the binary alloy, resulting in lower pinning pressure according to Equation 12. The total volume fraction is increased roughly twofold in the ternary alloy compared to the binary, and therefore the average particle radius must be increased more than twofold to rationalize this argument. Another possibility is solute segregation during solidification resulted in a highly inhomogeneous distribution in the ternary alloy, and less-so in the binary, which would lead to an overall reduction in recrystallization resistance. The fact that this decrease in recrystallization resistance is not observed in the grain refined alloys does not support this latter reasoning, since these alloys had a) larger initial grain size (i.e., more potential segregation of solute) and b) the same levels of Zr and Ti. To investigate further, a high resolution field emission SEM (FESEM), or possibly TEM, study is warranted to assess the distribution and sizes of precipitates in these alloys.

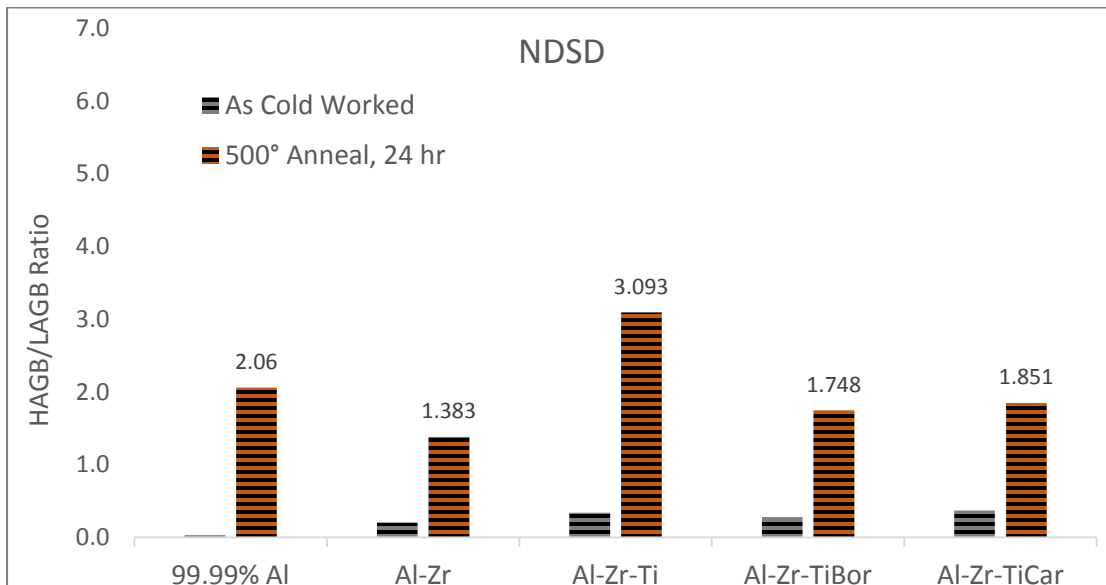


**Figure 37:** High/low-angle grain boundary ratio measured on NDSO samples in the as-cold-worked and 500°C annealed states.

#### 4.4 Theoretical vs. Observed Recrystallized Grain Size

A model was presented in Chapter II Section 1.2.4 which concluded with the relation of recrystallized grain size ( $D_R$ ) proportional to the fourth root of the difference between the driving pressure for migration of a boundary ( $P_D$ ) and the Zener pinning pressure ( $P_Z$ ) given by Equation 16. Assuming a constant nucleation frequency, boundary mobility, and number density of nucleant particles, as the difference between  $P_D$  and  $P_Z$  increases, the expected grain size increases as grains are able to nucleate and grow at a faster rate.  $P_Z$  is inversely proportional to the average pinning particle radius. The dependence of  $(P_D - P_Z)^{1/4}$ , and thus  $D_R$ , is plotted in Figure 38 as a function of this parameter. Regions are plotted for two volume fractions calculated using a lever rule approximation for the compositions used herein, and both are bounded by what could be expected for driving pressure nominally ( $P_D = 0.2$  MPa [121]) and in the near vicinity of larger, incoherent particles ( $P_D \approx 0.4$  MPa). A critical particle radius is observed below which the Zener pressure is high enough to completely restrict particle stimulated nucleation and growth, and recrystallization is expected to proceed by subgrain coarsening/rotation, resulting in very fine grain size stabilization and retention of deformation texture. This value is less than 1 nm for the 0.01 at% Zr alloy and around 12 nm for the 0.07 at% Zr alloy in regions of high misorientation, increasing to 23 nm nominally for the more Zr-rich alloy. Since all annealed NDSD microstructures exhibited a lack of equiaxed grain shape and some retained subgrain structure, it can be indirectly concluded that pinning particles are certainly less than ~25 nm in radius. Unfortunately, the annealed grain structures of the 0.01 at% Zr alloys were not characterized by any microscopy technique in the current study, and so the experimental comparison to this plot is not available, though this does represent an area of opportunity for immediate future work. Samples are electropolished and would simply need to be anodized and imaged under polarized light to assess recrystallized grain size and aspect ratio to determine if the samples are susceptible to PSN or not.



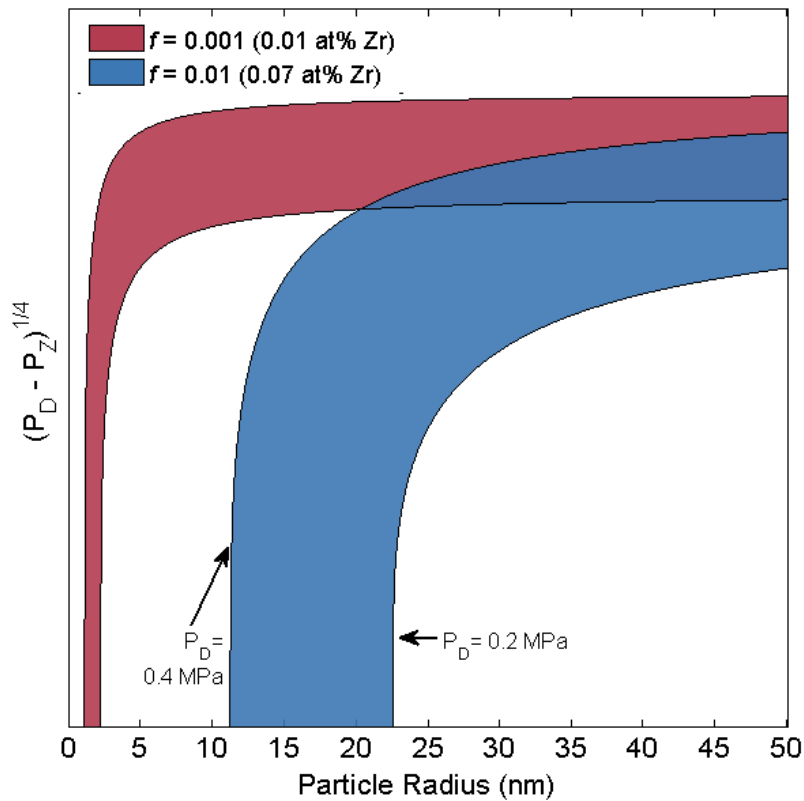


**Figure 38:** Anticipated dependence of recrystallized grain size on difference between driving pressure for boundary to migrate and Zener pinning pressure to restrict growth for the Zr levels studied here.  $P_D$  is nominally 0.2 MPa [121] after 75% cold work, but may increase in areas of high misorientation estimated at 0.4 MPa.

#### 4.5 Other Factors and Limitations

Rotary swaging is a violent, normal direction, compressive deformation process that can produce some heterogeneity in the deformed microstructure due to variations in local magnitude and direction of applied stress. Shear banding may occur in areas of high local stress as certain slip planes are weakened by shear of very small particles. This leads to zones of material in which the effective cold work is much higher than in other areas, and therefore the driving force for recrystallization ( $P_D$ ) is increased. In the absence of PSN, these regions are known to nucleate new strain free grains which can result in bands of small, recrystallized grains in between larger collections of subgrains where cold work has been

retained. Further study on the alloy systems studied here is warranted through a more uniform deformation technique, such as rolling to limit the occurrence of shear bands.

## Conclusions

- Grain size decreases with an addition of 0.07 at% Zr compared to 0.01 at% Zr in the presence of either grain refining additions Al-Ti-B or Al-Ti-C.
- Al-Ti-C is more effective, and interaction of Zr with the Al-Ti-B refiner is indicated by the larger grain size compared to Al-Ti-C at both Zr levels, the decreased hardening potential in both cases, and the increased conductivity in the presence of B.
- All alloys containing 0.07 at% Zr exhibit significant pinning pressure against recrystallized grains at 400°C, evidenced by EBSD scans of partially recrystallized structures and the corresponding quantification of low and high-angle grain boundary densities and HAGB/LAGB ratios.
- Alloys with grain refining additions are less resistant to static recrystallization than binary Al-0.07 at% Zr at 500°C, as indicated by low and high-angle grain boundary density measurements in the NDND plane. The recrystallized structures are all very similar in the NDSD plane, however, and the transition from elongated grains in Al-Zr to fully equiaxed grains in refined alloys was not observed. This indicates that pinning particles are sufficiently small to completely suppress PSN in Al-0.07 at% Zr, supported by model predictions presented in Section 4.4.



## List of References

- [1] V. Davydov, T. Rostova, V. Zakharov, Y.A. Filatov, V. Yelagin, *Materials Science and Engineering: A*, 280 (2000) 30-36.
- [2] L.S. Kramer, W.T. Tack, M.T. Fernandes, *Advanced Materials and Processes*, 152 (1997).
- [3] J. Royset, N. Ryum, *International Materials Reviews*, 50 (2005) 19-44.
- [4] L.S. Toropova, D.G. Eskin, M.L. Kharakterova, T.V. Dobatkina, *Advanced Aluminum Alloys Containing Scandium: Structure and Properties*, Taylor and Francis, Milton Park, Abingdon, Oxon, 1998.
- [5] K.E. Knipling, D.C. Dunand, D.N. Seidman, *Zeitschrift fur Metallkunde*, 97 (2006) 246.
- [6] N. Belov, A. Alabin, D. Eskin, V. Istomin-Kastrovskii, *Journal of materials science*, 41 (2006) 5890-5899.
- [7] M.A. Kerkove, T.D. Wood, P.G. Sanders, S.L. Kampe, D. Swenson, *Metallurgical and Materials Transactions A*, 45 (2014) 3800-3805.
- [8] T. Marumo, S. Fujikawa, K.-i. Hirano, *J. Jap. Inst. Light Met.*, 23 (1973) 17-25.
- [9] D.N. Seidman, E.A. Marquis, D.C. Dunand, *Acta Materialia*, 50 (2002) 4021-4035.
- [10] B. Smola, I. Stulikova, V. Očenášek, J. Pelcova, V. Neubert, *Materials Science and Engineering: A*, 462 (2007) 370-374.
- [11] C.B. Fuller, D.N. Seidman, D.C. Dunand, *Acta Materialia*, 51 (2003) 4803-4814.
- [12] E.A. Marquis, D.N. Seidman, D.C. Dunand, in: R.S. Mishra, J.C. Earthman, S.V. Raj (Eds.) *Creep Deformation: Fundamentals and Applications*, TMS (The Minerals, Metals, & Materials Society), 2002.
- [13] M.E. vanDalen, *Acta Materialia*, (2011).
- [14] K.E. Knipling, D.N. Seidman, D.C. Dunand, *Acta Materialia*, 59 (2011) 943-954.
- [15] E.A. Marquis, D.C. Dunand, *Scripta Materialia*, 47 (2002) 503-508.
- [16] E.A. Marquis, D.N. Seidman, D.C. Dunand, *Acta Materialia*, 51 (2003) 4751-4760.
- [17] R.A. Karnesky, D.N. Seidman, D.C. Dunand, *Materials Science Forum*, 519-521 (2006) 1035-1040.
- [18] K.E. Knipling, Northwestern University, 2006.
- [19] M.E. van Dalen, D.N. Seidman, D.C. Dunand, *Acta Materialia*, 56 (2008) 4369-4377.
- [20] M.E. vanDalen, *Acta Materialia*, 53 (2005) 4225-4235.
- [21] E. Clouet, L. Laé, T. Épicier, L. Williams, M. Nastar, A. Deschamps, *Nature Materials*, 5 (2006) 482-488.
- [22] Y. Riddle, T. Sanders Jr, *Metallurgical and Materials Transactions A*, 35 (2004) 341-350.
- [23] J. Murray, *Journal of phase equilibria*, 19 (1998) 380-384.
- [24] H. Okamoto, *Journal of phase equilibria*, 23 (2002) 455-456.
- [25] B. Forbord, W. Lefebvre, F. Danoix, H. Hallem, K. Marthinsen, *Scripta materialia*, 51 (2004) 333-337.

- [26] A. Tolley, V. Radmilovic, U. Dahmen, *Scripta materialia*, 52 (2005) 621-625.
- [27] W. Lefebvre, F. Danoix, H. Hallem, B. Forbord, A. Bostel, K. Marthinsen, *Journal of Alloys and Compounds*, 470 (2009) 107-110.
- [28] Y. Du, Y. Chang, B. Huang, W. Gong, Z. Jin, H. Xu, Z. Yuan, Y. Liu, Y. He, F.-Y. Xie, *Materials Science and Engineering: A*, 363 (2003) 140-151.
- [29] N. Peterson, S. Rothman, *Physical Review B*, 1 (1970) 3264.
- [30] Y. Minamino, T. Yamane, H. Araki, *Metallurgical and Materials Transactions A*, 18 (1987) 1536-1538.
- [31] S.-i. Fujikawa, K.-i. Hirano, Y. Fukushima, *Metallurgical Transactions A*, 9 (1978) 1811-1815.
- [32] A. Ardell, *Metallurgical Transactions A*, 16 (1985) 2131-2165.
- [33] Y. Harada, D. Dunand, *Materials Science and Engineering: A*, 329 (2002) 686-695.
- [34] E. Nes, *Acta Metallurgica*, 20 (1972) 499-506.
- [35] L.S.G. Darken, W. ROBERT, (1953).
- [36] E. Hornbogen, E. Starke, *Acta metallurgica et materialia*, 41 (1993) 1-16.
- [37] P. Hirsch, F. Humphreys, Cambridge, Massachusetts: MIT Press, 1969.
- [38] K. Bowman, *Mechanical Behavior of Materials*, John Wiley and Sons, Hoboken, 2004.
- [39] E. Nembach, (1997).
- [40] W.D. Callister, D.G. Rethwisch, *Fundamentals of materials science and engineering: an integrated approach*, John Wiley & Sons, 2005.
- [41] A. Rollett, F. Humphreys, G.S. Rohrer, M. Hatherly, *Recrystallization and related annealing phenomena*, Elsevier, 2004.
- [42] E. Nes, K. Marthinsen, *Materials Science and Engineering: A*, 322 (2002) 176-193.
- [43] K.E. Knipling, R.A. Karnesky, C.P. Lee, D.C. Dunand, D.N. Seidman, *Acta Materialia*, 58 (2010) 5184-5195.
- [44] V. Zakharov, *Metal science and heat treatment*, 45 (2003) 246-253.
- [45] Google Patents, 1971.
- [46] R. Kaibyshev, E. Avtokratova, A. Apollonov, R. Davies, *Scripta materialia*, 54 (2006) 2119-2124.
- [47] R. Mahmudi, P. Sepehrband, H. Ghasemi, *Materials Letters*, 60 (2006) 2606-2610.
- [48] H. Elhadari, H. Patel, D. Chen, W. Kasprzak, *Materials Science and Engineering: A*, 528 (2011) 8128-8138.
- [49] C. McNamara, S. Kampe, P. Sanders, D. Swenson, *Light Metals 2013*, (2013) 379-382.
- [50] M. Easton, D. Stjohn, *Metallurgical and Materials Transactions A*, 30 (1999) 1613-1623.
- [51] D. StJohn, A. Prasad, M. Easton, M. Qian, *Metallurgical and Materials Transactions A*, 46 (2015) 4868-4885.
- [52] H.J. Frost, M.F. Ashby, (1982).

- [53] R. Hyland, R. Stiffler, *Scripta metallurgica et materialia*, 25 (1991) 473-477.
- [54] E. Clouet, J.-M. Sanchez, C. Sigli, *Physical Review B*, 65 (2002) 094105.
- [55] C. Fu, *Journal of Materials Research*, 5 (1990) 971-979.
- [56] W.F. Gale, T.C. Totemeier, *Smithells metals reference book*, Butterworth-Heinemann, 2003.
- [57] Z. Jia, G. Hu, B. Forbord, J.K. Solberg, *Materials science and engineering: A*, 444 (2007) 284-290.
- [58] M.A. Kerkove, T.D. Wood, P.G. Sanders, S.L. Kampe, D. Swenson, *Metallurgical and Materials Transactions A*, (2013, submitted).
- [59] V. Radmilovic, A. Tolley, E.A. Marquis, M.D. Rossell, Z. Lee, U. Dahmen, *Scripta Materialia*, 58 (2008) 529-532.
- [60] V.K. LaMer, R.H. Dinegar, *Journal of the American Chemical Society*, 72 (1950) 4847-4854.
- [61] V.K.L. Mer, *Industrial & Engineering Chemistry*, 44 (1952) 1270-1277.
- [62] D.T. Robb, V. Privman, *Langmuir*, 24 (2008) 26-35.
- [63] B. Forbord, H. Hallem, N. Ryum, K. Marthinsen, *Materials Science and Engineering: A*, 387 (2004) 936-939.
- [64] D.A. Porter, K.E. Easterling, *Phase transformations in metals and alloys*, CRC Press LLC, 1992.
- [65] T.B. Massalski, H. Okamoto, P. Subramanian, L. Kacprzak, *ASM International*, 1990, (1990) 1485.
- [66] J. Murray, A. Peruzzi, J. Abriata, *Journal of phase equilibria*, 13 (1992) 277-291.
- [67] F. Crossley, L. Mondolfo, *J. Metals (New York)*, 3 (1951).
- [68] W. Dahl, W. Gruhl, G. Ibe, W. Burchard, C. Dumitrescu, *Zeitschrift fuer Metallkunde*, 68 (1977) 121-127.
- [69] B. Murty, S. Kori, M. Chakraborty, *International Materials Reviews*, (2002).
- [70] F. Wang, D. Qiu, Z.-L. Liu, J.A. Taylor, M.A. Easton, M.-X. Zhang, *Acta Materialia*, 61 (2013) 5636-5645.
- [71] T. Atamanenko, D. Eskin, L. Zhang, L. Katgerman, *Metallurgical and Materials Transactions A*, 41 (2010) 2056-2066.
- [72] K.E. Knipling, D.C. Dunand, D.N. Seidman, *Acta Materialia*, 56 (2008) 1182-1195.
- [73] E. Nes, *Journal of Materials Science*, 13 (1978) 2052-2055.
- [74] N. Ryum, *Acta Metallurgica*, 17 (1969) 269-278.
- [75] J.S. Vetrano, S.M. Bruemmer, L. Pawlowski, I. Robertson, *Materials Science and Engineering: A*, 238 (1997) 101-107.
- [76] B. Morere, R. Shahani, C. Maurice, J. Driver, *Metallurgical and Materials Transactions A*, 32 (2001) 625-632.
- [77] V. Ocenasek, M. Slamova, *Materials Characterization*, 47 (2001) 157-162.
- [78] K. Gardner, R. Grimes, *Metal Science*, 13 (1979) 216-222.
- [79] S. Srinivasan, P. Desch, R. Schwarz, *Scripta metallurgica et materialia*, 25 (1991) 2513-2516.
- [80] F. Van Loo, G. Rieck, *Acta Metallurgica*, 21 (1973) 61-71.

- [81] A. Bunn, P. Schumacher, M. Kearns, C. Boothroyd, A. Greer, *Materials science and technology*, 15 (1999) 1115-1123.
- [82] A. ABDEL-HAMID, *Zeitschrift fuer Metallkunde*, 80 (1989) 566-569.
- [83] M. Johnsson, *Zeitschrift für Metallkunde*, 85 (1994) 786-789.
- [84] G.P. Jones, J. Pearson, *Metallurgical Transactions B*, 7 (1976) 223-234.
- [85] A. Cibula, *J. Inst. Metals*, 80 (1951).
- [86] D. McCartney, *International Materials Reviews*, 34 (1989) 247-260.
- [87] M. Easton, D. StJohn, *Metallurgical and materials transactions A*, 36 (2005) 1911-1920.
- [88] P. Schumacher, A. Greer, J. Worth, P. Evans, M. Kearns, P. Fisher, A. Green, *Materials science and technology*, 14 (1998) 394-404.
- [89] G.V. Kumar, B. Murty, M. Chakraborty, *Journal of Alloys and Compounds*, 396 (2005) 143-150.
- [90] V. Dobatkin, Y.G. Grishkovets, *Metal Science and Heat Treatment*, 8 (1966) 628-631.
- [91] E. Nes, N. Ryum, *Scripta Metallurgica*, 5 (1971) 987-989.
- [92] R. Sandstrom, *Zeitschrift fur Metallkunde*, 71 (1980) 681-688.
- [93] J. Robson, *Materials Science and Engineering: A*, 338 (2002) 219-229.
- [94] A. Eivani, S. Valipour, H. Ahmed, J. Zhou, J. Duszczuk, *Metallurgical and Materials Transactions A*, 42 (2011) 1109-1116.
- [95] K.E. Knipling, D.C. Dunand, D.N. Seidman, *Acta Materialia*, 56 (2008) 114-127.
- [96] T. Nieh, L. Hsiung, J. Wadsworth, R. Kaibyshev, *Acta materialia*, 46 (1998) 2789-2800.
- [97] M. Jones, F. Humphreys, *Acta Materialia*, 51 (2003) 2149-2159.
- [98] R. Kaibyshev, F. Musin, D. Lesuer, T. Nieh, *Materials Science and Engineering: A*, 342 (2003) 169-177.
- [99] R. Kaibyshev, O. Sitdikov, A. Goloborodko, T. Sakai, *Materials Science and Engineering: A*, 344 (2003) 348-356.
- [100] K. Sotoudeh, P. Bate, *Acta Materialia*, 58 (2010) 1909-1920.
- [101] S. Katsas, R. Dashwood, R. Grimes, M. Jackson, G. Todd, H. Henein, *Materials Science and Engineering: A*, 444 (2007) 291-297.
- [102] F. Musin, R. Kaibyshev, Y. Motohashi, G. Itoh, *Scripta Materialia*, 50 (2004) 511-516.
- [103] F. Musin, R. Kaibyshev, Y. Motohashi, G. Itoh, *Metallurgical and materials transactions A*, 35 (2004) 2383-2392.
- [104] A. Haslam, S. Phillpot, D. Wolf, D. Moldovan, H. Gleiter, *Materials Science and Engineering: A*, 318 (2001) 293-312.
- [105] K. Harris, V. Singh, A. King, *Acta materialia*, 46 (1998) 2623-2633.
- [106] M. Ferry, N. Hamilton, F. Humphreys, *Acta materialia*, 53 (2005) 1097-1109.
- [107] M. Ferry, *Acta materialia*, 53 (2005) 773-783.
- [108] C. Booth-Morrison, D.C. Dunand, D.N. Seidman, *Acta Materialia*, 59 (2011) 7029-7042.

- [109] R. Grimes, C. Baker, M. Stowell, B. Watts, *Aluminium*, 51 (1975) 720-723.
- [110] B. Watts, M. Stowell, D. Owen, B. BAIKIE, *Metal Science*, 10 (1976) 189-206.
- [111] S. McFadden, R.S. Mishra, R. Valiev, A. Zhilyaev, A. Mukherjee, *Nature*, 398 (1999) 684-686.
- [112] F. Humphreys, *Acta Metallurgica*, 25 (1977) 1323-1344.
- [113] R. Ørsund, E. Nes, *Scripta metallurgica*, 22 (1988) 671-676.
- [114] R. Ørsund, E. Nes, *Scripta metallurgica*, 22 (1988) 665-669.
- [115] C.S. Smith, *Trans. Metall. Soc. AIME*, vol. 175, p. 15-51 (1948). 175 (1948) 15-51.
- [116] E. Nes, N. Ryum, O. Hunderi, *Acta Metallurgica*, 33 (1985) 11-22.
- [117] O. Hunderi, E. Nes, N. Ryum, *Acta Metallurgica*, 37 (1989) 129-133.
- [118] N. Ryum, O. Hunderi, E. Nes, *Scripta metallurgica*, 17 (1983) 1281-1283.
- [119] M. Ashby, J. Harper, J. Lewis, *Trans Met Soc AIME*, 245 (1969) 413-420.
- [120] N. Louat, *Acta metallurgica*, 30 (1982) 1291-1294.
- [121] J.A. Wert, L. Austin, *Metallurgical Transactions A*, 19 (1988) 617-625.
- [122] E. Nes, J.A. Wert, *Scripta metallurgica*, 18 (1984) 1433-1438.
- [123] S.C. J, *Google Patents*, 1962.





## Appendix I

### Metallographic Preparation

Samples are prepared by first grinding away the deformation zone left by the high speed diamond saw or other cutting operation on 120 grit silicon carbide paper; 0.5-1.5 mm is typically removed. The ground samples are deburred on 400 grit paper and then cleaned thoroughly. 14g Copper wire is wrapped around each sample and twisted tight for electrical contact. In the case of RD-SD sections, a hole is drilled near one side of the sample perpendicular to the RD-RD plane; the sample is then cut in half to expose the RD-SD section, and the copper wire passes through the drilled hole for electrical contact. Each sample is mounted in 24-hour epoxy (Aeromarine Products, San Diego CA) with the copper wire extending from the top and near the side of the mount (Figure A1) to facilitate autopolishing, electropolishing, anodizing, and electron microscopy of the aluminum surfaces. Once the epoxy sets, the mounts are broken out of their cups and each is carefully ground by hand on 240 grit silicon carbide followed by 400 grit silicon carbide.

A pair of LaboPol-1 autopolishers (Struers USA, Cleveland OH) are used for diamond polishing. Three samples are polished at a time on each machine starting with 7-9 minutes of 15  $\mu\text{m}$  on an MD-Largo pad with 20N of pressure applied via a spring mechanism. Samples are washed, rinsed, and ultrasonically bathed in ethanol before continuing on the a 9-10 minute 1  $\mu\text{m}$  diamond polishing step on MD-mol, again at 20N of applied pressure. The same cleaning procedure is followed preceding the final 1-2 minute 0.04  $\mu\text{m}$  colloidal silica suspension polish on an MD-chem pad at 10N.

Generally, the mounts continue on for anodizing following metallographic polishing. Anodization produces an  $\text{Al}_2\text{O}_3$  coating on the surface which has a thickness dependence on the underlying grain structure. A Polectrol (Struers USA, Cleveland OH) power supply and polishing cell are used in a fume hood for this process with a solution of 2.5% fluoboric acid at 15V applied potential in room temperature solution. Samples are suspended in the solution and electrical contact is made using the copper wire extending from the back of the mount. Anodization times are typically 60-75 seconds.

Electropolishing for EBSD and higher resolution optical microscopy is performed using the same Struers Pollectrol DC power supply and polishing cell. Modifications were made to allow the use of a methanol chiller to reach electropolishing temperatures between -20 and -40°C. Copper tubing, 7mm in diameter, was tightly coiled around a 1200 mL stainless steel beaker. The beaker was then inserted in the larger 1900mL stainless beaker and placed on the polishing cell. The outer beaker is then filled to the top of the coil with ethanol, and the outside of the assembly is wrapped in neoprene to help insulate the system. A stirrer bar and a stainless mesh anode are placed in the inner beaker which is then filled with electrolyte until the stainless mesh is covered. The electrolyte used here is a mixture of 91% ethanol, 7% perchloric acid, and 2% water, with careful attention paid to any ignition sources. Methanol from the chiller, which can reach -80°C, is pumped through the coil around the inner beaker which cools the system quickly. Temperature is monitored via NI-TC01 logger and current is manually recorded using a multimeter. Spare aluminum-epoxy mounts are used to collect voltage-current data in this solution to optimize the set-up. Setting voltage too high results in pitting, especially at grain boundaries, and too low causes instabilities which do not produce a smooth surface.



**Figure A1:** Mounted sample of aged, swaged, and annealed LP09 (Al-0.08 Zr-0.07 Ti) with wire incorporated into mount for anodizing and electropolishing.

## Appendix II

### Multi-step Aging Conductivity Curves

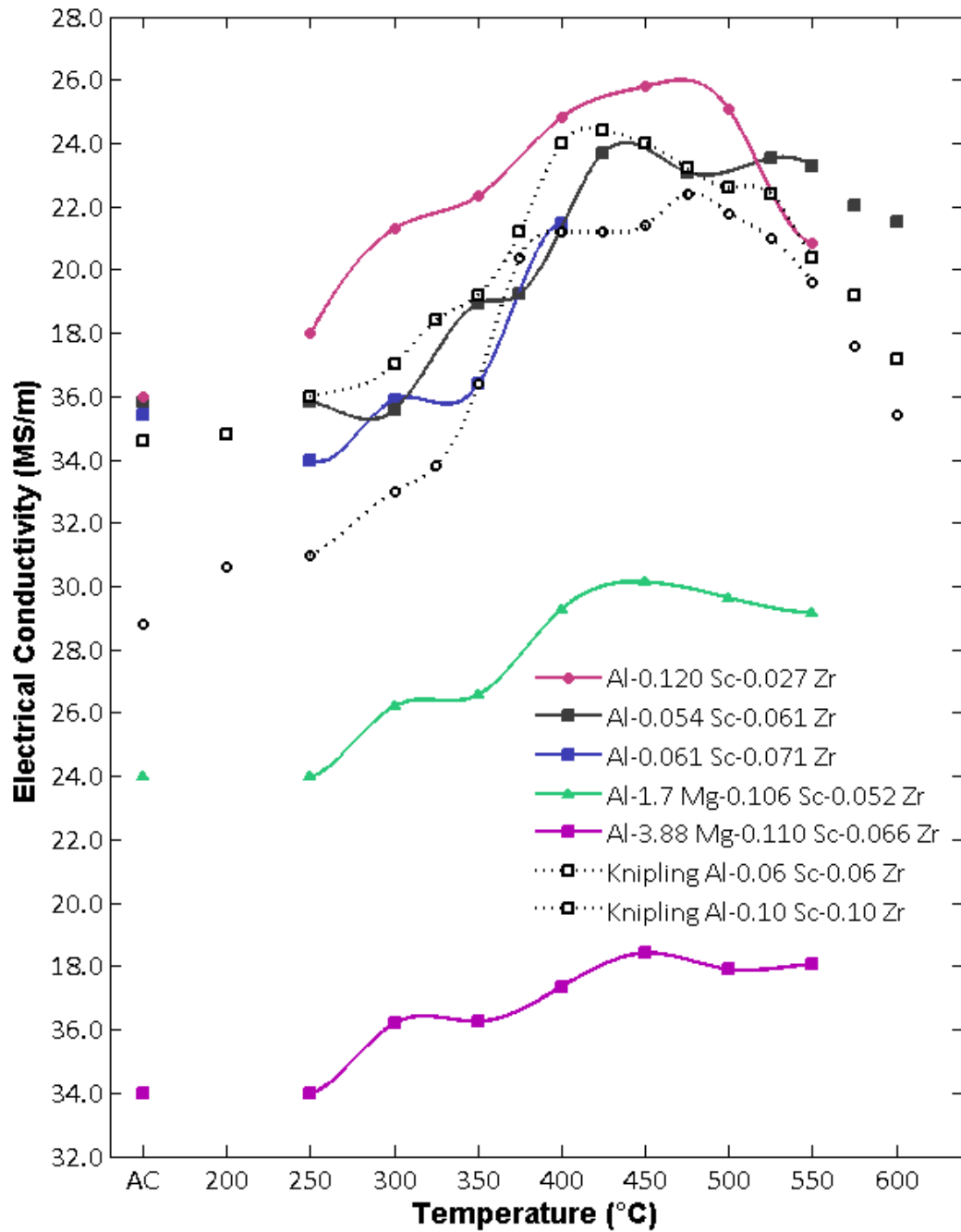


**Figure A2:** Conductivity changes during multi-step aging for various Al-Sc-Zr and Al-Mg-Sc-Zr with Al-0.06 Sc-0.06 Zr and Al-0.10 Sc-0.10 Zr reference data from [14, 43], respectively.



## Appendix III

### Casting X-ray Imaging



**Figure A3:** Digital x-ray image of casting LP09 (Al-0.08 Zr-0.07 Ti).

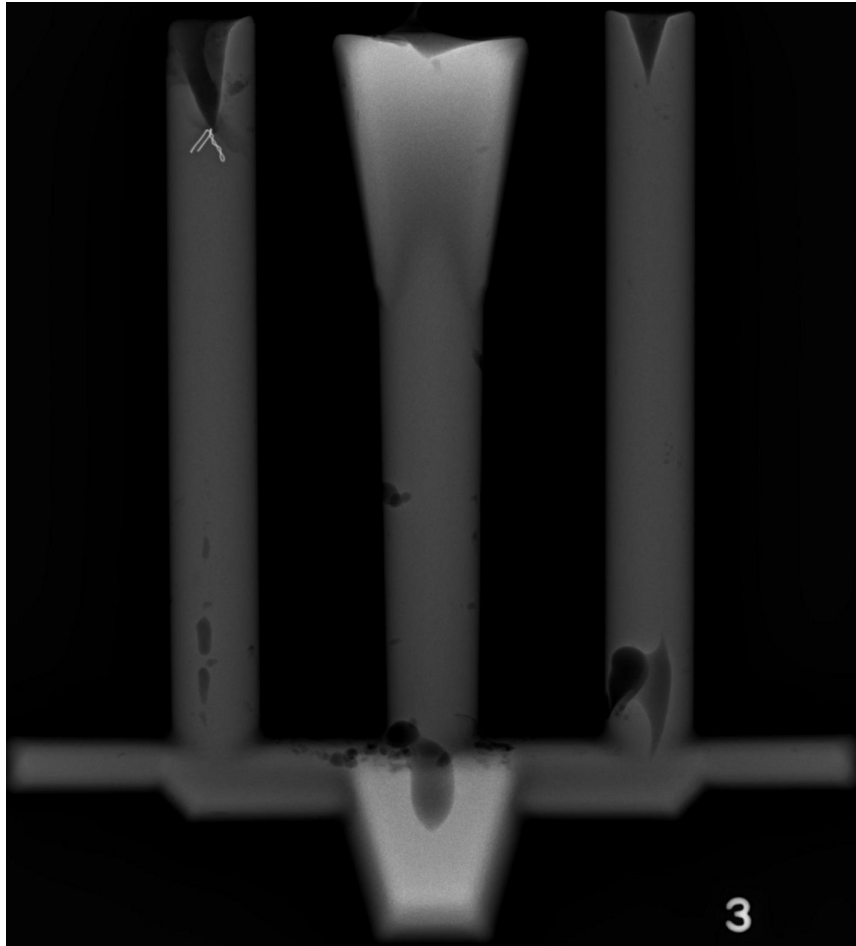


**Figure A4:** Digital x-ray image of casting LP10 (Al-0.07 Zr-0.07 Ti-0.014 C).

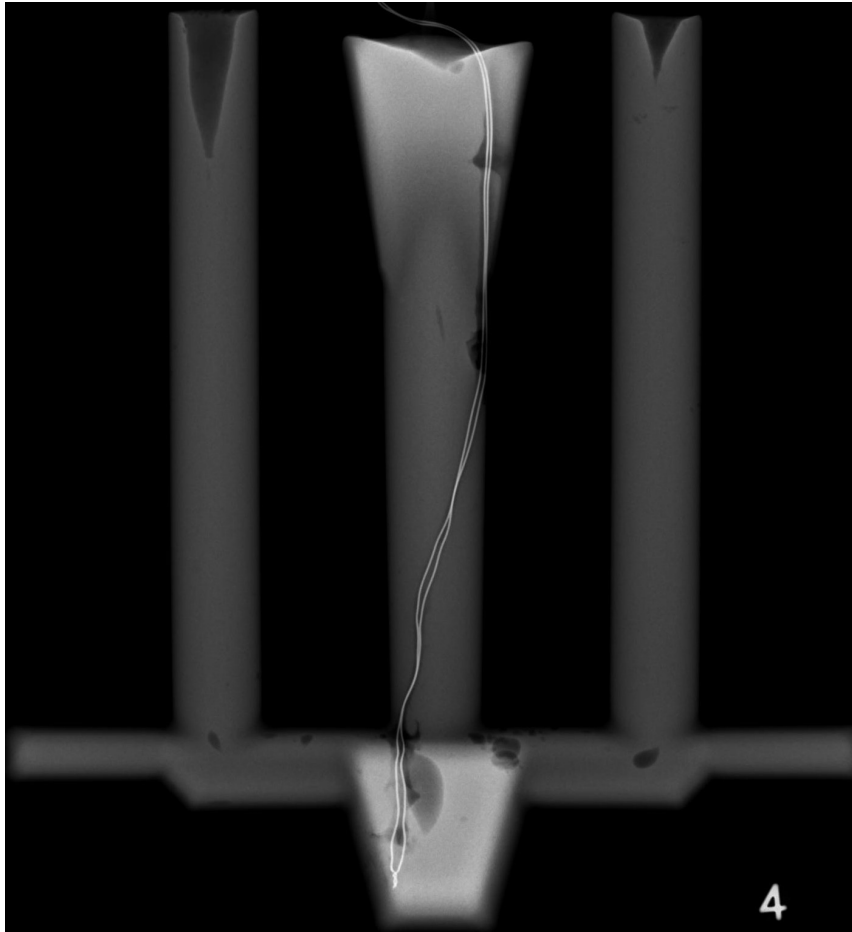



**Figure A5:** Digital x-ray image of casting LP10 (Al-0.07 Zr-0.07 Ti-0.014 C).





# Appendix IV

## All Available Raw Material Certification Sheets

**Belmont**  
METALS INC.   
THE NON FERROUS SPECIALISTS SINCE 1896

330 Belmont Avenue, Brooklyn, NY 11207-4000 U.S.A  
tel:+1.718.342.4900 fax:+1.718.342.0175

### Certificate of Analysis

May 03, 2010


To: Michigan Technological University  
Material Science & Engineering Dept.  
1400 Townsend Drive  
Room 512 M&M Bldg.  
Attn: Paul Saunders  
Houghton, MI 49931 USA

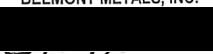
Customer Order No: Verbal  
Customer ID: MICHUN  
Belmont Order No: 3867


Material: 1009A BELMONT 99.99% ALUMINUM  
Shape: 24 LB Ingot  
Packaging: Skid

Lot: BR-82974

Aluminum (Al)	99.993
Copper (Cu)	0.00326
Iron (Fe)	0.00218
Silicon (Si)	0.00155
Zinc (Zn)	0.00014

  
1 T

BELMONT METALS, INC.  
  
Laboratory Director

  
BELMONT  
METALS



PACKING LIST /  
ANALYSIS REPORT  
72058 / 1

DELZIJL/NL  
KBM Master Alloys B.V.  
Kloosterlaan 2, 9936 TE FARMSUM  
P.O. Box 156, 9930 AD DELZIJL  
The Netherlands  
T + 31(0)596 641911  
F + 31(0)596 617321  
info@kbmasteralloys.com

OSS/NL  
KBM Master Alloys B.V.  
Waalkade 2, 5347 KS OSS  
P.O. Box 799, 5340 AT OSS  
The Netherlands  
T + 31(0)412 681311  
F + 31(0)412 635594

DUMMYKLANT USA

PACKING LIST / ANALYSIS REPORT

4 May 2012

Your Order No. :  
Our Order No. : 72058 / 1  
Product : 5% ZIRCONIUM BALANCE ALUMINIUM MASTER ALLOY IN THE FORM OF  
INGOTS COLOUR CODE - DARKBLUE B.T.N. 760120100

Qty Ordered : 7 KG  
Qty Delivered : 7 KG  
Gross Weight :  
Packing :  
Marks : PAUL SANDERS  
512 M&M BUILDING  
1400 TOWNSEND DR  
HOUGHTON, MI 49931  
906 487 2339

Pallet Number	Nett Weight In KG	Lot Heat Number	ZR	SI	FE
SAMP388	7	91594	5,1	0,03	0,17

WE CERTIFY THAT THE ANALYSIS ARE ACCURATE WITHIN  
COMMERCIAL LIMITS

O.C. DEPARTMENT



From: Paul Sanders <sanders@mtu.edu>  
Subject: **Fwd: Al-Sc Master Alloy Analysis AlSc2 sample: SC2017-2**  
Date: May 8, 2012 10:28:49 AM EDT



---

From: "Jennifer Smotek" <[JenniferS@ntruddock.com](mailto:JenniferS@ntruddock.com)>  
Date: April 9, 2010 1:10:57 PM EDT  
To: "Paul Sanders" <[sanders@mtu.edu](mailto:sanders@mtu.edu)>  
Subject: **FW: Analyse AlSc2 sample: SC2017-2**

Here is the certs they sent me. Hope it works for you. Your other material should be going out today. Thank you!

Jennifer

-----Oorspronkelijk bericht-----

Van: Jaco Belgraver  
Verzonden: vr 9-4-2010 15:54  
Aan: André Eykhoff  
Onderwerp: Analyse AlSc2 sample: SC2017-2

Sc: 1,6 wt%  
Si: 0,02 wt.%  
Fe: 0,08 wt.%  
Mg: 0,03 wt.%  
Ca: 0,01 wt.%  
Others each: < 0,01 wt.%



PACKING LIST / ANALYSIS REPORT

8079502 1

DELFIJL/NL	OSS/NL
KBM Master Alloys B.V.	KBM Master Alloys B.V.
Kloosterlaan 2, 9936 TE FARMSUM	Waalkade 2, 5347 KS OSS
P.O. Box 156, 9930 AD DELFIJL	P.O. Box 799, 5340 AT OSS
The Netherlands	The Netherlands
T + 31(0)596 641911	T + 31(0)412 681311
F + 31(0)596 617321	F + 31(0)412 635594
info@kbrmasteralloys.com	

DUMMYKLANT USA

PACKING LIST / ANALYSIS REPORT

14 October 2015

Your Order No. :  
 Our Order No. : 8079502/ 1  
 Product : 3% TITANIUM 0.15% CARBON BALANCE ALUMINIUM MASTER  
 ALLOY IN THE FORM OF CUT ROD, 50 CM PIECES  
 US HS CODE: 7604293010

Qty Ordered : 1 KG  
 Qty Delivered : 2 KG  
 Gross Weight : 22 KG  
 Packing : 1 Pallet  
 Marks : MICHIGAN TECHNOLOGICAL  
 UNIVERSITY, 512 MINERALS AND  
 MATERIALS BUILDING 1400  
 TOWNSEND DR HOUGHTON, MICHIGAN  
 USA 49931 ATT CAMERON MCANARA

Pallet Number	Nett Weight In KG	Lot Heat Number	TI	C	SI	FE
K55448S	2	K55448	3,0	0,19	0,03	0,10

WE CERTIFY THAT THE ANALYSIS ARE ACCURATE WITHIN COMMERCIAL LIMITS

O.C. DEPARTMENT

PO 100

FD035:03

Chamber of Commerce Groningen  
 reg. no. 02325066  
 VAT No. NL0081274R3R01



Sales by / Verkoop door (Met)